

Metal absorption systems in spectra of pairs of QSOs: how absorbers cluster around QSOs and other absorbers

David Tytler,¹★ Mark Gleed,¹ Carl Melis,¹ Angela Chapman,¹ David Kirkman,¹ Dan Lubin,¹ Pascal Paschos,¹ Tridivesh Jena¹ and Arlin P. S. Crotts²

¹Center for Astrophysics and Space Sciences, University of California San Diego, La Jolla, CA 92093-0424, USA

²Department of Astronomy, Columbia University, 550 West 120th Street, New York, NY 10027, USA

Accepted 2008 October 28. Received 2008 October 27; in original form 2007 December 13

ABSTRACT

We present the first large sample of metal absorption systems in pairs of QSOs with sightlines separated by about 1 Mpc at $z = 2$. We found 690 absorption systems in the spectra of 310 QSOs in 170 pairings. Most systems show C IV or Mg II absorption.

When we see absorption in one QSO, the probability that we see absorption in the paired QSO, within about 500 km s^{-1} , is at least ~ 50 per cent at $< 100 \text{ kpc}$, declining rapidly to ~ 8 per cent at $200\text{--}400 \text{ kpc}$, ~ 0.8 per cent by $1\text{--}2 \text{ Mpc}$ proper distance. Although we may occasionally see an individual absorbing halo in two sightlines, the absorber-absorber correlation is primarily a probe of the distribution of metals around galaxies and Mpc scale galaxy clustering. QSO absorption lines give redshifts errors of $\sim 23 \text{ km s}^{-1}$, almost 10 times smaller than the error for galaxy spectra at these redshifts, hence we can measure clustering on small scales, around 0.5 Mpc proper, with a small sample. The distribution of 23 absorber-absorber coincidences separated by $< 2.5 \text{ Mpc}$ at $z \sim 2$ is consistent with an origin in galaxies with a normal correlation function, normal systematic infalling velocities and low random pair-wise velocity differences, more consistent with blue than with red galaxies. Absorption in gas flowing out from galaxies with a mean velocity of 250 km s^{-1} would produce more redshift elongation than we see. The fast winds detected by Adelberger et al. in the same ions account for less than 1/3 of the absorption systems we see. Such winds may be confined to the ultraviolet (UV) luminous star-forming regions of Lyman break galaxies. If most galaxies have winds, they cannot extend to 40 kpc with large velocities, while continuing to make UV absorption that we can detect. This suggests that most metals seen in the intergalactic medium at $z = 2$ arrived long before.

We see an excess of C IV absorbers, with an a posteriori probability of 0.0003, when a line of sight passes a foreground QSO. We see 16 absorbers where we expect 5.8 at $0\text{--}600 \text{ km s}^{-1}$, on the front side of the partner QSO. At these velocities, we see an excess absorber in ~ 6 per cent of sightlines that pass within $0.1\text{--}2.5 \text{ Mpc}$ of a QSO, but in < 2 per cent of cases when we look directly at a QSO. These transverse associated absorbers are not the normal line-of-sight associated absorbers that have a broader velocity distribution. Excluding the sightlines to us, the 3D distribution of 59 absorbers around 313 QSOs is approximately isotropic, except for the $1.5\text{--}2\sigma$ tendency for the excess C IV absorbers to be on the front side of the QSOs. Our QSO redshifts may be too large by $\sim 300 \text{ km s}^{-1}$, or there might be a real asymmetry coming from a hypothetical anisotropy in the QSO UV emission, or from isotropic UV emission that lasted less than $\sim 1 \text{ Myr}$, possibilities suggested by the excess H I behind these QSOs. The velocity dispersion of the excess absorbers near the QSOs is small, $\sim 250 \text{ km s}^{-1}$, suggesting that both these absorbers and the QSOs are in the blue sequence of galaxies. The probability of seeing absorption when a sightline passes a QSO rises only slowly as the

★E-mail: davidtytler@gmail.com

impact parameter drops from 2.5 to 0.1 Mpc, perhaps because the UV radiation from QSOs destroys many nearby absorbers.

Key words: intergalactic medium – quasars: absorption lines – quasars: general – cosmology: observations.

1 INTRODUCTION

In this paper we discuss correlations between metal-line absorption systems seen in the spectra of pairs of QSOs. The sightlines to these pairs have an average separation of 1 Mpc proper at $z = 2$. These metal systems probe two separate environments; metals in the outer regions of galaxies that are far from both QSOs, and separately, metals in the immediate vicinity of one or both QSOs.

The absorption lines that we see typically come from the outer parts of galaxies. We use moderate resolution spectra [full width at half-maximum (FWHM) 83–280 km s $^{-1}$], with a wide range of S/N and hence we are sensitive to a wide range of absorption-line equivalent widths, but we only rarely detect the weaker metal lines from the intergalactic medium (IGM) far from galaxies.

In the remainder of this introduction we discuss metal absorption systems far from the QSO and then those near to the QSO, and finally we describe the distance measures that we use.

1.1 Metals absorption far from QSOs

In general, the correlation of metal-line absorption between sightlines tells us about the distribution, size and structure of the regions that produce metal absorption.

When QSO sightlines are separated by <100 kpc we can see similar metal absorption lines in each, indicating that the light is passing through the same gas ‘clouds’ (Rauch et al. 2001, 2002). We expect the density, ionization and metal abundances to be changing over the distance between the sightlines, but we often lack information to determine how they change. Weymann, Carswell & Smith (1981) note that it is hard to distinguish between absorption by a single large cloud and absorption by clustered clouds that are too small to individually cover both sightlines.

The sizes of the metal absorbing regions, either single clouds or clusters of clouds, have been estimated from various pairings on the sky. Lensed images of the same QSO (Steidel & Sargent 1991) probe the smallest separations and give proper sizes of ~ 15 to about ~ 80 kpc (we use $H_0 = 71$ km s $^{-1}$ Mpc $^{-1}$). Pairs of physically distinct QSOs close to each other on the sky, like those used here, typically probe separations greater than 1 Mpc, but the occasional pair is closer and gives sizes of roughly 100 kpc for strong C IV absorbers (Crotts et al. 1994). Chen, Lanzetta & Webb (2001) find C IV is very often seen out to impact parameters (radii) of 140 kpc around galaxies seen in images, but only rarely beyond that distance. Churchill et al. (2007) discuss one E/SO galaxy that shows no metals at 58 kpc, showing that not all galaxies absorb at large distances. Adelberger et al. (2005a) examined the absorption near 1044 foreground galaxies in the spectra of 23 background QSOs and found C IV absorption with column densities $N(\text{C IV}) \gg 10^{14} \text{ cm}^{-2}$ is often seen to radii of 40 kpc, while $N(\text{C IV}) \approx 10^{14} \text{ cm}^{-2}$ is seen to 80 kpc. A corresponding size for Mg II absorbers, at lower redshifts $z \lesssim 0.5$, is about 70 kpc (Lanzetta & Bowen 1990). We will see strong correlations arising from sightlines that pass through the

same halo, but in general our paired sightlines are too far apart to both probe the same halo.

On larger scales the correlation in the redshifts of metal-line absorption in adjacent sightlines depends on the clustering of dark matter and baryons, modified by the spatial variation in both the ratio of metals to baryons, and the level of ionization.

We know from many large surveys of single QSO sightlines that metal lines are very strongly clustered on scales of <150 km s $^{-1}$, with detectable clustering out to beyond 600 km s $^{-1}$ (Sargent, Boksenberg & Steidel 1988; Petitjean & Bergeron 1994; Rauch et al. 1996; Pichon et al. 2003; Scannapieco et al. 2006), and possibly out to 140 Mpc or $\sim 50\,000$ km s $^{-1}$ for $q_0 = 0.5$ (Quashnock, vanden Berk & York 1996). Absorption systems with higher H I or metal-line column densities tend to be more strongly clustered and confined, while those with low column densities are more widespread (Sargent et al. 1980; Tytler 1987; Cristiani et al. 1997).

With some assumptions, we can convert velocities along sightlines into a prediction for the correlation between adjacent sightlines. We need to specify the cosmological model and the 3D density field of the metal ions. Ignoring peculiar velocities, we would expect to see metal lines weakly correlated in sightlines separated by $<600/H(z) \simeq 3$ Mpc at $z = 2$. Crotts, Burles & Tytler (1997) found that the clustering in the plane of the sky was weaker than along the line of sight (LOS) for C IV seen in HIRES spectra of the three QSOs near 1623+27. They suggest this might be because peculiar velocities make the clustering appear overextended along the LOS.

Scannapieco (2005) argues that we expect metals to be highly clustered around their sources, the high-density peaks. Scannapieco et al. (2006) show that the metal-line correlation function along an LOS can be modelled with most metals confined to bubbles of radius 2 Mpc comoving. On the other hand, Pieri, Schaye & Aguirre (2006) show that the incidence of weak C IV and O VI absorption is similar both near to galaxies (marked by strong metal lines) and far from galaxies, indicating that some metals (mostly below our detection threshold) are present well beyond the immediate surroundings of galaxies.

Coppolani et al. (2006) did not see any significant correlation in 139 C IV systems towards 32 pairs of QSOs, except for an overdensity of C IV in front of a group of four QSOs. Since the mean separation of their QSO pairs is greater than 2 arcmin, they conclude that the metal enriched ‘bubbles’ should not cover both sightlines. Below we will show that we see strong correlations between sightlines only for the smallest angular separations. Simcoe et al. (2006) study galaxies and intergalactic gas towards a single QSO at $z = 2.73$ and conclude that the metal absorption can arise from bubbles of radii ≈ 100 kpc and thickness ≈ 1 kpc.

On the largest scales, Jakobsen et al. (1986) and Sargent & Steidel (1987) discuss evidence for a supercluster filament causing absorption at similar velocities in sightlines separated by 17.9 arcmin. Romani, Filippenko & Steidel (1991) describe how absorption in pairs of QSOs could be used to find superclusters at high redshifts, before any galaxies were known at these redshifts. Jakobsen & Perryman (1992) used C IV absorption in 12 QSOs including Tol

1037-2703 to detect a sheet spanning tens of Mpc. Tytler, Sandoval & Fan (1993) saw no sign of periodicity on 10–210 Mpc scales in the 3D distribution of 268 Mg II absorption systems. Loh, Quashnock & Stein (2001) examined the 3D distribution of 345 C IV systems from 276 QSOs and found evidence for clustering on scales up to 220 Mpc ($q_0 = 0.5$). Vanden Berk et al. (2000) found four metal-line absorption systems towards QSOs near to the HDF, two of which have redshifts that place them in the second most populated peak in the galaxy redshift distribution. Williger et al. (1996) compiled a statistically complete sample of C IV absorption at $1.5 < z < 2.8$ in 25 sightlines. They found evidence for structure on 2–50 Mpc proper scales for C IV absorbers, but not for a smaller sample of 11 Mg II absorbers.

Overall, this body of work shows that the distribution of absorption systems reveals large-scale structure, including the redshift spikes seen in narrow angle galaxy surveys (Broadhurst et al. 1990). The sample of absorbers that we present in this paper will include clustering on all scales, but it is best suited to studying correlations on small scales, because we have a very low sampling density. We rarely see even one metal system when we pass a given group of galaxies.

1.2 Metals absorption near to QSOs

Absorption by metals near to QSOs will help us understand the feedback of QSOs on the IGM. We may see the ejection of hot gas containing metals from the QSOs. We may see absorption from the emission-line region, the ISM of the QSO host galaxy, and the galaxies clustered around the QSO host. The number of absorbers, their velocities and their angular distribution about the QSOs will tell us about the density and velocity fields near the QSO host. We might learn about the mass of the QSO hosts, since we expect larger peculiar velocities around more massive hosts.

We expect to see enhanced photoionization by the QSO ultraviolet (UV) flux, but this will be reduced because the gas density will also be higher near the QSOs (Rollinde et al. 2005). Guimarães et al. (2007) find that the H I proximity effect in 45 QSOs at $z > 4$ is less than expected, by an amount that implies that QSOs reside in regions with overdensities of 5 to 2 within 4–15 Mpc, with higher luminosity QSOs in higher overdensities. D’Odorico et al. (2008) also find a density enhancement to 4 Mpc, but not out to 14 Mpc.

If the QSO UV flux is not isotropic, then we might see an anisotropic spatial distribution of the absorbers about the QSOs. If the QSOs have had the UV luminosity that we observe for only a few Myr, then we may see different amounts of absorption in front of, versus behind, the QSOs.

We will distinguish between absorption seen along a single LOS (from a QSO to the Earth) from that seen in the spectrum of a second background QSO, and transverse to the LOS. It also helps to distinguish different ions, since they probe different gas densities and respond differently to the QSO environment.

It is now well established that a significant fraction of metal lines systems are intrinsic to QSOs and not at the positions implied by their redshifts. Richards et al. (1999) found that the numbers of C IV systems in a heterogeneous catalogue of absorption systems depended on the optical luminosity and radio properties of the QSOs. If this were confirmed in a homogeneous sample it would be evidence that up to 36 per cent of C IV systems are intrinsic (Ganguly & Brotherton 2008). Misawa et al. (2007) used doublet ratios of metal lines in Keck HIRES spectra of 37 QSOs to conduct the first large survey of the frequency of absorbers that do not cover the

QSO UV radiation source. They found 28 reliable cases of intrinsic absorption, corresponding to 10–17 per cent of narrow C IV systems at velocities of 5000–70 000 km s⁻¹ from their QSOs, and at least 50 per cent of QSOs show intrinsic systems. Wild et al. (2008) examine Sloan Digital Sky Survey (SDSS) QSO spectra to find that >40 per cent of C IV systems within 3000 km s⁻¹ of a QSO are not the result of large-scale clustering and are directly associated with that QSO, in a population that extends to 12 000 km s⁻¹. Nestor, Hamann & Rodriguez Hidalgo (2008) survey narrow C IV absorption lines in SDSS QSO spectra and find >43 per cent of absorbers within a velocity range of 750–12 000 km s⁻¹ in the QSO frame are intrinsic to the QSOs. In a review, Ganguly & Brotherton (2008) estimate that 60 per cent of QSOs, with a wide range of luminosity, display outflows in absorption that we detect in various ways including broad absorption line (BAL) features, and absorption with partial coverage, time variability, high photoionization or high metallicity.

When we see common absorption in pairs of QSO spectra, we can conclude that this absorption is intervening and not ejected gas. The outflows mentioned above are generally believed to be confined to within a few pc to a few kpc of the QSOs (Narayanan et al. 2004; Wise et al. 2004; Misawa et al. 2005), too small a distance to intercept the other LOS.

1.2.1 Absorption near to QSOs and along individual lines of sight

We see various behaviours in the number of absorption lines from different ions at velocities near to the QSOs emission redshifts. The amount of H I decreases, probably because of the increased photoionization. The number of Lyman limit systems (LLS) is little changed, while the number of C IV lines (Young, Sargent & Boksenberg 1982) and damped Ly α (DLA) lines (Russell, Ellison & Benn 2006) increases. While it has long been known that N V lines are often found near to QSOs (Petitjean, Rauch & Carswell 1994), a fascinating analysis of UVES spectra of 19 QSOs by Fechner & Richter (2008) shows about twice as many systems with N V far from QSOs compared to near. Prochaska, Hennawi & Herbert-Fort (2008) study the incidence of DLAs within 3000 km s⁻¹ of QSOs. At $z < 2.5$ and $z > 3.5$ they see no deviation from a flat intervening distribution, but at intermediate z they see twice the usual number of DLAs. They had expected 5–10 times more DLAs near the QSOs because of clustering of galaxies around the QSOs and speculate that this lack is due to the enhanced ionization from the QSOs.

It has long been known (Tytler 1982) that there is no strong excess of LLS with $z_{\text{abs}} \simeq z_{\text{em}}$ along individual sightlines to mostly high-luminosity QSOs, and hence no sign of H I absorption in the host galaxies. There are two obvious explanations. First, the QSOs might be in galaxies (elliptical or lenticular) that have insufficient H I columns to make LLS, where LLS need $\log N_{\text{H}_1} > 17.2 \text{ cm}^{-2}$. While high-luminosity QSOs are in elliptical galaxies, low-luminosity QSOs are often disc galaxies (Hamilton, Casertano & Turnshek 2002), hence we predict that lower luminosity QSOs may show enhanced LLS at $z_{\text{abs}} \simeq z_{\text{em}}$. Secondly, the QSO UV radiation or relativistic jets may have ionized the gas in the sightline. In some models, feedback from optical (Di Matteo, Springel & Hernquist 2005) or radio-loud active galactic nuclei (AGN) (Best 2007) can effect the host galaxy as a whole, tending to make it appear like an elliptical galaxy, and hence making the first explanation a consequence of the second: the host is elliptical because the QSO changed the host.

1.2.2 Absorption near to QSOs and seen in background spectra: transverse

The results of searches for a relative decrease in H_I absorption near foreground QSOs, the classical ‘transverse proximity effect’, are mixed. In early work, Dobrzycki & Bechtold (1991a,b) found a large transverse void in the amount of Ly α absorption that they concluded was probably not caused by UV from a foreground QSO. Srianand (1997) discussed a second void that was less than expected from the foreground QSO luminosity. Fernandez-Soto et al. (1995) and Liske & Williger (2001) claimed marginal detections of the transverse proximity effect. Crotts (1989) and Moller & Kjaergaard (1992) saw no lack of H_I absorption. Other work (Crotts & Fang 1998; Croft 2004; Schirber, Miralda-Escudé & McDonald 2004) has shown enhanced, instead of decreased, H_I absorption near foreground QSOs.

Three types of explanation have been discussed for the absence of the H_I transverse proximity effect.

(i) The QSOs were less luminous in the past, by factors of 10–100 some 1–30 Myr ago (Schirber et al. 2004). The QSOs may resemble fireflies with short luminous episodes punctuating longer dark periods.

(ii) The QSO radiation is beamed or obscured so that their typical luminosity in transverse directions is factors of 10–100 lower than in the LOS direction (Barthel 1989; Crotts 1989; Moller & Kjaergaard 1992; Antonucci 1993; Schirber et al. 2004). Narrow beam opening angles are disfavoured by other evidence Urry & Padovani (1995).

(iii) The H_I does see the full QSO UV luminosity that we see, but the increased photoionization is partly cancelled by increased gas density, and the increased number of galaxies near the QSO (Loeb & Eisenstein 1995; Schirber et al. 2004; Rollinde et al. 2005; Guimarães et al. 2007; Kim & Croft 2007; Faucher-Giguere et al. 2008).

The first two explanations both make the radiation around the QSOs appear anisotropic from our perspective. The third explanation is widely agreed to be a real effect that enhances the numbers of many types of absorbers near to QSOs.

In contrast to H_I, there are claims that the He II ionization is changed by the radiation from foreground QSOs (Jakobsen et al. 2003; Worseck & Wisotzki 2006; Worseck et al. 2007; Worseck & Wisotzki 2007). Worseck & Wisotzki (2006) claim that the hardness of the radiation ionizing H_I and He II changes near to four foreground QSOs and their lifetimes are at least 10–30 Myr ago.

Only a few cases of metal-line systems near to foreground QSOs have been found (Shaver, Boksenberg & Robertson 1982; Shaver & Robertson 1983, 1985; D’Odorico, Petitjean & Cristiani 2002; Adelberger et al. 2006) because few QSO pairs were known until recently. Williger et al. (1996) found marginal evidence of an association between C IV absorbers and a grouping of 25 QSOs.

Bowen et al. (2006) found excess Mg II absorption in background QSOs at the emission redshift of foreground QSOs. They considered four pairs of QSOs with separations of 3–15 arcsec, or 26–97 kpc. Since we do not expect to see associated Mg II in four out of four sightlines, they conclude that the absorbing gas is not isotropic, and they discuss possible explanations. While no single explanation fits all four cases, the some of the absorbers can arise in the QSO host galaxies and others in near by galaxies.

Hennawi & Prochaska (2007) examine the incidence of a subset of all LLS, those with $\log N_{\text{H}_I} > 19 \text{ cm}^{-2}$, in the spectra of 149 QSO pairs with the nearer QSOs at $1.8 < z < 4.0$. They find 17 such LLS in transverse pairings which they argue is larger than the

number seen along LOS by factors of 4–20 times. Hennawi et al. (2006a) air their concern over the level of completeness and the false positive rate in their samples, since it is hard to find Ly α lines with $\log N_{\text{H}_I} > 18.3$ or 19.3 cm^{-2} in low-S/N moderate resolution spectra, and the reality of an excess depends on the precise minimum N_{H_I} values, and the number of false high column systems in their sample. Like Bowen et al. (2006), they suggest that absorbers are anisotropically distributed. Hennawi & Prochaska (2007) suggest that the LLS absorbers in the LOS are photoevaporated while those in the transverse direction are not evaporated because they do not see the full QSO UV flux.

1.3 Distances

We will measure separations in various units. The separations of sightlines in the plane of the sky are known in arcseconds. The errors on these separations are probably less than 1 arcsec, but they will be larger when the QSOs lack modern position measurements, or when the two QSOs were measured in different coordinate reference frames. We use a flat cosmological model with $\Omega_\Lambda = 0.73$, $\Omega_m = 0.27$ and $H_0 = 71 \text{ km s}^{-1} \text{ Mpc}^{-1}$, and we will use proper, not comoving, distance.

We convert from arcsec into proper Mpc in the plane of the sky using

$$b = \frac{c \delta\phi}{(1+z)H_0} \int_0^z \frac{dz}{\sqrt{\Omega_m(1+z)^3 + \Omega_\Lambda}}, \quad (1)$$

where b is the transverse proper distance in the plane of the sky, an impact parameter corresponding to the angular separation $\delta\phi$ in radians, measured at redshift z . The b parameter is the proper equivalent of the comoving r_p often seen in galaxy literature. For our cosmological model we have

$$b = \frac{0.020\,471\delta\theta}{(1+z)} \int_0^z \frac{dz}{\sqrt{0.27(1+z)^3 + 0.73}}, \quad (2)$$

where $\delta\theta$ is the angular separation of the QSOs in arcseconds, and the integral is 0.445 67, 0.785 66, 1.242 23, 1.530 38 for $z = 0.5, 1, 2, 3$. Jakobsen et al. (2003, equations 1 and 2) and Pen (1999) give analytic approximations, and Wright (2006) gives a JAVA calculator. We do not use the formulae given by Liske (2000) that are required for large angles or large redshift differences.

Distances along the LOS are most conveniently expressed as differences of redshift. When we discuss correlations in the positions of absorbers, we are interested in scales of about 1 Mpc or 100–400 km s⁻¹ depending on the redshift. These correlations will include higher density regions that will be expanding less rapidly than the Hubble flow, and some of them may be bound with constant proper size.

We shall convert the differences in redshift into velocity intervals using

$$\frac{v}{c} = \frac{(1+z_1)^2 - (1+z_2)^2}{(1+z_1)^2 + (1+z_2)^2}, \quad (3)$$

which for small intervals is approximately $v/c = H(z)d/c \simeq \Delta z/(1+z)$. We can convert these velocities into proper distances d using $v = H(z)d$ where $[H(z)/H_0]^2 = (1+z)^3\Omega_m + \Omega_\Lambda$ for our flat model and $H(z) = 120.70, 201.069, 301.31$ and 416.91 km s^{-1} at $z = 1, 2, 3$ and 4.

Conversion of small velocity intervals along the LOS into Mpc will be highly inaccurate because of systematic and random peculiar velocities (Kaiser 1988; McDonald 2003; Kim & Croft 2007). The effect of peculiar velocities has been studied in detail for H_I Ly α

absorption from the IGM (Hui, Stebbins & Burles 1999; McDonald & Miralda-Escudé 1999; Rollinde et al. 2003). We discuss these redshift-space distortions again in Sections 7 and 8.

2 QSO TARGETS

We use spectra of the 310 QSOs which include 140 pairs and 10 triplets. We treat each triple as three pairs, giving 170 QSO-to-QSO pairings. We selected these QSOs because their separations and redshifts are suitable for studying the correlations in the H_I absorption in the Ly α forest. When choosing objects to observe we initially observed all known pairs separated by under a few arcminutes. Later, as more pairs were announced by 2dF Quasar Redshift Survey (Boyle et al. 1997; Shanks et al. 2000; Miller et al. 2004) and SDSS (York 2000), we strongly biased our observing to the closest known suitable pairs, typically those within 120 arcsec. We also strongly biased our sample to pairs with similar emission redshifts, z_{em} , to maximize the redshift of overlap in the region between Ly α and Ly β in the paired spectra. However, some of the pairs discussed here do have widely differing z_{em} values. We also biased the sample against pairs where C_{IV} BAL absorption was at z_{abs} values that would put Ly α at rest wavelengths 1070–1170 Å, the key wavelengths for correlations of Ly α in the Ly α forest. Hence the sample contains less than the normal number of BAL QSOs, though there remain 34 BAL systems in 29 of the QSOs, especially weak BAL systems and systems restricted to z_{abs} similar to z_{em} . If we knew from SDSS spectra that a QSO in a pair had strong and widespread BAL absorption then we typically did not obtain new spectra of higher resolution or higher signal-to-noise ratio (S/N) to cover the Ly α forest at wavelengths <3900 Å that were not covered by the SDSS spectra.

In Table 1 we list the J2000 coordinates of the 310 QSOs, their z_{em} values, and the separation from the partner QSO in arcseconds. We give each QSO a label comprising a ‘P’, a number, and a letter. The number identifies the pair and the letter ‘a’, ‘b’ or ‘c’ the QSO in that pair or triple. We show the label in bold face when that QSO is part of a triple. The angles listed are from the current QSO to the next QSO in the sequence b, c then a; hence QSO P8c is 217 arcsec from P8a. The order of the QSOs in this table is not random and mostly relates to when we obtained spectra.

In Fig. 1 we show the distribution of the QSO pair separations in arcseconds and in proper Mpc.

In Fig. 2 we show the proper distance between two sightlines separated by 150 arcsec, the typical separation for our sample, as a function of z . The sightlines reach a maximum separation at $z = 1.644$. We will consider absorption systems at a wide range of z_{abs} values, including low redshifts where the proper distances are much less than 1 Mpc.

2.1 Emission redshifts

The average emission redshift of the QSOs is $z = 2.470$, with a range of 1.84–3.84. We measured the peak wavelengths for Mg II, C IV and Ly α emission lines in the available spectra. We selected the redshifts to use in this paper following the procedure in Kirkman, Tytler & Gleed (2008). If our spectra cover Mg II, we use the redshift from that line alone. Otherwise, if our spectra cover C IV, we use a redshift for C IV alone and we reduce that redshift by subtracting 753 km s⁻¹ that is the mean velocity difference of C IV from Mg II that Kirkman et al. (2008) found in 130 of the pairs used here. Otherwise, we use an Ly α redshift and subtract 475 km s⁻¹. For 74 of the 310 QSOs we did not measure any of the emission-line

Table 1. QSO targets. In order of QSO pair label number, not RA.

RA (J2000)	Dec. (J2000)	z_{em}	Label	Separation (arcsec)
00 44 34.08	+00 19 03.5	1.878	P1a	88.64
00 44 39.33	+00 18 22.8	1.866	P1b	
00 55 57.46	-32 55 39.0	2.250	P2a	122.53
00 56 05.33	-32 56 51.1	2.125	P2b	
02 09 54.8	-10 02 23.0	1.970	P3a	12.04
02 10 00.1	-10 03 54.0	1.976	P3b	
02 56 42.6	-33 15 21.0	1.915	P4a	55.78
02 56 47.02	-33 15 27.0	1.863	P4b	
03 10 06.08	-19 21 24.9	2.144	P5a	60.27
03 10 09.05	-19 22 08.1	2.122	P5b	
03 10 36.47	-30 51 08.4	2.554	P6a	72.04
03 10 41.06	-30 50 27.5	2.544	P6b	
09 14 04.1	+46 10 44.9	2.180	P7a	64.59
09 14 10.3	+46 10 50.01	2.370	P7b	
09 56 58.73	+69 38 52.5	2.048	P8a	130.92
09 57 21.22	+69 37 54.5	2.054	P8b	108.83
09 57 25.94	+69 36 08.5	2.048	P8c	217.08
11 45 47.55	-00 31 06.7	2.043	P9a	149.34
11 45 53.67	-00 33 04.5	2.055	P9b	
12 12 51.14	-00 53 42.2	2.473	P10a	74.01
12 12 56.06	-00 53 36.5	2.459	P10b	
13 06 34.19	+29 24 43.1	1.960	P11a	27.82
13 06 35.41	+29 25 05.9	1.926	P11b	
13 21 47.86	+01 06 04.8	2.130	P12a	107.86
13 21 54.33	+01 06 51.9	1.971	P12b	
13 39 39.0	+00 10 22.0	2.122	P13a	101.69
13 39 45.4	+00 09 45.0	1.869	P13b	
13 46 21.4	-00 38 05.0	1.894	P14a	119.62
13 46 25.6	-00 39 47.0	1.848	P14b	
14 12 24.51	-01 56 34.0	1.916	P15a	112.60
14 12 29.73	-01 55 13.1	2.030	P15b	
14 20 45.98	-00 05 18.0	2.193	P16a	299.36
14 20 55.61	-00 09 40.0	2.193	P16b	
16 12 37.9	+23 57 09.0	2.014	P17a	117.22
16 12 45.6	+23 58 00.0	2.005	P17b	
16 45 01.09	+46 26 16.0	3.790	P18a	195.32
16 45 19.62	+46 25 38.3	3.831	P18b	
17 27 56.45	+58 21 55.7	2.368	P19a	111.58
17 28 06.77	+58 20 39.19	2.011	P19b	
17 30 14.71	+54 56 57.5	2.127	P20a	244.99
17 30 42.38	+54 56 01.1	2.112	P20b	
17 36 26.73	+55 27 20.7	1.822	P21a	101.46
17 36 35.51	+55 28 29.4	1.988	P21b	
22 39 41.75	-29 49 55.2	2.101	P22a	154.98
22 39 48.64	-29 47 48.7	2.068	P22b	63.52
22 39 51.82	-29 48 37.0	2.121	P22c	152.44
23 09 11.88	-27 32 27.1	1.930	P23a	49.52
23 09 15.34	-27 32 45.3	1.927	P23b	
23 26 03.52	-29 37 40.4	2.310	P24a	141.22
23 26 14.26	-29 37 22.3	2.387	P24b	
09 09 23.13	+00 02 03.9	1.889	P25a	14.99
09 09 24.01	+00 02 11.0	1.866	P25b	
11 07 25.70	+00 33 53.6	1.883	P26a	24.82
11 07 27.08	+00 34 07.3	1.882	P26b	
14 35 06.42	+00 09 01.5	2.378	P27a	33.24
14 35 08.32	+00 08 44.4	2.378	P27b	
15 48 40.77	+53 37 08.59	2.165	P28a	126.11
15 48 50.17	+53 38 43.0	2.188	P28b	
23 01 12.42	-31 43 45.0	1.977	P29a	67.84
23 01 17.62	-31 43 59.2	2.132	P29b	
00 45 26.49	-32 00 16.91	1.885	P30a	79.62
00 45 27.54	-32 01 35.4	1.988	P30b	
01 24 56.45	-28 51 21.0	1.992	P31a	100.69
01 24 53.09	-28 52 51.5	2.094	P31b	

Table 1 – *continued.*

RA (J2000)	Dec. (J2000)	z_{em}	Label	Separation (arcsec)
01 35 14.53	-00 53 18.9	2.111	P32a	258.23
01 35 21.00	-00 57 18.2	2.075	P32b	
02 48 25.59	-28 03 55.4	2.139	P34a	193.83
02 48 40.13	-28 03 32.4	2.209	P34b	
21 36 19.40	+00 41 31.0	2.030	P35a	288.90
21 36 38.60	+00 41 54.0	1.941	P35b	
23 53 10.02	-27 26 14.09	1.968	P36a	40.35
23 53 13.03	-27 26 09.4	2.303	P36b	
00 08 52.71	-29 00 44.1	2.645	P37a	78.53
00 08 57.73	-29 01 26.9	2.610	P37b	
02 18 21.44	-29 53 40.9	2.070	P38a	21.97
02 18 22.96	-29 53 31.3	1.917	P38b	
03 06 40.91	-30 10 31.9	2.093	P39a	51.21
03 06 43.75	-30 11 07.49	2.129	P39b	
03 13 24.40	-31 41 44.9	1.954	P40a	17.00
03 13 25.51	-31 41 54.3	2.065	P40b	
03 33 20.90	-06 12 16.8	2.050	P41a	145.71
03 33 24.83	-06 10 03.4	2.139	P41b	
21 48 34.95	-29 41 09.9	1.807	P42a	26.74
21 48 36.61	-29 40 54.19	2.089	P42b	
22 32 20.27	-28 38 58.7	2.204	P43a	50.81
22 32 23.45	-28 38 29.9	2.065	P43b	
23 59 44.12	-00 57 38.16	1.778	P44a	46.15
23 59 45.48	-00 58 19.56	1.814	P44b	
00 59 34.10	-08 43 13.1	2.074	P45a	269.92
00 59 51.67	-08 44 23.8	2.142	P45b	
01 06 57.94	-08 55 00.1	2.354	P46a	181.93
01 06 58.41	-08 58 01.9	1.827	P46b	
03 40 23.50	+00 31 11.8	1.910	P47a	217.35
03 40 27.31	+00 34 41.5	1.874	P47b	
08 54 06.10	+42 38 10.0	2.387	P49a	283.22
08 54 15.40	+42 42 34.0	2.174	P49b	449.63
08 54 25.00	+42 35 17.0	1.850	P49c	271.04
10 05 38.50	+57 07 44.0	1.866	P50a	122.15
10 05 41.30	+57 05 44.0	2.306	P50b	
10 40 32.20	-27 27 48.6	2.331	P51a	291.12
10 40 33.50	-27 22 58.0	1.937	P51b	133.92
10 40 40.32	-27 24 36.4	2.460	P51c	220.51
10 41 21.90	+56 30 01.0	2.052	P52a	65.09
10 41 29.30	+56 30 23.0	2.267	P52b	
10 43 30.46	-02 30 12.7	2.246	P53a	258.44
10 43 42.53	-02 33 17.3	1.993	P53b	
11 06 10.70	+64 00 09.0	2.201	P54a	170.00
11 06 26.60	+63 57 55.0	1.960	P54b	
11 11 12.30	+01 22 01.6	2.417	P55a	91.33
11 11 14.11	+01 20 34.4	2.150	P55b	280.80
11 11 31.30	+01 22 25.0	2.010	P55c	285.96
11 19 22.40	+60 48 51.0	2.014	P56a	142.19
11 19 28.90	+60 46 37.0	2.293	P56b	164.79
11 19 31.10	+60 49 21.0	2.645	P56c	70.35
12 24 27.80	-11 20 50.0	2.495	P57a	253.03
12 24 41.40	-11 23 25.0	2.171	P57b	
13 31 25.93	+00 44 14.0	2.020	P58a	219.75
13 31 38.50	+00 42 21.1	2.429	P58b	252.96
13 31 50.51	+00 45 10.7	1.893	P58c	247.41
14 16 47.60	+63 02 51.0	2.034	P60a	284.83
14 16 50.80	+63 07 35.0	1.961	P60b	
14 26 05.80	+50 04 26.0	2.242	P61a	235.17
14 26 28.00	+50 02 48.0	2.324	P61b	
14 53 29.53	+00 23 57.3	2.538	P62a	259.89
14 53 37.99	+00 20 10.5	1.859	P62b	
14 58 38.04	+00 24 18.0	1.888	P63a	387.74
14 59 01.28	+00 21 23.7	1.988	P63b	180.73
14 59 07.19	+00 21 01.2	3.012	P63c	91.46

Table 1 – *continued.*

RA (J2000)	Dec. (J2000)	z_{em}	Label	Separation (arcsec)
15 22 43.99	+03 27 19.8	1.998	P64a	249.33
15 22 46.66	+03 31 25.9	2.287	P64b	
16 06 28.39	+17 31 26.0	2.040	P65a	265.05
16 06 37.60	+17 35 16.0	2.323	P65b	
16 32 52.30	+37.47 47.99	1.888	P66a	156.19
16 32 57.60	+37 50 11.0	2.152	P66b	
22 40 26.20	+00 39 38.0	2.200	P67a	213.50
22 40 40.10	+00 40 24.0	2.200	P67b	
23 31 32.84	+01 06 20.9	2.641	P68a	153.99
23 31 39.75	+01 04 27.0	2.245	P68b	
23 46 46.02	+12 45 30.18	2.763	P69a	334.44
23 46 28.21	+12 48 59.89	2.525	P69b	
20 45 33.15	-06 21 54.3	2.014	P70a	182.84
20 45 22.28	-06 23 19.0	2.157	P70b	
13 48 08.70	+28 40 07.0	2.464	P71a	59.09
13 48 04.40	+28 40 24.0	2.464	P71b	
09 00 06.90	+03 33 07	1.872	P72a	212.87
08 59 52.70	+03 33 18	2.163	P72b	
08 04 00.30	+30 20 46	3.446	P73a	269.22
08 03 42.00	+30 22 54	2.031	P73b	
15 45 44.20	+51 13 07	2.242	P74a	98.27
15 45 34.60	+51 12 28	2.453	P74b	
17 17 30.70	+26 22 27	2.203	P75a	211.93
17 17 15.20	+26 21 48	1.934	P75b	
17 29 43.36	+60 21 54.20	1.928	P76a	370.01
17 30 30.20	+60 19 47.40	2.215	P76b	
17 18 45.00	+30 26 47	2.028	P77a	160.61
17 18 37.20	+30 28 52	2.028	P77b	
17 28 40.02	+56 39 57.74	1.984	P78a	148.43
17 28 52.65	+56 41 43.58	1.769	P78b	
14 57 56.27	+57 44 46.90	2.130	P79a	73.63
14 57 47.55	+57 44 23.50	2.016	P79b	
15 34 12.70	+50 34 05	2.118	P80a	280.61
15 33 48.30	+50 31 28	2.215	P80b	
15 08 38.11	+60 35 40.10	2.179	P81a	120.46
15 08 27.67	+60 34 07.40	1.893	P81b	
16 50 51.10	+34 43 10	2.002	P82a	169.84
16 50 43.30	+34 45 30	1.984	P82b	
07 55 45.60	+40 56 43.61	2.348	P83a	138.18
07 55 35.61	+40 58 02.90	2.418	P83b	
11 09 52.30	+55 42 24	3.177	P84a	221.68
11 09 27.20	+55 41 20	3.472	P84b	
11 26 34.30	-01 24 36	3.741	P85a	278.71
11 26 17.40	-01 26 32	3.607	P85b	
12 19 33.26	+00 32 26.40	2.871	P86a	260.71
12 19 22.19	+00 29 05.40	2.627	P86b	
13 54 42.90	+59 28 56	2.554	P87a	161.67
13 54 38.40	+59 31 34	2.992	P87b	
14 19 19.50	+57 45 13	3.339	P88a	248.30
14 19 00.60	+57 48 30	2.937	P88b	
14 29 51.87	+63 16 31.90	2.403	P89a	188.86
14 29 33.01	+63 14 12.40	2.749	P89b	
14 35 00.27	+03 54 03.50	2.491	P90a	224.84
14 34 55.38	+03 50 30.90	2.853	P90b	
14 41 34.30	+61 39 19	2.435	P91a	296.10
14 40 52.90	+61 38 52	2.898	P91b	
15 59 22.70	+52 00 27	3.101	P92a	145.47
15 59 17.40	+52 02 44	3.042	P92b	
21 36 29.40	+10 29 52	2.555	P93a	237.83
21 36 15.40	+10 27 54	2.966	P93b	
08 25 50.20	+35 48 03	3.203	P94a	259.91
08 25 40.10	+35 44 14	3.846	P94b	
08 31 15.90	+38 14 24	3.073	P95a	216.00
08 30 53.00	+38 12 43	3.171	P95b	288.08

Table 1 – continued.

RA (J2000)	Dec. (J2000)	z_{em}	Label	Separation (arcsec)
08 30 52.90	+38 09 07	3.149	P95c	417.03
10 19 37.00	+55 23 55	3.231	P96a	125.37
10 19 22.90	+55 24 31	3.720	P96b	
11 08 19.15	-00 58 24.00	4.564	P97a	113.03
11 08 13.86	-00 59 44.50	4.033	P97b	
13 02 16.91	-03 38 03.70	3.714	P98a	141.24
13 02 08.17	-03 37 10.50	3.718	P98b	
13 48 08.79	+00 37 23.20	3.626	P99a	236.72
13 47 55.68	+00 39 35.00	3.814	P99b	
17 19 37.90	+29 18 05	3.079	P100a	106.46
17 19 32.90	+29 19 29	3.294	P100b	
20 53 03.70	-01 04 42	3.115	P101a	137.52
20 53 02.90	-01 02 25	3.251	P101b	
08 59 59.14	+02 05 19.70	2.980	P102a	275.29
08 59 56.83	+02 09 52.80	2.233	P102b	
13 37 57.87	+02 18 20.90	3.332	P103a	172.33
13 37 56.34	+02 15 30.10	2.314	P103b	
10 42 53.43	-00 13 00.90	2.958	P104a	289.81
10 42 43.12	-00 17 06.00	1.969	P104b	
09 45 08.00	+50 40 57	3.736	P105a	182.57
09 44 53.80	+50 43 00	3.789	P105b	
11 04 11.60	+02 46 55	2.533	P106a	131.25
11 04 03.00	+02 47 20	2.374	P106b	
13 12 13.84	+00 00 03.00	2.680	P107a	148.43
13 12 13.29	+00 02 31.20	2.842	P107b	
15 54 07.74	+01 00 10.10	2.606	P108a	239.10
15 53 59.96	+00 56 41.40	2.630	P108b	
01 06 16.06	+00 15 24.00	3.043	P109a	243.02
01 06 12.22	+00 19 20.10	3.110	P109b	
08 40 55.70	+37 04 37	3.152	P111a	178.10
08 40 42.20	+37 05 52	2.905	P111b	
13 24 11.60	+03 20 50	3.670	P112a	154.19
13 24 01.50	+03 20 20	3.371	P112b	
14 30 06.40	-01 20 20	3.249	P113a	199.75
14 29 57.10	-01 17 57	3.111	P113b	
15 00 58.70	+61 45 06	2.587	P114a	287.78
15 00 23.50	+61 47 29	2.994	P114b	
15 37 29.50	+58 32 24	3.059	P115a	202.31
15 37 15.70	+58 29 33	2.590	P115b	
01 02 51.85	-27 53 03.30	1.768	P116a	81.11
01 02 57.35	-27 53 38.82	1.800	P116b	
15 19 13.29	+23 46 58.72	1.834	P117a	101.25
15 19 19.40	+23 46 02.00	1.903	P117b	
16 25 48.00	+26 44 32.50	2.490	P118a	146.44
16 25 48.75	+26 46 58.60	2.526	P118b	180.33
16 25 57.66	+26 44 43.40	2.605	P118c	129.86
21 42 25.90	-44 20 17.00	3.230	P119a	61.52
21 42 22.20	-44 19 30.00	3.220	P119b	
21 43 07.01	-44 50 47.60	3.250	P120a	33.15
21 43 04.09	-44 50 36.00	3.060	P120b	
09 45 05.93	-00 46 45.00	2.299	P121a	261.94
09 44 54.24	-00 43 30.40	2.292	P121b	
09 27 43.02	+29 07 34.7	2.2530	P122a	57.60
09 27 47.27	+29 07 20.7	2.2920	P122b	
11 51 38.05	+02 06 10.30	2.258	P123a	260.18
11 51 22.14	+02 04 26.30	2.401	P123b	
14 11 08	+62 24 52	2.264	P124a	200.66
14 11 30.7	+62 22 48	2.305	P124b	
09 46 42.43	+33 07 54.8	2.477	P125a	194.21
09 46 56.17	+33 06 25.8	2.484	P125b	
08 33 21.61	+08 12 38.3	2.518	P126a	208.57
08 33 26.82	+08 15 52.0	2.572	P126b	
10 00 52.21	+45 00 11.0	2.567	P127a	199.33
10 00 54.38	+45 03 29.0	2.649	P127b	

Table 1 – continued.

RA (J2000)	Dec. (J2000)	z_{em}	Label	Separation (arcsec)
09 35 31.84	+36 33 17.6	2.858	P128a	231.84
09 35 48.51	+36 31 21.9	2.977	P128b	
14 22 49.19	+42 02 46.2	3.071	P129a	106.87
14 22 39.88	+42 02 20.4	3.236	P129b	
12 09 17.94	+11 38 30.4	3.105	P130a	196.41
12 09 10.71	+11 35 45.2	3.122	P130b	
08 52 32.18	+26 35 26.2	3.208	P131a	170.86
08 52 37.94	+26 37 58.6	3.29	P131b	
08 03 05.84	+50 32 15.3	3.244	P132a	190.91
08 03 21.24	+50 34 17.4	3.245	P132b	
12 38 15.04	+44 30 26.2	3.254	P133a	232.24
12 38 31.46	+44 32 58.2	3.268	P133b	
08 36 59.84	+35 10 19.4	3.319	P134a	269.47
08 37 00.83	+35 05 50.2	3.311	P134b	
14 21 49.99	+46 59 38.6	3.678	P135a	201.85
14 22 09.71	+46 59 32.5	3.798	P135b	
10 54 16.47	+51 27 24.6	2.367	P136a	238.50
10 54 16.51	+51 23 26.1	2.341	P136b	
12 13 03.26	+12 08 39.2	3.384	P137a	137.99
12 13 10.72	+12 07 15.1	3.469	P137b	
10 39 41.49	+55 09 27.8	3.709	P138a	258.46
10 39 49.28	+55 13 37.5	3.851	P138b	
08 07 44.89	+23 48 25.7	3.745	P140a	225.90
08 07 35.01	+23 51 26.4	3.76	P140b	
22 47 21.06	-09 15 45.7	4.13	P141a	284.94
22 47 40.17	-09 15 11.8	4.167	P141b	
23 38 15.45	-10 19 17.2	2.279	P142a	281.75
23 37 56.58	-10 20 00.1	2.436	P142b	
14 34 08.31	+23 22 30.0	3.97	P143a	166.07
14 33 56.26	+23 22 22.8	4.16	P143b	
10 16 05.84	+40 40 05.8	2.99	P144a	68.24
10 16 01.50	+40 40 52.9	2.963	P144b	
13 56 07.50	+58 12 36.1	3.32	P145a	89.15
13 55 57.54	+58 13 18.0	3.371	P145b	
11 52 10.43	+45 18 25.8	2.282	P146a	113.40
11 52 00.54	+45 17 41.4	2.379	P146b	
15 09 25.64	+50 56 09.3	2.365	P147a	119.68
15 09 32.23	+50 57 51.5	2.343	P147b	
16 43 30.13	+30 55 41.8	2.703	P148a	244.49
16 43 41.28	+30 58 59.8	2.559	P148b	
09 16 11.02	+33 11 30.5	3.112	P149a	152.45
09 16 03.40	+33 09 31.8	3.153	P149b	
11 06 11.11	+13 56 00.0	3.908	P150a	101.72
11 06 16.68	+13 54 58.6	3.846	P150b	
08 15 14.28	+06 05 42.5	2.495	P151a	64.08
08 15 18.32	+06 06 04.3	2.529	P151b	
16 23 23.68	+33 12 32.6	2.411	P152a	103.69
16 23 24.76	+33 10 49.8	2.585	P152b	
11 43 16.98	+13 24 00.8	2.514	P153a	138.30
11 43 23.44	+13 25 42.0	2.515	P153b	
10 40 04.02	+32 21 50.6	2.609	P154a	191.02
10 40 19.09	+32 21 56.4	2.649	P154b	
11 16 10.68	+41 18 14.5	2.98	P155a	13.75
11 16 11.73	+41 18 21.5	2.971	P155b	

positions, primarily because of strong absorption in the emission-line peaks, and instead used values from the SDSS for 51 QSOs and from NASA/IPAC Extragalactic Database (NED) for the remaining 23. We did not apply any shifts to these z_{em} values.

We do not know the errors in these redshifts, but we shall see in Section 5.1 that the similarity of z_{em} and the z_{abs} values in partner QSOs suggests errors are $\sim 300 \text{ km s}^{-1}$ for some of the QSOs. The

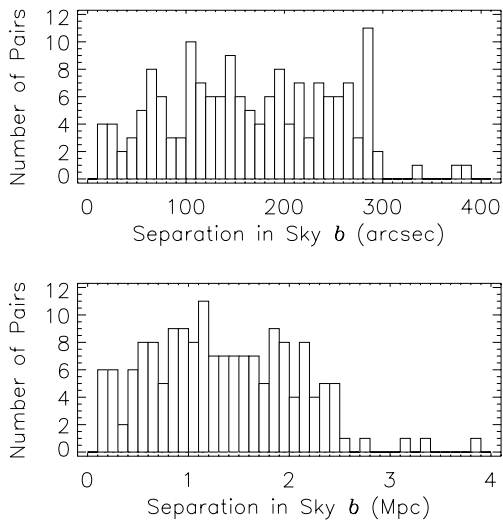


Figure 1. Separation of pairs of QSOs in arcseconds (upper, in bins of 10 arcsec) and proper Mpc in the plane of the sky, b (lower, in bins of 0.1 Mpc). We calculate the separation using the lower of the two z_{em} values. In this and many other figures we move the zero of the horizontal axis away from the vertical axis. The paired sightlines typically probe adjacent haloes, and small-scale galaxy clustering, and only occasionally do we probe the same halo with both sightlines.

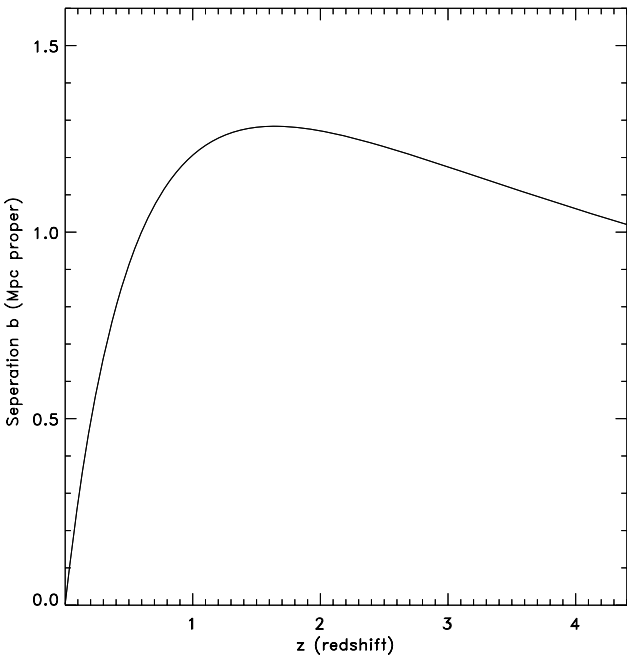


Figure 2. Proper distance between two sightlines separated by 150 arcsec as a function of redshift for the model we use in this paper with $\Omega_{\Lambda} = 0.73$, $\Omega_m = 0.27$ and $H_0 = 71 \text{ km s}^{-1} \text{ Mpc}^{-1}$.

errors may be several times larger for other QSOs, depending on the emission lines used to obtain the z_{em} values (Gaskell 1982; Tytler & Fan 1992; Vanden Berk 2001; Richards et al. 2002). The number of absorbers at negative velocities implies that z_{em} errors are typically less than 1000 km s^{-1} .

In Fig. 3 we show the distribution of the differences in the z_{em} values, where we define for each pair of QSOs

$$\Delta z_{\text{EE}} = |z_{\text{em1}} - z_{\text{em2}}|. \quad (4)$$

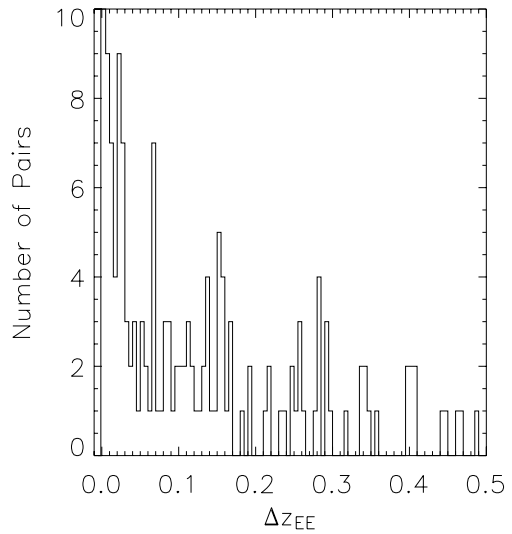


Figure 3. Distribution of the Δz_{EE} values, the difference between the z_{em} values of the QSOs in each pair, in bins of 0.005, or 500 km s^{-1} at $z = 2$.

There is a strong tendency for QSOs in the sample to have very similar z_{em} values, because most of the pairs with the smallest angular separation are physical pairings (Hennawi et al. 2006b; Shen et al. 2007), and because we favoured pairs with the most similar z_{em} values when we obtained spectra. Many pairs have $\Delta z_{\text{EE}} < 0.03$, or approximately 3000 km s^{-1} or 15 Mpc at the typical $z = 2$. This excess has a major effect on the correlation of z_{abs} values, because there is also an excess of absorbers with $z_{\text{abs}} \approx z_{\text{em}}$ in the individual sightlines.

3 OBSERVATIONS

We use spectra that we obtained with LRIS on the Keck I telescope, the Kast spectrograph on the Lick 3-m Shane telescope and from CTIO and KPNO. We also use spectra from the SDSS data release 5 (DR5).

We obtained spectra with LRIS (Oke et al. 1995; McCarthy et al. 1998) from 2001 to 2004 September. While we attempted to obtain spectra of a given pair on a given night, there are many cases where the partner spectrum was obtained on a different night or even a different year. The paired spectra then often have different resolution and wavelength coverage because LRIS changed.

In Table 2 we summarize the different grisms and gratings that we used with LRIS. The high-resolution 1200/3400 grism has the advantage of showing weak absorption lines, but it sometimes had lower efficiency than the low-resolution grism and it does not cover wavelengths 3880–4600 or 3770–4600 Å, a gap between the blue and red side spectra. For blue spectra the CCD was changed from B to A in 2002 June.

In Table 3 we list the wavelength ranges covered by the various CCD, grating and grism choices and the FWHM resolution for a given slit. Set-ups A, B and C are for LRIS on Keck, and D is for RCSP on the CTIO and KPNO 4-m telescopes. The resolution of individual spectra differs, even when we use the same gratings and slit, because of differences in the focus, seeing and guiding.

We give more details on the individual spectra in Appendix A. We show example spectra in Kirkman et al. (2008).

Table 2. Properties of the LRIS CCDs, grisms and gratings.

CCD used					
A	blue: two Marconi 2048 × 4096 CCDs 15 μm pixels				
B	blue: SITE 2048 × 2048 engineering grade CCD				
C	red: Tektronix 2048 × 2048 CCD 24 μm pixels				
	Blue grism ^a Red grating ^a				
1	1200/3400				
2	400/3400				
3	600/5000				
4	900/5500				
5	600/4000				

^aGrooves per mm/blaze wavelength (Å).

Table 3. Spectra characteristics.

Set-up	Wavelength range (Å)	Pixel (Å)	Slit (arcsec)	FWHM (Å)	FWHM (km s ⁻¹)	N ^a
A1	3200–3880	0.24	0.7	0.98 ^b	83 ^c	26
A1	3200–3880	0.24	1.0		108 ^d	27
A1	3200–3880	0.24	1.5		162 ^d	4
B1	3000–3770	0.41	0.7		105 ± 10 ^{e,f}	13
A2	3180–5800	1.07	0.7	4.21 ^b	281 ^c	7
B2	3000–5300	1.46	0.7		260 ± 30 ^{e,g}	21
C3	5500–8070	1.28	0.7	3.59 ^h	166 ^c	14
C4	4600–6330	0.85	0.7	2.39 ^h	131 ^c	53
C4	4600–6330	0.85	1.0	3.10 ^h	170 ^c	29
C4	4600–6330	0.85	1.5		255 ⁱ	4
D1 ^j	3180–6240	1.01	—	3.2	199 ^c	2
D2 ^k	1600–4720	0.52	—	3.2	234 ^c	2
D3 ^l	3150–4720	0.76	—	1.8	135 ± 10 ^e	3
D4 ^l	3600–6700	1.01	—	3.2	163 ^c	4
SDSS	3800–9200	0.90			165.5	164
LICK	3175–5880	1.15	2.3		250 ^e	45

^aN is the number of spectra with that set-up. ^bValues from Chuck Steidel 2002 July on LRIS web site: http://www.astro.caltech.edu/~ccs/lrisb/new_numbers.txt. ^cConverted from the FWHM in Å at the central wavelength of the spectrum, or the central wavelength to the red of Ly α emission when only one or two pairs of QSOs, or using 6500 Å for C3. ^dGuessed value. For the 1.0 arcsec slit we multiply the value for A1 by 1.3, the factor increase reported by Tonry (1998, section 2) for the 600 grooves mm⁻¹ grating. For the 1.5 arcsec slit we multiply the 1.0 arcsec value by 1.5. ^eMeasured by comparing the Ly α forest in Keck HIRES spectra of bright QSOs, following Suzuki et al. (2003). ^fConstant from 3200 to 3600 Å. ^gDecreasing from 300 km s⁻¹ at 4350 Å to 235 km s⁻¹ at 5320 Å. ^hFrom Tonry (1998, section 2) for the 600 grooves mm⁻¹ grating and times 2/3 for the 900 grooves mm⁻¹. ⁱGuessed value. We multiply the value for the 1.0 arcsec slit by 1.5. ^jCTIO 4-m RCSP KPGL-1 632 grooves mm⁻¹ grating blazed at 4200 Å. ^kAs D1 and including an HST FOS G270H spectrum. ^lKPNO 4-m RCSP BL 420 grating with 600 grooves mm⁻¹ and blazed at 8000 Å.

4 ABSORPTION SYSTEMS

We take care to describe the types of absorption systems that we see in the spectra since the spectra have various resolutions, wavelength coverage and S/N, all of which have a major effect on whether we detect an absorption system at a given z_{abs} value. We describe the procedure, what we found and what we could have found.

We began by looking for absorption to the red of the Ly α emission where we expect only metal ions. We identify many systems from the doublet lines and we then searched for other ions and Ly α

absorption at the same redshift. We believe that all the absorption systems are reliable, including those with a single doublet. The least reliable are those with weak N V alone, on the red side of the peak of the Ly α emission line where the flux changes rapidly.

We fit the absorption lines with Voigt profiles convolved to the spectral resolution. At the resolution of these spectra some lines are approximately a single unresolved Gaussian, but many others show velocity structure. If the velocity structure is clearly resolved, we list separate z_{abs} values for each component. When components are not well resolved, which in practice means velocity separations less than the FWHM of the spectrum, we select a single redshift for all the lines. We do not average the velocities of the components, but rather we seek to identify a single component, that with the largest column density. If all the lines are single components, we chose the z_{abs} of the line that is the best defined and most like a single Voigt profile. If we see multiple velocity components, we take the z_{abs} from the strongest component, often seen by its presence in a transition with a smaller oscillator strength. When we see many ions each with components we choose the ion with the least components and the location of the highest optical depth.

In Table 4 we list the 690 metal-line redshift systems that we found, including 34 that we will classify as BAL. We give their z_{abs} values, the ions we saw and the rest-frame equivalent widths W_{rest} values for the stronger lines in the doublets; λ1548.19 Å for C IV, λ1238.82 for N V and λ2796.35 for Mg II. We list the W_{rest} for C IV if available, else Mg II, and failing those two, N V. We give W_{rest} for 593 non-BAL systems, less than the 656 total number of non-BAL systems, since we did not measure any lines for some systems because of low S/N, or a lack of unblended C IV, Mg II or N V. We also list under the heading W_{pm} the approximate minimum W_{rest} value that we could have seen in the partner spectrum at that redshift and for the same ion, where a value of −1 means that that ion could not be seen and hence there is a significant chance that the system would not be detected in any ions. The list is in order of z for each pair, including the z_{em} values, to make it easier to see coincident redshifts.

In Fig. 4 we show the broad distribution of z_{abs} values, with a range from 0.2 to 4.0 and a mode of 2.0.

The effective mean FWHM of our sample is less than 170 km s⁻¹. This is the mean FWHM value from Table 3 weighted by the number of QSOs with that FWHM. In Table 3 the N parameter gives the number of spectra with each resolution. We multiply these numbers by two for all set-ups where we list only one set-up (D1, D2, D3, D4, SDSS and Lick). This mean is larger than the effective FWHM value because we expect to see more absorption systems in spectra with smaller FWHM values.

In Fig. 5 we show the distribution of the separations of the absorption systems in individual LOS. We see only three pairs of systems with separations of less than 200 km s⁻¹, consistent with an effective resolution of near 170 km s⁻¹.

In Table 4 we mark the 34 systems that we consider to be BAL, because they show strong wide C IV lines. We arbitrarily choose to call BALs all systems with a total rest-frame equivalent width for 1548 Å and 1550 of C IV $W_{\text{rest}}(\text{CIV}) > 5$ Å. We find that 32 of the QSOs contain one or more BAL systems. We will present separate analysis for the BAL systems because they are located near to their QSOs and not at the distance suggested by their z_{abs} . We exclude the BAL systems from our main analysis.

In Table 5 we list the number of times that we see each ion, N_{tot} , and the fraction of the absorption systems f_{tot} that show each ion. These distributions resemble those seen in other samples, such as table VI of Barthel, Tytler & Thomson (1990). Compared to

Table 4. The 690 metal-line absorption systems in the spectra of the 310 QSOs. QSO coordinates are in Table 1. Definitions are in Section 5.2 for EA and EAV, and Section 5.3 for AA, AAV and AAA. We give five decimal places for the redshifts of the coincident absorption systems, and four decimals for most other absorbers. We discuss errors on redshifts in Table 8 and Section 9. We comment on individual coincident systems in Appendix A. W_{rest} is the rest-frame equivalent width for one of the stronger doublet lines (1548, 2796 or 1238) in order of preference, and W_{pm} is the minimum W_{rest} (\AA) that we could have seen for the same line in the spectrum of the partner QSO at the same z .

QSO	z	Ions or z_{em}	Notes	W_{rest}	W_{pm}
P1 a	0.9397	Mg II, Fe II		2.29	0.08
P1 b	1.0091	Mg II, Fe II		0.68	0.10
P1 a	1.1355	Mg II, Fe II		1.59	0.10
P1 b	1.4267	C IV, Mg II		0.68	0.15
P1 a	1.541	Mg II		0.31	0.20
P1 b	1.7244	H I, C II, C IV, Si II, Si III, Si IV, Al II, Al III, Mg II, Fe II		0.86	0.15
P1 b	1.7584	C IV		0.39	0.15
P1 b	1.85837	H I, C IV, Si IV	AAA21	0.62	0.18
P1 b	1.866	z_{em}	EA1		
P1 a	1.86730	H I, N V ² , C IV	EA1 AAA21	0.38	0.10
P1 a	1.878	z_{em}			
P2 a	2.1142	H I, C IV, Si IV		0.63	0.10
P2 b	2.125	z_{em}			
P2 a	2.2193	H I, C IV, Si IV		1.05	0.10
P2 a	2.250	z_{em}			
P3 a	0.96767	Mg II, Fe II	AA1	1.29	0.10
P3 b	0.96770	Mg I, Mg II, Fe II	AA1	1.33	0.10
P3 b	1.0322	Mg II		0.26	0.10
P3 b	1.5483	C IV ²		0.34	0.30
P3 b	1.7854	H I, C IV, Si III, Si IV		0.50	0.25
P3 a	1.954	N V, C IV, Si IV	BAL	11.3	0.15
P3 a	1.970	z_{em}			
P3 b	1.976	z_{em}			

Full version of this 11-page table is in the electronic version of the paper.

Milutinovic et al. (2007) who examined systems at $z_{\text{abs}} \simeq 1$ in high-resolution *Hubble Space Telescope* (*HST*) spectra, we see fewer ions per system, and fewer instances of most ions.

In addition to the BAL systems, we expect that other systems, especially those with $z_{\text{abs}} \sim z_{\text{em}}$ will be intrinsic to the QSOs and not at the distances from the QSOs implied by their z_{abs} values (Misawa et al. 2007; Ganguly & Brotherton 2008; Wild et al. 2008). We make the following definition to help isolate such systems.

Associated absorbers are at velocities $< 3000 \text{ km s}^{-1}$ in the frame of the z_{em} value of their QSOs.

We will explicitly state when we include or exclude associated systems from the samples that we analyse.

5 ANALYSIS OF NON-BAL METAL-LINE ABSORPTION SYSTEMS

In this section we examine the distribution of the absorbers relative to each other and relative to the emission redshifts. We look for

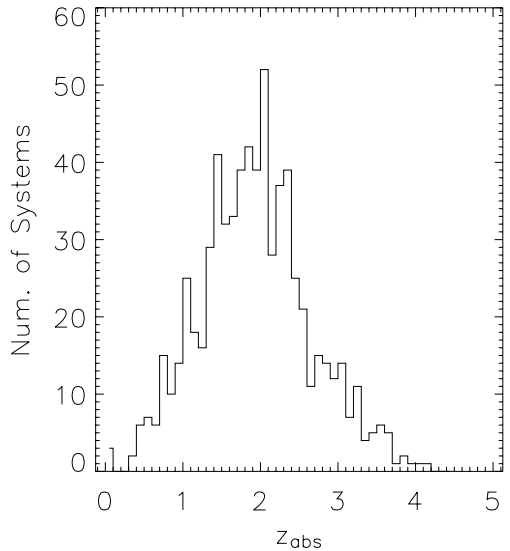


Figure 4. Distribution of all z_{abs} values, the absorption redshifts of the lines we observed, in bins of size 0.01.

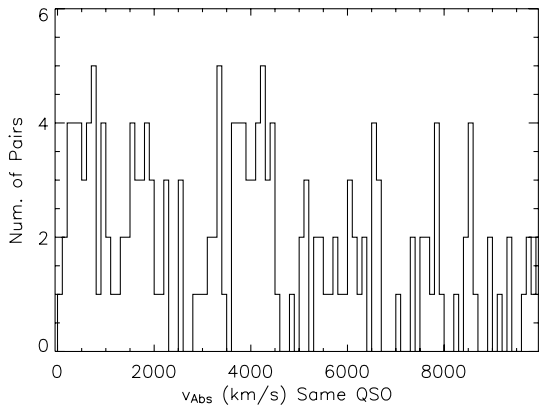


Figure 5. The distribution of redshift differences of absorption systems in individual QSOs. We include associated absorbers and we use bins of 100 km s^{-1} .

correlations along the individual sightlines and especially between the sightlines. We work in both redshift and velocity along the LOS. We will see that many of the systems have $z_{\text{abs}} \sim z_{\text{em}}$. We will see significant correlation between absorbers in the paired sightlines and between absorbers in one sightline and the z_{em} in the other sightline.

Many of our results on the distribution of the absorption and emission redshifts are shown in the five panels of Fig. 6 and the related panels of Fig. 7 that we will discuss and compare one by one. The panels of Fig. 7 are close-ups of the panels from Fig. 6, using the relative velocity instead of redshift differences. The histogram bin size is five times smaller in Fig. 7 for $z = 2$. We include QSOs with BAL absorption, because a large fraction of the QSO groupings, 29/140, show one or more BAL systems; but we exclude the BAL systems themselves.

5.1 Absorbers distributed along individual lines of sight

In Fig. 6(a) we show how the absorbers are distributed relative to the z_{em} of their QSO. For each absorption system we plot

Table 5. Ions seen in absorption systems. We counted the instances of ions in the 690 non-BAL, 34 BAL, 34 AA (both absorbers in each pair) and 16 EA systems, and we give fractions showing the ions for all except the BAL. We did not conduct a thorough search for ions other than C IV and Mg II. We only occasionally looked for ions such as Si III, O VI and C III with lines at rest wavelengths $< 1216 \text{ \AA}$.

Ion	N_{tot}	f_{tot}	N_{BAL}	N_{AA}	f_{AA}	N_{EA}	f_{EA}
C IV	419	0.607	30	24	0.706	14	0.88
H I	257	0.372	26	7	0.206	13	0.81
Mg II	192	0.278	0	12	0.353	0	0.00
Si IV	117	0.169	10	5	0.147	5	0.31
Si III	113	0.164	0	4	0.118	3	0.19
N V	106	0.153	24	2	0.059	2	0.12
Fe II	106	0.153	0	7	0.206	0	0.00
Si II	55	0.080	0	5	0.147	2	0.12
Al II	47	0.068	0	3	0.088	2	0.12
C II	44	0.064	0	3	0.088	0	0.00
O VI	30	0.044	15	2	0.059	0	0.00
Al III	17	0.025	0	2	0.059	2	0.12
O I	11	0.016	0	1	0.029	0	0.00
Mg I	6	0.009	0	1	0.029	0	0.00
C III	2	0.003	0	0	0.000	0	0.00
Ca II	1	0.001	0	0	0.000	0	0.00

$z_{\text{em}} - z_{\text{abs}}$, where both redshifts are from the spectra of the same QSO. We see approximately seven times more systems per bin with $z_{\text{abs}} \simeq z_{\text{em}}$ compared to $0.15 < (z_{\text{em}} - z_{\text{abs}}) < 0.3$. The excess is most conspicuous in three bins covering $-0.005 < z_{\text{em}} - z_{\text{abs}} < 0.025$ (2500 km s^{-1} for $z = 2$) and continues with lower amplitude to $z_{\text{em}} - z_{\text{abs}} \sim 0.1$ (10000 km s^{-1} at $z = 2$).

Fig. 7(a) shows the same data as Fig. 6(a) but in terms of velocity v_{abs} of the absorption system relative to the z_{em} of its QSO,

$$v_{\text{abs}} = c \frac{(1 + z_{\text{em}})^2 - (1 + z_{\text{abs}})^2}{(1 + z_{\text{em}})^2 + (1 + z_{\text{abs}})^2}, \quad (5)$$

where absorbers that appear to be falling into the QSOs have negative velocities. The v_{abs} values are approximately uniformly distributed from 0 to 2200 km s^{-1} , with the distribution peak at approximately $v_{\text{abs}} \sim 1300 \text{ km s}^{-1}$, and not at $v_{\text{abs}} = 0$.

The excess absorbers with $z_{\text{abs}} \sim z_{\text{em}}$ is similar to that reported by Weymann et al. (1981) for a sample like ours that does not use an equivalent width cut-off. The velocity range $-4000 < v_{\text{abs}} < 4000 \text{ km s}^{-1}$ includes 42 per cent of the Weymann et al. (1981) sample of C IV systems and 50 per cent of our mixed absorption systems. Samples that contain only lines with W_{rest} exceeding some fixed minimum show much smaller excesses (fig. 3 of Young et al. 1982 and fig. 2a of Sargent et al. 1988) because they exclude the additional absorption lines that are easiest to see in the regions with the highest S/N, especially in and near to the C IV emission line. Emission lines are made even more important for our relatively low-luminosity QSOs by the Baldwin effect.

5.2 Emission redshift errors and absorbers with negative velocities

Some QSOs show absorption with z_{abs} larger than their z_{em} with $v_{\text{abs}} > 1000 \text{ km s}^{-1}$. Peculiar velocities will account for many of the smaller ‘infalling’ velocities, but not the largest ones (Sargent, Boksenberg & Young 1982). We believe that when we see a large negative v_{abs} , the z_{em} value is too small by about $-v_{\text{abs}}$. This idea, due to Gaskell (1983), is credible because we know that large negative blueshifts of the C IV emission lines are common (Gaskell 1982;

Tytlér & Fan 1992; Richards et al. 2002). With this interpretation, the absorbers at negative v_{abs} values do not need special treatment, other than noting that their z_{em} values are too small.

The distribution of the velocities of the absorption systems in the frame of the QSOs give information on the z_{em} errors. In Fig. 7(a) we see only eight systems from 310 QSOs at velocities less than -1000 km s^{-1} . This suggests that z_{em} errors are typically less than 1000 km s^{-1} . We say more about z_{em} errors below.

5.3 Absorption in one QSO near the emission redshift of the partner: EA

We now discuss the absorption we see in the spectrum of a QSO when the LOS passes the partner QSO. Fig. 6(b) shows the distribution of Δz_{EA} values, where

$$\Delta z_{\text{EA}} = z_{\text{em}1} - z_{\text{abs}2}, \quad (6)$$

and the emission and absorption redshifts are from different QSOs in a pair. We see 16 absorbers where we expect 5.98 in the bin centred at zero, at $-0.005 < \Delta z_{\text{EA}} < 0.005$, or $\pm 500 \text{ km s}^{-1}$ at $z = 2$. Since the errors on the z_{em} values are likely in the range $400-800 \text{ km s}^{-1}$ or more, we expect any clustering of absorbers next to a QSO to be spread over the three bins covering $-0.015 < \Delta z_{\text{EA}} < 0.015$. Here we see 35 absorbers, where we expect 17.9 if the distribution were an extrapolation of a straight line fit to Δz_{EA} in the range 0.01–1.0. The probability of seeing ≥ 35 is then 0.0002. This low probability demonstrates that we see a real excess of absorbers. In Section 5.3.1 we show that this excess is not from the associated absorbers in the spectrum of the other QSO that congregate near $\Delta z_{\text{EA}} = 0$ because the paired QSOs have similar z_{em} values. Instead they are likely from galaxies near the QSOs.

On large scales, $0.10 < |\Delta z_{\text{EA}}| < 0.15$, we see more absorbers in front of the QSO (positive Δz_{EA}) than behind, because many of the paired QSOs have similar z_{em} values, giving a reduced sample size behind. We do not place any constraints on the relative values of the z_{em} of the paired QSOs.

In Fig. 7(b) we use velocity v_{EA} instead of redshift, where

$$v_{\text{EA}} = c \frac{(1 + z_{\text{em}1})^2 - (1 + z_{\text{abs}2})^2}{(1 + z_{\text{em}1})^2 + (1 + z_{\text{abs}2})^2}, \quad (7)$$

and the emission and absorption redshifts are again from the different QSOs in a pair. Fig. 7(b) shows that the excess is most conspicuous in only two bins that sample 0–200 and 400–600 km s^{-1} . We shall assume that it is an accident that the bin at 200–400 km s^{-1} contains no excess, and consider all three bins covering 0–600 km s^{-1} . These three bins contain 16 absorbers and the a posteriori probability of ≥ 16 is 0.0003, given that we expect 5.77, from a straight line fit to $600 < v_{\text{EA}} < 20000 \text{ km s}^{-1}$. This is similar to the probability that we obtained from Fig. 6(b) when we used a wider velocity range of approximately $\pm 1500 \text{ km s}^{-1}$.

Fig. 6(c) repeats the panel above, but now excluding all associated systems, those within 3000 km s^{-1} of the z_{em} . The excess near $\Delta z_{\text{EA}} = 0$ has gone leaving an approximately constant number of pairings at $-0.015 < \Delta z_{\text{EA}} < 0.6$. Fig. 7(c) shows the same for v_{EA} , again excluding associated absorbers.

The distribution of the excess absorbers around QSOs is of considerable physical interest. We fit the excess in the three bins covering 0–600 km s^{-1} in Fig. 7(b) with the sum of a straight line, with a height of 1.92 at the origin, plus a Gaussian with a mean of approximately 300 km s^{-1} and a standard deviation of 250 km s^{-1} .

Fig. 7(b) shows that all the excess absorbers are to the right-hand side of zero and hence in front of the QSOs. We see 16 absorbers

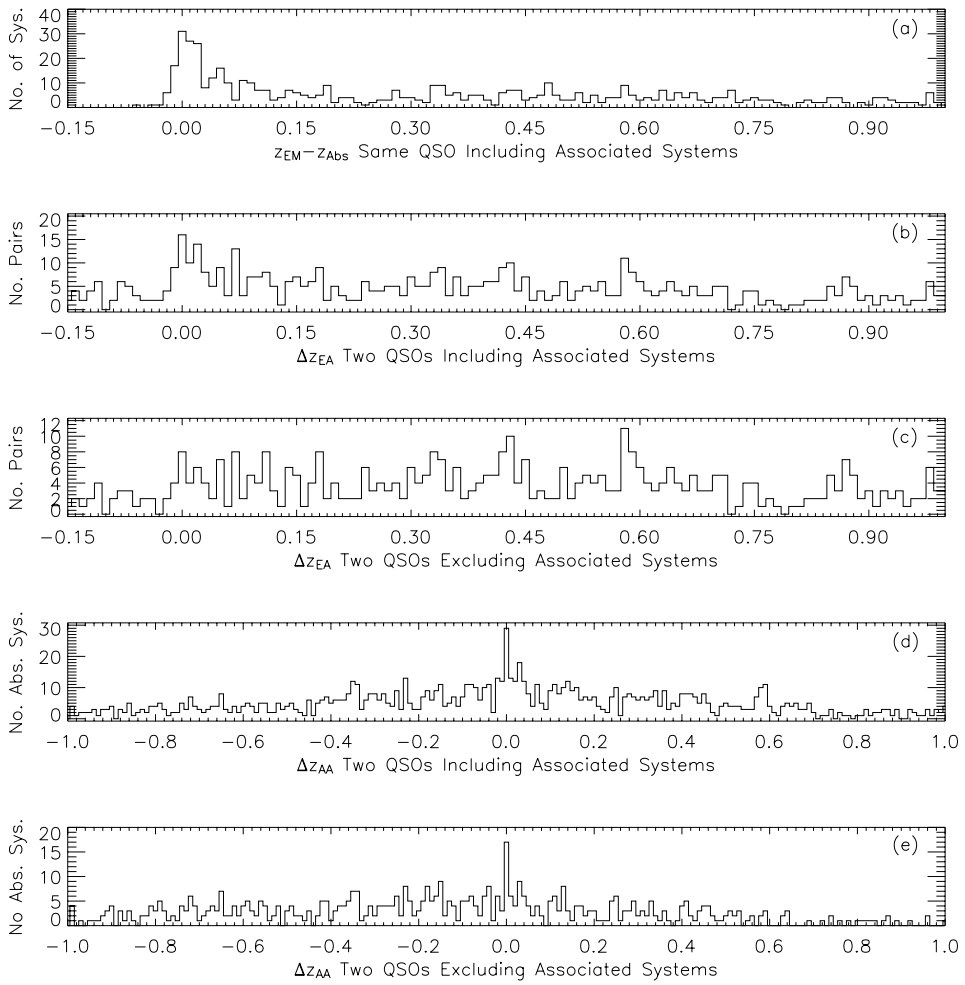


Figure 6. Histograms showing the distribution of redshift differences. The top panel shows the distribution of the redshift distance of the absorbers from the background QSO. The second panel shows the distribution of the distance from the foreground QSO of all the absorbers and (third panel) all the absorbers except the ones near the background QSO. The last two panels show the distribution of the absorber–absorber separation for all absorbers and for all absorbers except the ones near a QSO. The top panel (a) shows the distribution of $z_{\text{em}} - z_{\text{abs}}$ both from the same QSO. The second and third panels (b) and (c) take a z_{em} value from one QSO in a pair, and a z_{abs} value from the other QSO. The fourth and fifth panels (d) and (e) take one absorber from each QSO. In the second and fourth panels use all z_{abs} values, while the third and fifth panels use subsets that exclude all absorbers within 3000 km s^{-1} of their QSO’s z_{em} value. All bins have a width of $\Delta z = 0.01$, approximately 1000 km s^{-1} or 5 Mpc at $z = 2$.

in front at 0 – 600 km s^{-1} , compared to only six behind at -600 to 0 km s^{-1} . The level of significance of the asymmetry about zero is not high and depends on the range of velocities that we choose a posteriori. For the $n = 9$ velocities in the range $\pm 200 \text{ km s}^{-1}$, the mean velocity is $\bar{v} = 53.0 \text{ km s}^{-1}$ and the standard deviation $s = 115.5 \text{ km s}^{-1}$. The statistic $t = (\bar{v} - \mu)/(s/\sqrt{n})$ has a Student t -distribution with $(n - 1)$ degrees of freedom. The probability of exceeding this $t = 1.38$ value if the population mean $\mu = 0$ is 10 per cent. For the 22 velocities $\pm 600 \text{ km s}^{-1}$, the mean is 125.3 km s^{-1} , $s = 337.6$, $t = 1.74$ and probability is 4.8 per cent. For all 47 velocities in the range $\pm 2000 \text{ km s}^{-1}$, the mean is 213.2 km s^{-1} , $s = 1000.0$, $t = 1.46$ and the probability is 7.5 per cent.

5.3.1 Transverse associated absorbers

We now distinguish and discuss two possible explanations for the excess pairings of absorbers with z_{abs} similar to the z_{em} of the partner QSO.

(1) *Normal LOS associated absorbers*: These are the excess C IV absorbers at $v_{\text{abs}} < 3000 \text{ km s}^{-1}$ seen in individual LOS, and seen in Figs 6(a) and 7(a). Some of the excess pairings that we see in Figs 6(b) and 7(b) may be normal LOS associated absorbers that are selected because the QSO pairs often have very similar z_{em} values.

(2) *Transverse associated absorbers*: These are a new type of absorption connected to and near to the QSOs. Their existence was been established by the four Mg II pairings reported by Bowen et al. (2006) and probably also for LLS found by Hennawi & Prochaska (2007). These authors find more absorbers in the transverse compared to the LOS direction, direct evidence that the transverse associated absorbers are more than a subset of the LOS associated absorbers. A simple logical argument connects our sample to theirs. (1) The C IV absorbers we see, like all samples of strong C IV absorbers, include many Mg II systems and LLS. For example, of the 31 LLS with measured W_{rest} (1548) or limits in Sargent, Steidel & Boksenberg (1989, Tables 4, 6) we would have detected about 1/3 (seven have $W_{\text{rest}}(1548) > 0.7 \text{ \AA}$, 11 > 0.5 \AA and 13 > 0.4 \AA). We would also have detected three of the four Mg II systems, those with $W_{\text{rest}}(2796) = 1.10, 1.59$ and 1.90 \AA , that Bowen et al.

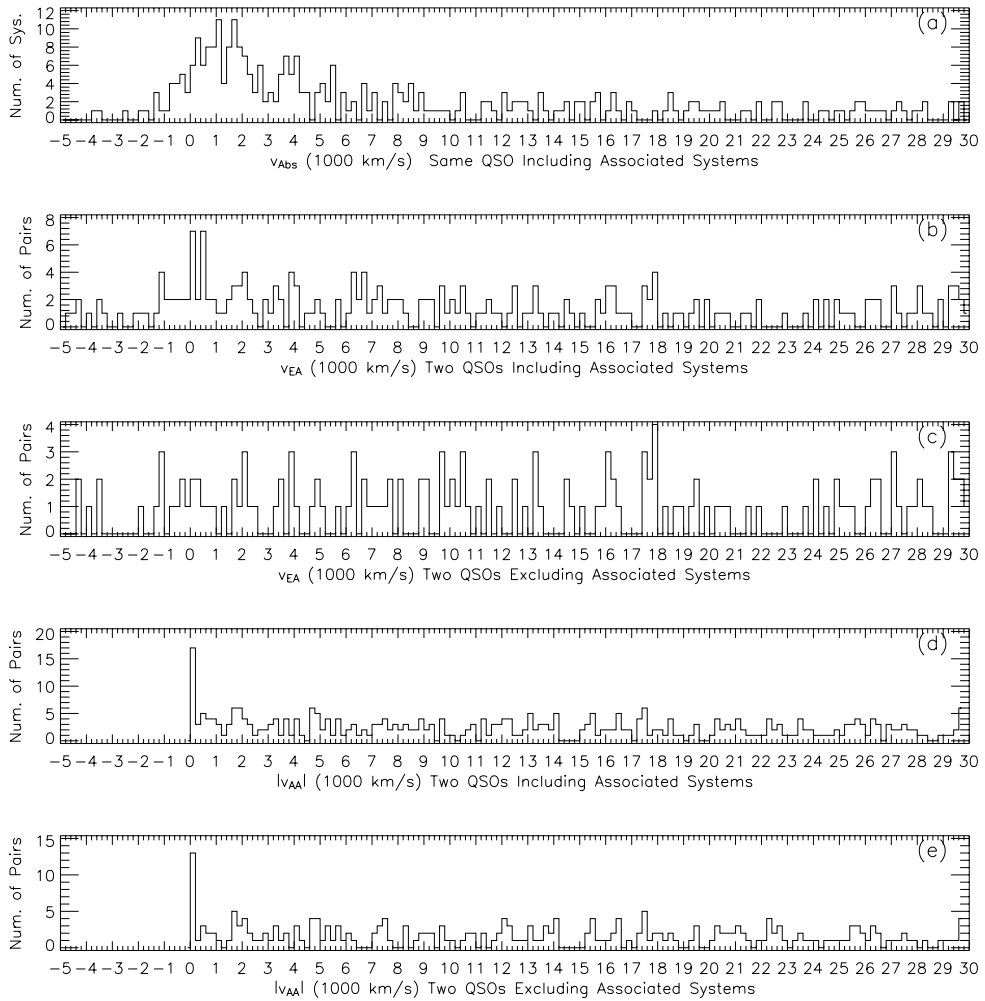


Figure 7. As Fig. 6 but using bins 200 km s⁻¹ wide, or approximately 1 Mpc at $z = 2$.

(2006, Table 1) saw. (2) The Bowen et al. (2006) and Hennawi & Prochaska (2007) sample contain Mg II and LLS, and they show the excesses transverse absorbers near QSOs. (3) Hence at least that part of our C IV sample that are Mg II systems or LLS will show the same types of excess transverse absorption, when the pairs have similar separations. While the Hennawi & Prochaska (2007) sample is intended to be entirely absorbers that are optically thick in the Lyman continuum (they use the Ly α line equivalent width to judge this), and three of the four Bowen et al. (2006) absorbers are also likely optically thick, our sample includes both optically thick and thin absorbers. Our sample is different from that of Bowen et al. (2006) because their impact parameters are all < 100 kpc where they can see absorption in the QSO host galaxy. We also differ from both these past studies in that they detected transverse absorbers from comparisons of the absolute number of absorbers in the LOS and transverse directions, while here we detect the transverse absorbers in their distribution in redshift.

We believe we also detect the transverse absorbers, because the distributions of absorbers in Figs 7(a) and (b) are different. We find similar results from three statistical tests. In Fig. 8 the probability of a difference larger than the $D = 0.2904$ observed at 539 km s⁻¹ between the two cumulative distributions is 0.009. The Wilcoxon rank U -statistic described by Kendall & Stewart (1979, sec-

tion 31.51) and Lupton (1993, section 15.3) gives a higher significance. Again for velocities ± 2000 km s⁻¹ the sum of the ranks of the v_{EA} velocities is 2882 giving $U = 1754$ which corresponds to a standard normal deviate of $z = -2.63$, significant at the 0.005, while for -1000 to 2000 km s⁻¹ we have a rank sum of 2306, $U = 1486$ and $z = 2.07$, significant at the 0.02 level.

Since the samples are not very small, we obtain similar results comparing the mean velocities [Lupton (1993, section 9.1) and Kendall & Stewart (1979, section 21.24)]. Let $v_a = s_a^2/(n_a - 1)$, where s_a^2 is the variance of the velocities from Fig. 7(a). The variance of the difference of the mean velocities $\bar{a} - \bar{b}$ is $S^2 = v_a + v_b$ and the statistic $z = (\bar{a} - \bar{b})/S$ is distributed approximately as Student t with $(v_a + v_b)^2/[v_a^2/(n_a - 1) + v_b^2/(n_b - 1)]$ degrees of freedom, for the two samples that may have different sample size and population variances. For velocities ± 2000 km s⁻¹, we have $z = 2.57$ with 82 degrees of freedom, which is significant at the 0.006 level, while for velocities -1000 to 2000 km s⁻¹ we have $z = 2.02$ for 68 degrees of freedom which is significant at the 0.024 level. We conclude that the absorbers near $v = 0$ in Figs 7(b) are not a random sample from the LOS absorbers seen in Figs 7(a). The excess of EA absorbers Fig. 7(b) are more concentrated around zero than are the normal LOS associated absorbers in Figs 7(a). There remains the possibility that the presence of associated absorbers in the sample has somehow confused this interpretation.

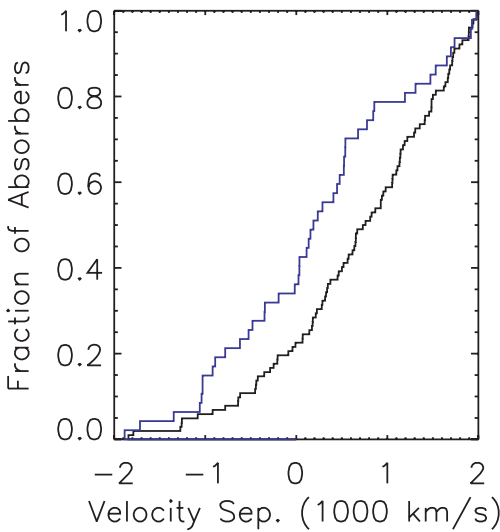


Figure 8. Cumulative distributions of the velocities from Figs 7(a) and (b), for the range -2000 to 2000 km s^{-1} . The lower curve (black) at zero on the horizontal axis shows the 102 velocities measured from their own QSO's z_{em} , the v_{abs} from Fig. 7(a). The upper curve (blue) is for the 47 velocities measured relative to the z_{em} of the partner QSO, v_{EA} from Fig. 7(b).

Sargent et al. (1988, fig. 2a) shows that the excess of LOS associated systems extends over about ± 2000 km s^{-1} in their complete sample. This is a larger range than the 0 – 600 km s^{-1} indicated for the coincidences in Figs 7 (b), and supports our belief that the transverse absorbers are more than a subset of the LOS associated absorbers. However, Sargent et al. (1988) measured z_{em} values using laboratory rest-frame wavelengths for emission lines of H I, N V, Si IV+O IV, C IV, and their QSOs are more luminous leading to less distinct emission lines, factors that might give larger errors in the z_{em} values and hence a wider range of v_{EA} for the excess C IV absorbers.

We suspect that many of the transverse absorbers that we see are in galaxies near the QSOs. We differ from Bowen et al. (2006) in that our separations are typically 1 Mpc, while theirs are only 0.026–0.097 Mpc. Our transverse absorbers do not arise in the QSO host galaxies but theirs might. Chelouche et al. (2008, fig. 8) shows a possible arrangement of the transverse absorbers.

We now define a new term.

(i) EA (emission-absorption) coincident absorbers are close to the emission redshift of the partner QSO, with $-0.005 < \Delta z_{\text{EA}} < 0.005$, which is the bin centred on zero in Fig. 6(b), covering approximately ± 500 km s^{-1} or 2.5 Mpc at $z = 2$. We include associated systems. We do not require that the absorber is in the QSO with the higher z_{em} value.

We see 16 EA coincidences that we mark EA1, EA2, in Table 4, and we give notes on each in Appendix A. In Table 6 we list some properties of these 16 EA coincident absorbers, including the separation in proper Mpc in the plane of the sky and in velocity.

For EA pairing P147 the absorber is in the QSO with the lower z_{em} value. The absorber is at $v_{\text{abs}} = -1630$ km s^{-1} and $v_{\text{EA}} = +24$ km s^{-1} . If both z_{em} values have negligible errors, this cannot be a physical coincidence. However, if the z_{em} value of the QSO showing the absorber is too low by ~ 1700 km s^{-1} , depending on peculiar velocities, we may still have a physical coincidence.

We add two more definitions that explore a larger range of separations, and focus on the velocities where we see the excess absorbers near the QSOs.

Table 6. EA emission-absorber coincidences. The first column gives the QSO that contributes the z_{em} value (listed in Table 4). The letter in front of the z_{abs} in the second column identifies the QSO that gives the z_{abs} value. Velocities are in (km s^{-1}) and v_{abs} is the velocity of the absorber in the frame of the z_{em} value of its QSO. The separation of the two sightlines in the plane of the sky is the b value in proper Mpc.

QSO em	QSO z_{abs}	Pair	v_{abs}	v_{EA}	b (Mpc)	W_{rest} (Å)
P18a	b 3.824 20	EAV21	466	-934	1.4089	0.24
P26b	a 1.890 84	EAV24	-918	-918	0.2114	0.80
P26b	a 1.889 51	EAV23	-781	-781	0.2114	0.80
P58a	b 2.033 55	EAV26	37 022	-619	1.8596	0.53
P8c	b 2.046 02	EAV20	1638	-524	0.9203	0.77
P64a	b 2.004 51	EA10	27 356	-481	2.1130	0.54
P24a	b 2.322 16	EA6	6311	-349	1.1731	0.35
P94a	b 3.207 84	EA12	42 349	-345	1.9944	1.0
P146a	b 2.313 54	EA14	7408	-193	0.9427	0.35
P153a	b 2.5178	EA16	-452	-17	1.1315	0.31
P147a	b 2.370 13	EA15	-1630	24	0.9907	0.28
P8a	b 2.051 15	EA3	1133	34	1.1069	0.52
P28a	b 2.168 63	EA7	2167	35	1.0589	2.72
P36a	b 1.966 88	EA8	32 575	113	0.3425	0.52
P38b	a 1.916 58	EA9	14 986	136	0.1869	0.45
P8c	a 2.039 12	EA2	1220	156	1.1075	0.16
P6b	a 2.546 97	EA1	1664	189	0.588	0.17
P22b	a 2.064 49	EA4	3553	236	1.3039	1.25
P123a	b 2.259 27	EA13	12 762	288	2.1714	0.40
P23b	a 1.924 02	EA5	1052	408	0.4211	0.14
P82b	a 1.980 55	EA11	2979	448	1.4410	0.58
P95c	b 3.145 71	EAV28	1825	476	2.2246	0.90
P5b	a 2.123 06	EAV18	2767	522	0.5075	0.28
P43b	a 2.066 23	EAV25	13 588	525	0.4292	0.32
P121b	a 2.288 20	EAV29	347	538	2.1815	1.32
P8a	b 2.046 02	EAV19	1638	539	1.1071	0.77
P22b	c 2.059 97	EAV22	6778	679	0.5368	0.16
P77b	a 2.039 22	EAV27	-249	777	1.3587	1.96
P141a	b 4.115 57	EAV30	3001	845	2.0399	2.85
P1b	a 1.867 30	EAV17	982	857	0.7556	0.38

(ii) *EAV coincident absorbers* (V for velocity) are like EA coincidences but with $v_{\text{EA}} < 1000$ km s^{-1} and $|\Delta z_{\text{EA}}| > 0.005$, so they are not EA.

(iii) *EA6 coincident absorbers* (the 6 denotes 600 km s^{-1}) are the subset of all EA and EAV absorbers with $0 < v_{\text{EA}} < 600$ km s^{-1} .

In Table 6 we list 16 EAV coincidences. The triple P8 includes one EA and one EAV pairing, while P26 and P22 also each give two pairings. The EAV pairings in P77 and P121 also have absorbers in the lower z_{em} QSO. There are also 16 EA6 coincidences.

5.4 Absorption in one QSO near absorption in the partner: AA

We now discuss absorber-absorber coincidences, where one absorber comes from each of a pair of QSOs. Fig. 6(d) shows the highly significant excess of absorbers in one QSO near an absorber in the partner QSO LOS. We plot the distribution of Δz_{AA} which we define as

$$\Delta z_{\text{AA}} = z_{\text{abs}1} - z_{\text{abs}2}, \quad (8)$$

where one absorber is from each QSO in a pair. We arbitrarily chose which QSO is 1 for the subtraction of the absorption redshifts and hence the signs have no physical meaning. However, the QSO

ordering in the main table is not random, and hence the Δz_{AA} distribution has a clear, unintended asymmetry. Some of the peak near the $\Delta z_{\text{AA}} = 0$ value again comes from the tendency of the two QSOs in a pair to have similar z_{em} values and the excess of absorbers with $z_{\text{abs}} \simeq z_{\text{em}}$. We see 29 absorbers in the single bin covering $-0.005 < \Delta z_{\text{AA}} < 0.005$ ($\pm 500 \text{ km s}^{-1}$ at $z = 2$).

Fig. 6(e) is like panel 6(d), but now excluding the associated systems from both QSOs. The excess remains with 17 systems in the bin covering $-0.005 < \Delta z_{\text{AA}} < 0.005$. The Poisson probability of ≥ 17 absorber pairs is 0.0006 when we expect 6.73 from a linear fit to $\Delta z_{\text{AA}} > 0.005$ in Fig. 6(e). The 17 pairings are a factor of $17/6.727 = 2.5$ above the expected number of chance pairings.

We now make three definitions.

(i) *AA* (absorption–absorption) *coincident systems* have a partner in the paired QSO with $-0.005 < \Delta z_{\text{AA}} < 0.005$, or approximately 500 km s^{-1} or a Hubble flow distance of 2.5 Mpc at $z = 2$. They exclude associated systems, those with $v_{\text{abs}} < 3000 \text{ km s}^{-1}$ relative to their QSOs z_{em} value.

(ii) *AAV coincident systems* (V for velocity) have

$$v_{\text{AA}} = c \frac{(1 + z_{\text{abs}1})^2 - (1 + z_{\text{abs}2})^2}{(1 + z_{\text{abs}1})^2 + (1 + z_{\text{abs}2})^2}, \quad (9)$$

less than 1000 km s^{-1} but $|\Delta z_{\text{AA}}| > 0.005$, so that they were not listed as AA. As with the AA systems, we require that both absorbers be farther than $v_{\text{abs}} = 3000 \text{ km s}^{-1}$ from their QSO.

(iii) *AAA coincident systems* (associated absorber–absorber) have $|v_{\text{AA}}| < 1000 \text{ km s}^{-1}$ and one or both absorbers at $v_{\text{abs}} < 3000 \text{ km s}^{-1}$ from their QSO.

We find 17 AA coincident absorption systems, five AAV coincidences (AAV18–22) and 12 AAA coincidences (AAA23–34). Seven pairs (P5, P6, P25, P31, P38, P42, P155) and two triples (P8, P22) contribute two or more coincidences each.

In Table 7 we list the velocity and redshift separations for these coincident system pairs. We give notes on each of the 17 AA systems in Appendix A, and we label and number them with AAxx in Table 4. For comparison with LOS measurements, only pair AA12 has a velocity separation larger than 500 km s^{-1} , which is somewhat less than the correlation length seen in individual sightlines for strong C IV and Mg II absorption systems (Young et al. 1982; Petitjean & Bergeron 1990; Scannapieco et al. 2006). It is easier to detect small velocity differences when we compare absorption systems in two, rather than one spectrum.

Fig. 7(d) shows the absolute values of v_{AA} including associated systems. When we fit a straight line plus a Gaussian with a mean of zero we find the likelihood of the data is maximum when the $\sigma = 85 \text{ km s}^{-1}$, showing that the two z_{abs} values are very similar. There are 17 paired absorbers in the bin from 0 to 200 km s^{-1} .

Fig. 7(e) shows the absolute values of v_{AA} values, excluding all associated systems. There are now 13 pairs in the first bin covering $0 < v < 200 \text{ km s}^{-1}$. A straight line fit to 200 – 20000 km s^{-1} gives $y = -0.0075x + 2.237$ pairs per 200 km s^{-1} bin. The probability of seeing 13 or more, when we expect 2.237, is 7.2×10^{-7} .

6 REST-FRAME EQUIVALENT WIDTHS AND IONS SEEN IN THE COINCIDENT SYSTEMS

In this section we see that both the AA and the EA coincident systems are unremarkable spectroscopically. Rather they seem typical of all systems that we see.

In Fig. 9 we show the cumulative distribution of the W_{rest} values of the main ions of the non-BAL absorption systems listed in Table 4.

Table 7. The 34 absorber–absorber coincidence separations in order of velocity difference v_{AA} . In all cases one absorber is from each of a pair of QSOs. The two letters after the pair number in the first column identify the two QSOs containing the absorbers. The first letter (e.g. P3b) refers to the $v_{\text{E}1}$ value in the third column, while the second letter refers to the $v_{\text{E}2}$ value. Velocities are in km s^{-1} , and the redshift difference is in units of 10^{-5} . At $z = 2$, $\Delta z_{\text{AA}} = 10^{-5}$ corresponds to $v_{\text{AA}} \simeq c\Delta z_{\text{AA}}/(1+z) = 1 \text{ km s}^{-1}$. The last column shows the separation between the sightlines at the redshift of the absorbers in proper Mpc.

QSO ^a pair	Label	$v_{\text{E}1}$	$v_{\text{E}2}$	Δz_{AA} (10^{-5})	v_{AA}	Separation (Mpc)
P3ba	AA1	117 487	116 978	3.0	5	0.096
P7ba	AA4	20 540	5134	9.0	9	0.544
P38ab	AA10	69 516	55 276	20	25	0.187
P31ba	AA9	70 581	61 263	26	32	0.858
P22cb	AAA30	6778	637	40	41	1.310
P31ba	AA8	119 877	111 525	36	53	0.815
P36ba	AAA32	32 575	180	66	67	0.343
P155ba	AA17	5067	3874	90	68	0.108
P25ba	AA6	65 840	67 137	54	70	0.126
P70ab	AA15	17 915	31 648	72	76	1.560
P155ba	AA16	27 184	25 986	102	84	0.111
P38ab	AA11	67 866	53 511	88	108	0.187
P5ab	AAA24	2767	650	133	128	0.507
P5ab	AA2	45 633	43 308	119	132	0.516
P44ab	AA14	77 597	80 008	100	140	0.382
P42ab	AA13	40 309	67 426	147	179	0.228
P83ba	AAA33	8065	1112	90	198	1.148
P25ba	AA7	50 791	52 414	192	238	0.128
P147ba	AAA34	1191	1937	316	283	0.993
P6ab	AAA25	1664	502	370	313	0.588
P22ab	AAA31	3553	637	410	402	1.310
P6ab	AA3	202 929	201 884	231	442	0.468
P22ac	AA5	3553	6778	452	443	1.310
P22bc	AAA28	1146	6778	477	467	1.310
P125ab	AAV22	38 663	39 805	568	558	0.831
P63ab	AAV21	25 662	35 635	528	597	1.098
P42ab	AA12	79 617	104 593	445	621	0.222
P8ab	AAA27	1219	1638	690	680	1.836
P8ac	AAA26	1220	941	790	785	1.836
P5ab	AAV18	11 358	8325	802	792	0.510
P22ba	AAV19	38 118	40 524	784	870	1.326
P22ab	AAA29	3553	1146	928	910	1.310
P1ab	AAA23	982	1792	893	936	0.756
P31ba	AAV20	69 650	61 263	775	953	0.858

^aIn order of velocity separation.

We detected a wide range of W_{rest} values from 0.1 to 2.8 \AA , with a mean near 0.74 \AA . We show separately the W_{rest} distribution for the 16 EA coincident absorbers.

The EA systems tend to have smaller W_{rest} values than the sample as a whole. There is a 6 per cent probability of a maximum difference larger than the $D = 0.3221$ at $W_{\text{rest}} = 0.585 \text{ \AA}$. We expect the EA coincident absorbers to have relatively small W_{rest} values, since we can see smaller W_{rest} values in emission lines and towards the red end of the spectra where the S/N is the highest.

In Fig. 10 we compare the W_{rest} values of the AA systems with the sample from which they were selected, the distribution of most absorbers. Like the EA absorbers, the AA coincident absorbers also include a larger fraction of smaller than average W_{rest} values. There is a ~ 17 per cent probability of a larger maximum difference between the two distributions of $D = 0.1875$ near $W_{\text{rest}} = 0.385 \text{ \AA}$.

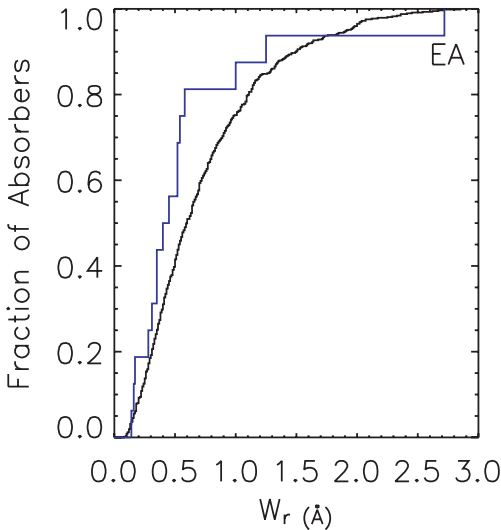


Figure 9. Cumulative distribution of the rest-frame equivalent width of 577 of the non-BAL absorption lines from Table 4, excluding the 16 EA coincidences but including associated systems (smoother black line). We show separately the W_{rest} values of the 16 EA coincidences (stepped blue line).

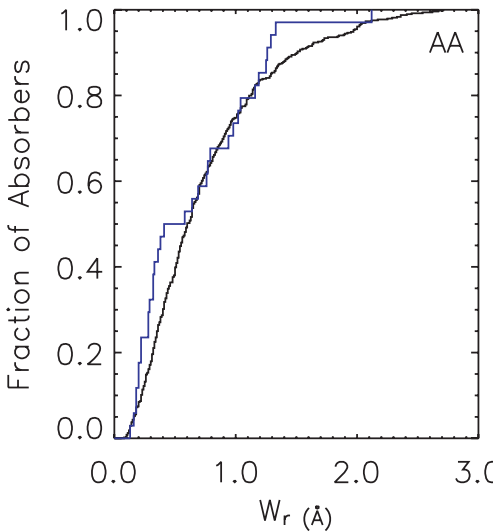


Figure 10. Cumulative distribution of the rest-frame equivalent widths of both absorbers in each of the 17 AA systems (stepped blue line) and the sample from which they were drawn (smoother black line). We use the W_{rest} values from Table 4 of the main ions in the 487 non-BAL absorption systems, excluding associated systems and excluding the 34 absorption systems from the 17 paired AA coincidences. This figure differs from Fig. 9 in that associated absorbers are now removed and the samples are divided by whether an absorber is an AA rather than EA coincidence. Most of the absorbers have W_{rest} values that indicate an origin in galaxy haloes and not in the lower density IGM.

In Table 5 we list the frequencies of ions in the EA and AA systems. We see nothing unusual about the AA coincidences. Most AA coincidences show the same ions in both systems. In only two cases (AA5, AA15) do coincident systems have no ions in common. The 17 AA coincidences show C IV 14 times and Mg II seven times, and nine of the AA systems show other ions, most often Fe II, but also Mg I, Si III, Si IV, N V, Al II and Al III.

The EA systems essentially all have C IV. We see C IV in 14 of the 16 EA systems and we expect that the remaining two also have C IV (EA8 in P36b $z_{\text{abs}} = 1.96688$ shows Si III, Si II, Al II, Al III and EA9 in P38a at $z_{\text{abs}} = 1.91658$ shows Al II, Al III) but we do not have spectra of the relevant wavelengths. The EA systems do not show Mg II or other lines with large rest-frame wavelengths because the z_{em} values are too high for these lines to be in our spectra.

7 SPATIAL DISTRIBUTION OF ABSORBERS AROUND ABSORBERS

We now give a more detailed discussion of the absorber–absorber correlation in both redshift and impact parameter in the plane of the sky. We will see that the absorbers show compact clustering on scales < 1.5 Mpc with little elongation along the redshift direction. This means that the peculiar velocities are low, more like blue than red galaxies, and much less than the velocities that Adelberger et al. (2005a) see in the C IV and H I absorption towards the intense star-forming regions of Lyman break galaxies (LBGs).

7.1 Absorption redshift errors

We are especially interested in the errors on the absorption system z_{abs} values that happen to be close to another z_{abs} or z_{em} value. For each system listed in Table 7 we made optimized fits to the main absorption lines. We list the results in Table 8. For about 40 per cent of these systems we have two or more ions per system. In those cases

Table 8. Redshift and velocity errors for 28 AA, AAV or AAA systems in order of pair number. We list only the ions we use to obtain the mean redshift in column 2 and the standard deviation of the two z_{abs} values in column 3. In column 4 we have converted the standard deviation of the z_{abs} values into velocity. The $\sigma(z)$ is in units of 10^{-5} . Velocities are in km s^{-1} .

QSO	z_{abs} mean	$\sigma(z)$ (10^{-5})	$\sigma(v_{\text{AA}})$ (km s^{-1})	Ions
P1a	1.86730	13	14	C IV N V
P1b	1.85837	26	27	C IV Si IV
P3a	0.96770	1.4	2.1	Mg II Fe II
P3b	0.96767	1.4	2.1	Mg II Fe II
P5a	2.03513	20	20	C IV C II
P5a	2.12306	7.2	6.9	C IV N V
P5b	2.04286	75	74	C IV Si III
P5b	2.12173	18	18	C IV Si IV
P6a	2.54697	17	14	C IV N V
P7a	2.13685	52	49	C IV Al II
P22a	2.06449	23	22	C IV Si IV
P22a	1.70703	6.0	6.6	C IV Si IV
P22a	1.69908	26	29	C IV Si IV
P22c	2.05997	44	42	N V Si III
P25a	1.30321	27	35	C IV Si IV
P25b	1.42593	52	65	C IV Mg II
P31a	1.02822	4.7	6.9	Mg II Fe II
P36a	1.96622	16	16	N V Si III
P36b	1.96688	23	24	Al II Si III
P42a	1.14819	6.2	8.6	Mg II Fe II
P44a	1.14351	10	14	Mg II Fe II
P70a	1.83710	41	43	Mg II Fe II
P147b	2.35187	6.0	5.3	C IV Si IV
P153b	2.51780	23	19	C IV Si IV
P155a	2.66316	59	48	C IV Si IV
P155a	2.94423	7.0	5.3	C IV Si IV
P155b	2.66216	23	19	C IV Si IV
P155b	2.94333	4.7	3.6	C IV Si IV

we calculate $\sigma(z)$, the standard deviation of the z that we measured for each ion. The mean $\sigma(z)$ is $23 \pm 4 \text{ km s}^{-1}$. We believe that this is representative of the internal errors on the z_{abs} values for systems showing one ion. For systems with two ions, we might attain errors smaller by a factor of up to $1/\sqrt{2}$. For approximately 10 per cent of the systems the lines are blended in ways that make it hard to find a unique centre, and errors will be several times larger.

When we compare to a z_{abs} value measured in the partner QSO we need to also account for systematic errors in the wavelength scales. We typically see the same ions in both spectra, and hence we are measuring the z_{abs} values at the same observed wavelengths. When these measurements are done with the same instrument and grating these external errors should be similar and hence they will have little effect on relative velocities. Otherwise the external errors may be some fraction of a pixel. We shall assume that our errors for a typical z_{abs} value are 23 km s^{-1} , noting that they will be several times larger in some cases, as seen from the large standard deviation of 19 km s^{-1} of the $\sigma(z)$ values in Table 8.

7.2 Impact parameters of AA coincidences

In Fig. 11 we see a highly significant tendency for the AA coincidences to be at unusually small separations. The probability of exceeding the observed maximum difference of $D = 0.57497$ at 0.5435 to 0.5436 Mpc is $\ll 0.5$ per cent (critical value $D = 0.381$). Of the 17 AA pairs, six are at < 0.2 , and 12 at < 0.6 Mpc, where as the mean separation of all systems from the other sightline is 1.3 Mpc. This is also seen comparing the histograms in Fig. 12.

The probability of finding an AA coincidence declines rapidly with increasing impact parameter. We see $n = 1$ coincidence from $m = 2$ systems ($n/m = 50$ per cent) in sightlines separated by < 100 kpc, six coincidences in 28 sightlines (21 per cent) at 100–200 kpc, three in 39 systems (8 per cent) at 200–400 kpc, five in 180 (3 per cent) at 0.4–1 Mpc and two in 249 (0.8 per cent) at

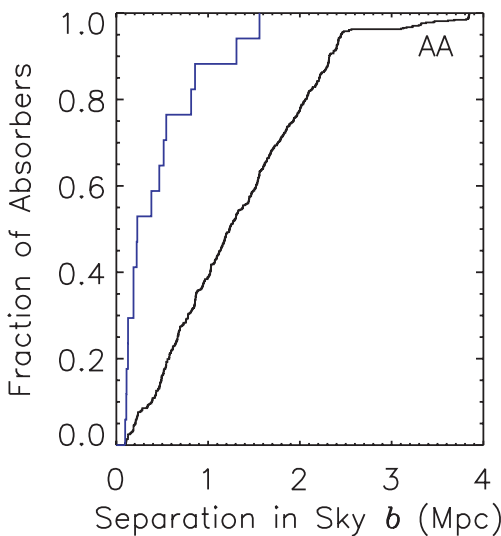


Figure 11. The cumulative distribution of the distances b (proper Mpc) between LOS measured in the plane of the sky. We show separately the impact parameter between the 17 AA coincidences (pale blue, stepped line) and the sample of 643 systems (black, smooth line) from which the AA subsample were drawn, including all absorption systems, and coincidences, but excluding cases where $z_{\text{abs}} > 0.005 + z_{\text{em}}$ of partner QSO, and excluding associated absorption systems within 3000 km s^{-1} of the host QSO. We count each coincident pair of systems as one incidence.

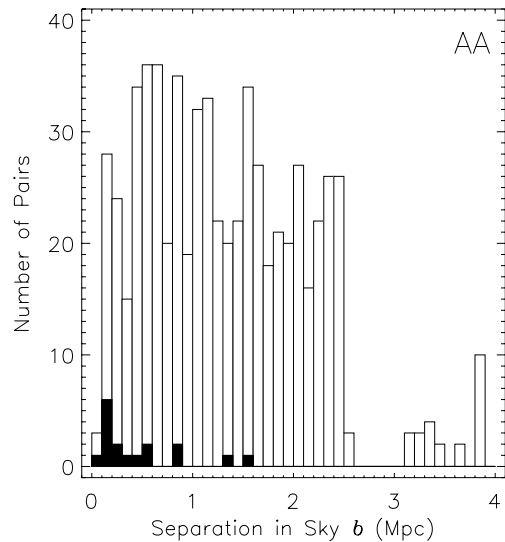


Figure 12. As Fig. 11 but as a discrete histogram showing the AA coincident absorbers (black) and the sample from which they were drawn (clear). We can explain the tendency of the paired absorbers to have small impact parameters as galaxy clustering.

1–2 Mpc. We obtain these ratios n/m by dividing the two histograms in Fig. 12. These ratios are very much lower limits since there are many cases in which we have limited or no ability to see an absorption system at the same z_{abs} in the partner QSO. High-quality spectra with complete wavelength coverage would show many more systems include those with small W_{rest} values, giving much higher probabilities.

7.3 Redshift-space distribution of AA coincidences

In Fig. 13 we see the 2D distribution of the absorber–absorber separations, in redshift space along the x -axis and in the plane of the sky along the y -axis. We place one of the two absorbers in each pairing at the origin. The y -axis is the impact parameter, and the x -axis is distance derived from Δz_{AA} assuming Hubble flow and ignoring peculiar velocities. Light rays travelling to us are horizontal lines going to the right-hand side. We average over the third dimension, which is the position angle between the QSOs in the plane of the sky.

We see the background of absorbers separated by 5–20 Mpc that is approximately uniform in density, although sparsely sampled. The clumps of points far from the origin are accidental because they are nearly all from different QSO pairs. Clustering of two or more system pairings along the LOS to a given QSO pair would appear as a horizontal grouping.

We have already seen projections of the absorber–absorber correlations into the two axes of Fig. 13. Figs 7(d, e) is the projection along the x -axis ignoring the sky separation, while Fig. 12 is the projection in the plane of the sky for coincidences with $\Delta z_{\text{AA}} < 0.005$, the AA coincidences. These two projections each showed that there is a strong and significant excess of absorbers near the origin. Absorbers are strongly clustered about other absorbers. The excess seems to extend out to about 1.5 Mpc. There are 23 absorbers within 2.5 Mpc (500 km s^{-1} at $z = 2$) of the origin, including all 17 AA coincidences that we list in Table 7. We shall show that the distribution of absorbers in the excess is consistent with the clustering of blue galaxies.

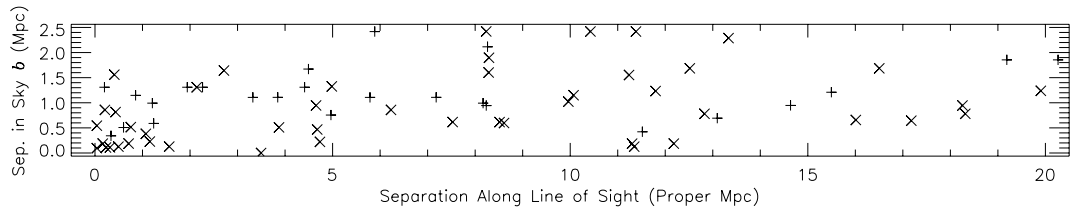


Figure 13. Detection of galaxy clustering in the absorber–absorber distribution. We show the separation in proper Mpc of pairs of absorption systems, one from each of a pair of sightlines. We plot each pairing once, with one system at the origin and the other marked by a symbol. We plot a \times for pairings that do not involve associated absorbers (including, but not limited to all the AA and AAV pairings that extend to approximately 5 Mpc). We plot a $+$ if either absorber (including but not limited to all AAA coincidences) is within 3000 km s^{-1} of its QSO. The x -axis is distance from one absorption system to that in the partner, obtained directly from the difference between the two absorption redshifts. This is the proper equivalent of the comoving π used in galaxy literature. The y -axis is the distance between the sightlines in the plane of the sky, at the redshift of the absorbers. This is the impact parameter b from equations (1) and (2), and it is the proper equivalent of the r_p in galaxy literature. We limit the vertical axis to 2.5 Mpc because we saw in Fig. 12 that we have approximately constant number of sightlines per unit b out to this distance.

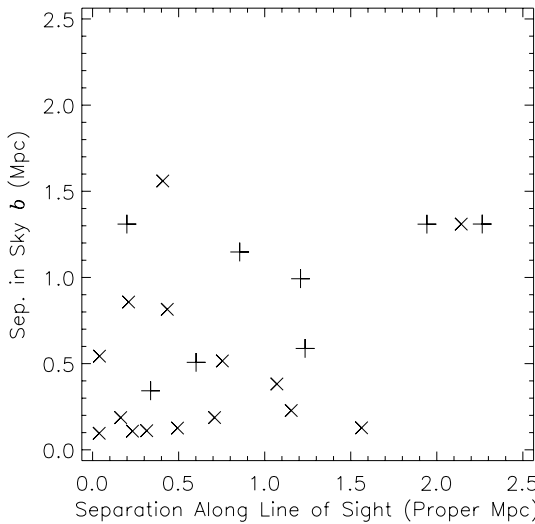


Figure 14. Enlargement of the inner 2.5 Mpc of Fig. 13.

The distribution of absorbers around absorbers can be determined from their 3D spatial correlation function. If the absorbers arise in galaxies, then the correlation function for those galaxies, modified by peculiar velocities, our sampling function and our measurement errors, will describe the distribution in Fig. 13. The level of concentration of points near the origin of the plot then depends on the correlation length, the peculiar velocities and the measurement errors.

Errors in the measurement of absorption redshifts tend to smear the x -coordinates of the plotted points. Measurement errors of 23 km s^{-1} per absorption system will contribute a 1σ dispersion of only $\sim 0.16 \text{ Mpc}$ along the x direction. We include them when we model the data but they have little effect.

Fig. 14 is an enlargement of the inner 2.5 Mpc of Fig. 13. We choose 2.5 Mpc because we know from Fig. 1 that we have approximately constant number of sightlines as a function of separation in the sky out to 2.5 Mpc. In Fig. 12 we saw that the absorbers that we found also have an approximately uniform distribution in impact parameter out to 2.5 Mpc. This is because we deliberately observed all known close pairs of QSOs but only a fraction of those at larger separations. In this way we fortuitously cancelled the increase with b^2 in the area of annuli on the sky of radius b . In the absence of

clustering we expect the absorbers to be approximately uniformly distributed along both axes of Fig. 13.

Peculiar velocities also smear points along the x -axis decreasing the density near the y -axis and producing the ‘fingers of God’ redshift-space distortion in maps of galaxy position in redshift versus sky position. Clusters of galaxies are elongated in the redshift coordinate (Davis & Peebles 1983, fig. 4) because of the large peculiar velocities. Crots et al. (1997) studied metal lines in the HIRES spectra of the triplet of QSOs, P118abc and found that the correlation between the LOS was much weaker than expected from the two-point correlation seen along many individual LOS. They proposed that the effect was caused by peculiar velocities that are large compared to the correlation length. The peculiar velocities make the LOS correlation in velocity space appear more extended than it is in proper Mpc multiplied by the Hubble constant. For our absorbers, the peculiar velocities could include random motions, while the systematic motions including infall, wind outflows and rotations. In all cases we are measuring the LOS motion of one absorber relative to a neighbour at about 1 Mpc separation. The random component of these motions are called pair-wise random velocities.

7.4 Qualitative assessment of the redshift-space distribution

In Fig. 15 we show the expected distribution of AA separations derived from the 3D two-point correlation function of LBGs from Adelberger et al. (2005b). Their correlation length measurements are larger but consistent with those from Cooke et al. (2006) who use redshifts for LBGs with similar redshifts and magnitudes, but with less sky coverage. We assume $\xi(r) = [(r + r_m)/r_0]^{-\gamma}$ with $\gamma = 1.6$ from Adelberger et al. (2005b). We set $r_m = 0.05$ proper Mpc because we are unlikely to distinguish multiple absorbers inside single haloes. We convert the Adelberger et al. (2005b) comoving correlation length measurements at $z = 1.69$ and 2.24 to proper Mpc and we linearly interpolate to $z = 2$, giving $r_0 = 2.06$ Mpc for our Hubble constant. We further reduce this by a factor of 0.6–1.24 Mpc at $z = 2$ to convert from the correlation length of their LBG galaxies to the correlation of all galaxies in the DEEP sample. We obtain the factor of $0.6 = 3.2/5.4$ from the comparison at $z \sim 1$ given in fig. 12 of Adelberger et al. (2005b). To mimic Fig. 13, we assume a constant number of sightlines per unit of impact parameter along the y -axis. Note that we have no paired QSOs separated by $y < 0.09 \text{ Mpc}$, and hence we cannot see the full amplitude of the peak near the origin. The distribution in Fig. 15 is much more concentrated near the origin than our AA coincidences in Fig. 14.

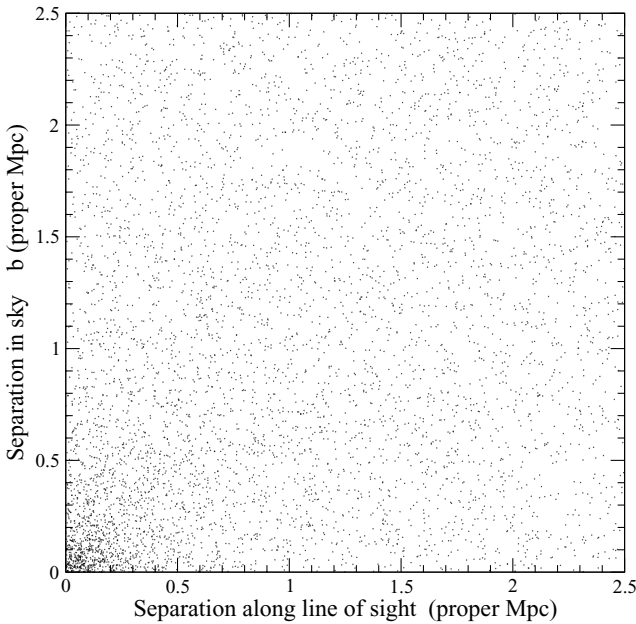


Figure 15. The expected distribution of absorbers about an absorber at the origin. We begin with a random distribution of points that sample the galaxy–galaxy two-point correlation function. We ignore peculiar velocities but we add a Gaussian random deviate to the horizontal position of each point with $\sigma(v) = 23\sqrt{2}\text{km s}^{-1}$ or ~ 0.16 Mpc to model our measurement errors.

7.5 Adding gravitational infall

Adelberger (2005, fig. 2) discusses the distortion produced by different types of peculiar velocity flows. Gravitational infall of one absorbing galaxy towards the other is a systematic effect that is correlated across the area of the plot. If the density field were spherically symmetric about the absorber at the origin we would expect radial infall towards the origin that moves most points closer to the y -axis. The amplitude of the infall will depend on the masses of the haloes of the absorbers.

In Fig. 16 we show the effect of adding systematic infalling velocities. We use infalling velocities for halo masses given in Table 9, from the lower portion of fig. 2 of Kim & Croft (2007). The haloes give infalling velocities of approximately 70 km s^{-1} out to 2.8 Mpc, declining to 20 km s^{-1} by 10 Mpc. We assume that the number of haloes is distributed as M^{-2} (Vale & Ostriker 2004) and that the absorbing area of a halo scales with the halo mass. Chen et al. (2001) find that the area out to which C IV absorption is readily seen at low z scales with the galaxy luminosity, and we assume constant M/L. Hence we assume that the absorption we see samples a halo mass distribution $\propto M^{-1}$ that we call the MidM distribution in Table 9. We expect slightly larger infalling velocities because we observe two galaxies that are absorbing, implying a local mass density above that around a typical galaxy that need not have a close neighbour.

We add radial infalling velocities directed towards the origin. These 3D velocities are a function of the radial distance (before we add simulated observational errors) from the origin alone, with no random component. The component of the velocity along our LOS decreases to zero as we rotate around the origin from the x -axis up to the y -axis, making a caustic like density peak, as shown in the upper right-hand quadrant of fig. 5 of Kaiser (1987). Since we use more than one halo mass and we have smoothed in the x direction by adding random errors in the redshifts, the caustic is less distinct

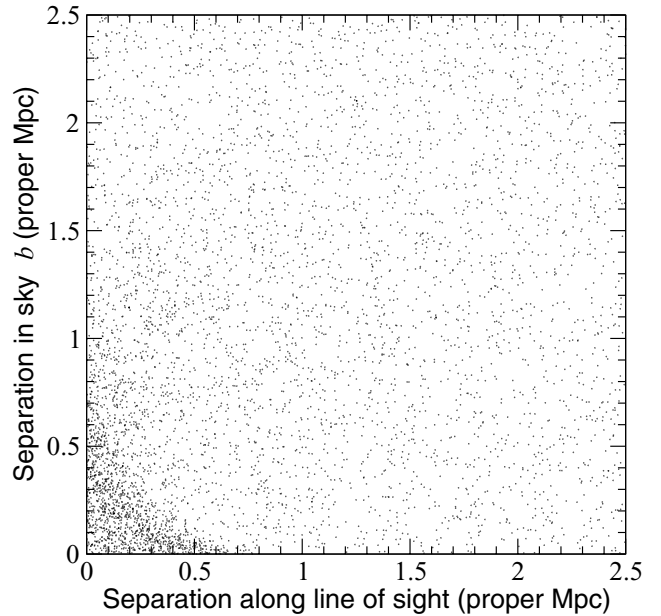


Figure 16. As Fig. 15 with observational errors and now including radial infall due to a moderate distribution of halo masses, MidM from Table 9.

Table 9. Halo masses used for infalling velocities in different models. We assume the probability of absorption in a halo of mass M is $\propto M^{-\beta}$. We list the percentage of haloes of each mass on the top row in solar units.

Model	β	5.1×10^9	1.6×10^{11}	9.1×10^{11}
LowM	2	96.9	3	0.1
MidM	1	75	23	2
HiM	–	0.1	3	96.9

in Fig. 16. The infall increases the density of points along both the x - and y -axes. For $y < 0.1$ Mpc the infall moves points away from the origin and along the x -axis, but we have almost no sightlines that sample these small y values. For other y values the infall moves points towards the y -axis, giving a lower density of points at $x > 0.4$ Mpc, $y < 0.5$ Mpc, and a higher density at $x < 0.2$, $0.2 < y < 0.5$ Mpc. The distribution in Fig. 16 is still more centrally concentrated than are the AA paired absorbers.

7.6 Adding pair-wise random velocities

In Fig. 17 we add random vector velocities v_{12} to model the pair-wise velocity differences of galaxies. We select the velocities from the (half-)exponential distribution

$$f(v_{12}) = \frac{1}{\sqrt{2}\sigma_{12}} \exp\left(-\frac{\sqrt{2}}{\sigma_{12}}|v_{12} - \bar{v}_{12}|\right) \quad (10)$$

from Diaferio & Geller (1996, equation 3.3) and Coil et al. (2008, equation 17), where \bar{v}_{12} is the mean infalling velocity. Since v_{12} is a vector, the integral of $f(v_{12})$ is one if we integrate from negative to positive infinity. Since we apply these random velocities to the undisturbed (x, y) coordinates, before we apply the infalling velocities or simulated measurement errors, we set the term $\bar{v}_{12} = 0$. This term is used if we fit the function to data comprising velocities that will necessarily include infall. We choose the dispersion

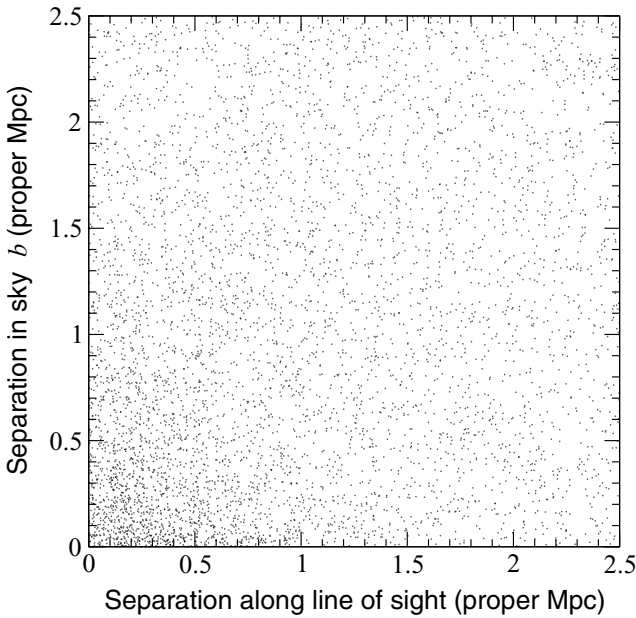


Figure 17. As Fig. 15 including observational errors and radial infall (for the MidM halo mass distribution) but now adding random pair-wise velocities from the exponential distribution of equation (10) with a $\sigma_{12} = 240 \text{ km s}^{-1}$ applied to the absorber that is not at the origin.

$\sigma_{12} = 240 \text{ km s}^{-1}$ to represent the random pair-wise velocity differences. The points are smeared along the x -axis giving the usual redshift distortion that makes the ‘finger of God’ effect that is most readily seen in dense groups and clusters where the peculiar velocities are large. Now we see a tendency of the points to be more extended along the x -axis, but it is unclear if this provides a better match to our data.

7.7 Estimation of the pair-wise velocity dispersion

Is the distribution of absorber–absorber separation in Fig. 14 consistent with absorption arising in ordinary galaxies with the expected galaxy–galaxy autocorrelation, infall and the pair-wise peculiar velocity distributions? Given the small size of our sample, we can only detect the absorber–absorber correlation on very small scales where the peculiar velocities are larger or comparable to the Hubble flow. Let us then assume that we know the absorber–absorber correlation length, the infalling velocities and the measurement errors, and ask what value for the pair-wise dispersion of the velocities is most consistent with the data. We understand that the pair-wise velocity distribution, the infall and the correlation length are all related to each other and to the history of the density distribution (Scoccimarro 2004; Slosar, Seljak & Tasitsiomi 2006).

We calculate the likelihood of our absorber–absorber distribution, as a function of the dispersion of the pair-wise velocities σ_{12} . We estimate the probability of each coincidence shown in Fig. 14 from the density of points on a version of Fig. 17 with many more points and recalculated for various values for σ_{12} . We calculate the probability P_s of absorption at (x, y) in the spectrum of the partner QSO.

The probability of one absorber at position x_i in an interval $0 < x < x_{\max}$ of one LOS is the product of three probabilities, $P_s = p_l p_i p_r$ where p_l is the probability of finding no absorbers in $0 < x < x_l$, p_i is the probability of finding an absorber at x_i

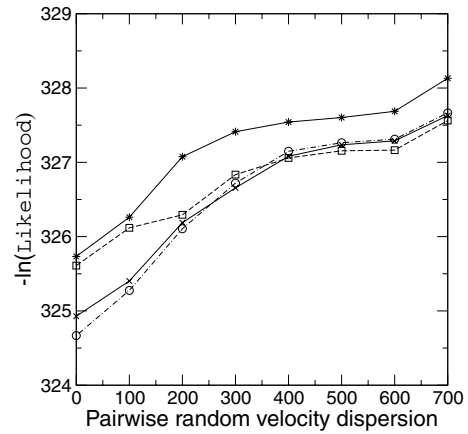


Figure 18. The maximum likelihood of the 3D distribution of absorber separations for different pair-wise random velocity dispersion (difference in velocity of nearby galaxies). The vertical axis shows the negative of the natural log likelihood of the absorber–absorber data, both coincidences and lack of coincidences. The horizontal axis shows the random pair-wise velocity dispersion σ_{12} , the parameter in the usual exponential distribution. Reading down from the top at $\sigma_{12} < 200 \text{ km s}^{-1}$, the stars show a model with no systematic infall, and the other curves are the infall for high, medium (crosses) and low (circles) halo masses.

and p_r is the probability of finding no absorbers at $x_r < x < x_{\max}$. We have no information on possible extra absorbers in the interval $x_l < x_i < x_r \sim 0.85 \text{ Mpc}$, because we can see a maximum of one absorber per FWHM of the spectra. From the Poisson distribution, the probability of no absorbers is $p = e^{-\mu}$ where μ is the expected number. We have

$$\mu_l = w_i \int_0^{x_l} p(x, y) dx \quad \text{and} \quad \mu_r = w_i \int_{x_r}^{x_{\max}} p(x, y) dx, \quad (11)$$

where $p(x, y)$ is probability of an absorber at (x, y) given by the density of points and w_i is a weighting factor that accounts for the sensitivity of the spectrum to an absorption system. Similarly, the probability of the absorber at x_i is $p_i = w_i p(x_i, y)$, and hence the probability for sightline s is

$$P_s = e^{-\mu_l} w_i p(x_i, y) e^{-\mu_r}. \quad (12)$$

The weighting w_i is the fraction of all W_{rest} values that are larger than the W_{pm} value in Table 4. If we do not list a value for either W_{rest} or W_{pm} we assume $w = 0.2$ corresponding to $W_{\text{pm}} = 1.5 \text{ \AA}$ in Fig. 9. If $W_{\text{pm}} = -1$, meaning that the main line could not be seen in the partner spectrum, we use $w = 0.1$.

The likelihood \mathcal{L} of the data set for a given model is the product of the probabilities for each sightline. We count each coincidence twice since the W_{pm} values for the two sightlines differ. We ignore absorbers with $z_{\text{abs}} > \Delta z_m + z_{\text{em}}$ of the partner QSO, where $\Delta z_m = (1+z)H(z)x_{\max}/c$ is the redshift equivalent of the distance x_{\max} .

In Fig. 18 we see that the likelihood of the data is maximum when the $\sigma_{12} = 0$ with a 1σ upper limit of 100 km s^{-1} and a 2σ limit of 300 km s^{-1} . The likelihood is insensitive to larger pair-wise velocity dispersions because the density of points is then nearly uniform in space. These pair-wise velocity dispersion values are very much at the lower end of the values reported for galaxies. The absorber–absorber correlation is concentrated near the origin showing that the absorbers arise in a ‘cold’ population, with low velocities relative to their neighbours.

In Fig. 18 we also show the likelihood for three other models from Table 9. We show a model with no infalling velocities, a model

where the probability of absorption in a halo is proportional to M^{-2} favouring very low-mass haloes and a model favouring high-mass haloes. To first order the models give similar infalling velocities and all are compatible with the data. In detail the data are most likely in models with low to medium halo masses, and less likely by more than 1σ in models using high-mass haloes or no infall. The trends follow because the low- and medium-mass halo models both give high density in the caustic region where we have four data points. The high-mass haloes have excessive velocities giving a slightly lower density near the origin, while the no-infall model has the highest density at the origin but a lower density in the caustic region.

Davis & Peebles (1983) estimated LOS random velocity differences locally could be represented as

$$\sigma_{12}(b) = 340 \pm 40(b/1.4 \text{ Mpc})^{0.13 \pm 0.04} (\text{km s}^{-1}), \quad (13)$$

for projected separations $14 < b < 1.4 \text{ Mpc}$. Like most authors we assume that σ_{12} values apply with no b dependence over a few Mpc. At redshifts $z \sim 0.1$ Zehavi et al. (2002) find SDSS blue galaxies give $\sigma_{12} \sim 300\text{--}450 \text{ km s}^{-1}$ while red galaxies give $\sigma_{12} \sim 650\text{--}750 \text{ km s}^{-1}$. Li et al. (2006) find $200\text{--}400 \text{ km s}^{-1}$ for blue and $600\text{--}800 \text{ km s}^{-1}$ for red SDSS galaxies. For the 2dF redshift survey Madgwick et al. (2003) find $\sigma_{12} = 416 \pm 76 \text{ km s}^{-1}$ for active star-forming galaxies and $612 \pm 92 \text{ km s}^{-1}$ for passive galaxies. We expect lower velocities at higher redshift but measured values are only slightly lower. At $z \sim 1$ Coil et al. (2008) estimate $\sigma_{12} = 240 \pm 20 \text{ km s}^{-1}$ for blue galaxies and $530 \pm 50 \text{ km s}^{-1}$ for red galaxies.

The low pair-wise velocities for the absorbers are marginally compatible with absorption in some samples of blue galaxies, and incompatible with red galaxies. This implies that the absorbers tend to avoid the rare high-density regions such as clusters of galaxies where the red galaxies gain much of their larger pair-wise velocities. We also believe that our sample is much too small to give a fair sample of all absorbers and hence we might anticipate a larger velocity dispersion in a larger sample, as is seen with galaxies.

7.8 Limits on wind outflows

We can use our upper limit on the random velocities to put a limit on wind outflow velocities. Adelberger et al. (2005a) recommended this test as one of the best ways to try to determine how far winds extend from the centres of galaxies. Our sample is well suited to this examination because our redshift errors of 23 km s^{-1} are small compared to the wind velocities of hundreds of km s^{-1} , and much smaller than the errors obtained for galaxies at $z = 2$ from their optical and UV lines.

Consider absorption in gas flowing radially out from galaxies. We assume this gas is transparent so we see either absorption with a velocity component towards us or away from us. The result is that the redshifts of the absorbers are changed by an amount given by the wind velocities. Assume pure radial outflow at velocity v_w confined to a thin spherical shell, and assume that absorption occurs on either the front or the back of the shell, but not on both sides. The mean component of the wind velocity along the LOS is then $0.5v_w$. If instead we see the same absorption from both sides then the mean velocity is zero by symmetry. The mean velocity will be less than $v_w/2$ depending on the frequency of two-sided absorption. Since we attempt to measure z_{abs} values for the velocity component with the highest optical depth, we will tend to set the z_{abs} value to one of the other side rather than the mean of both, except when they give similar or blended lines.

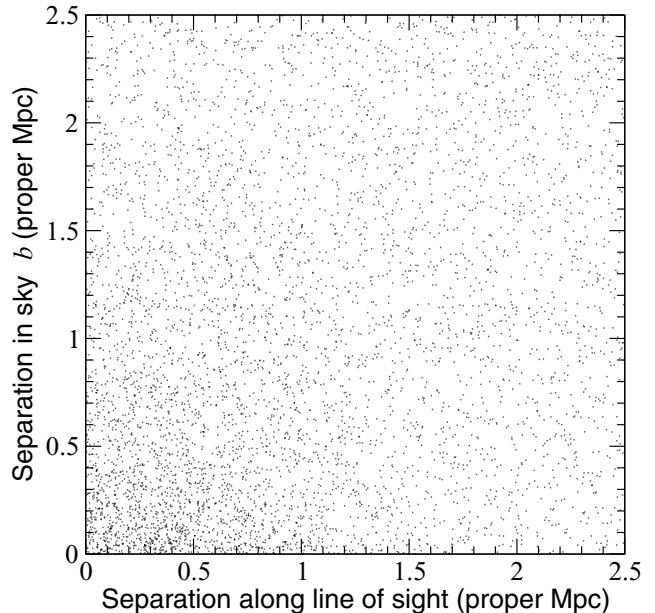


Figure 19. As Fig. 15 with observational errors, radial infall and random pair-wise velocities from the exponential distribution with $\sigma_{12} = 100 \text{ km s}^{-1}$, and now adding random peculiar velocities from a Gaussian with a $\sigma_w = 222 \text{ km s}^{-1}$ applied to the absorber that is not at the origin. This represents radial winds of $v_w = 250 \text{ km s}^{-1}$ from each galaxy, including that at the origin.

We will model the component of the wind velocity in the LOS as a Gaussian random deviate. We expect that a Gaussian is a more realistic distribution than that from a pure radial outflow with a constant velocity for all galaxies. We set the standard deviation of the Gaussian to $\sigma_w = 0.5v_w\sqrt{2}/\sqrt{2/\pi}$. The last term is the expected absolute value of a random Gaussian deviate, $\sqrt{2/\pi} = 0.7979$. The first $\sqrt{2}$ term accounts for the wind from the galaxy that makes the absorber that we place at the origin of the plot, so we do not need to also add a deviate to the origin. We choose the absorber that we place at the origin of the plot at random from each pairing, and we assume equal and uncorrelated winds for both absorbers. We then add these Gaussian deviates to each absorber on the plot, and not to the origin.

In Fig. 19 we add random velocities from a Gaussian probability distribution function with a dispersion of $\sigma_w = 222 \text{ km s}^{-1}$ to model a wind with $v_w = 250 \text{ km s}^{-1}$. Since the pair-wise random velocities can hardly be zero, we use $\sigma_{12} = 100 \text{ km s}^{-1}$. This model has much more dispersion than our data. Adelberger et al. (2005a, fig. 12) shows the positions of CIV absorbers (about 17 systems with 68 components) that they observed with <0.4 proper Mpc sky separation and $<\pm 4$ Mpc redshift difference from LBGs. They see that most absorption components have large velocity differences from their LBGs, implying several hundred km s^{-1} peculiar velocities. They suggest that these peculiar velocities may be winds, but they do not discuss normal pair-wise random peculiar velocities that can be comparable in size. The pair-wise random velocities are in part the difference between two Gaussian random deviates, giving an exponential distribution and a significant number of very large velocities. Ignoring systematic infall and measurement errors, we expect 5 per cent of galaxies to have pair-wise random velocities exceeding $3\sigma_{12}/\sqrt{2}$ or 509 km s^{-1} for the Coil et al. (2008) blue galaxies and 1124 km s^{-1} for their red galaxies. There

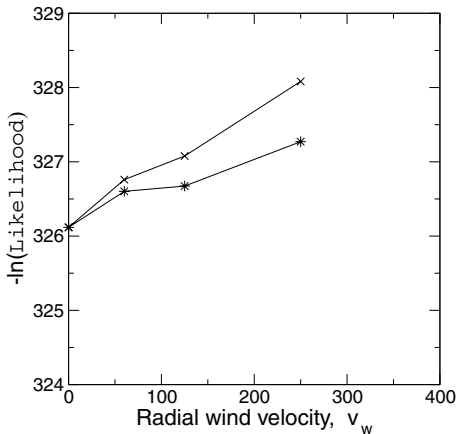


Figure 20. The negative of the natural log of the likelihood of obtaining the observed 3D distribution of metal-line absorbers as a function of the wind velocity v_w (km s^{-1}). The upper line is for a model where all absorption is in winds with the indicated velocity, while the lower line applies if the winds are restricted to 1/3 of the galaxies. The data prefer zero winds but are compatible with fast winds from <1/3 of galaxies.

is also a background of accidental coincidences extending over all velocities.

We do not see such large peculiar velocities. In Fig. 20 we see the likelihood of the absorber–absorber correlation declines significantly with increasing v_w that we use to represent the random wind velocity. The data prefer zero wind velocity with a 1σ limit of $v_w < 45 \text{ km s}^{-1}$ and a 2σ limit of 250 km s^{-1} .

The Adelberger et al. (2005a) sample differs from our in two obvious ways. We measure distances between pairs of absorbers while they measure distances from LBGs to absorbers. We take absorber redshifts from the main component visible in moderate resolution spectra while they consider all the components visible in higher resolution spectra. Hence they are exploring the low column density gas around LBGs while we are more sensitive to higher column density gas that is likely near to typical absorbing galaxies that may not be LBGs.

Absorption in gas flowing out from galaxies at a mean velocity of $v_w = 250 \text{ km s}^{-1}$ would produce much more elongation along the LOS than we see. We conclude that the absorbing gas is not in fast winds. The winds seen by Adelberger et al. (2005a) in LBG spectra are not representative of absorption systems that we see.

Adelberger et al. (2005a, section 3.1) further deduce that the LBGs in their sample can account for roughly one-third of C IV 1548 lines with $W_{\text{rest}} > 0.4 \text{ \AA}$ that is the typical W_{rest} for our AA absorbers. We model this assuming that their LBGs account for one-third of all z_{abs} that we can detect. For 1/9 of the points, where both absorbers arise in fast winds, we set $\sigma_w = 0.5v_w\sqrt{2}/\sqrt{2/\pi}$ as usual. For 4/9 of points where only one of the two absorbers arises in a wind we set $\sigma_w = 0.5v_w/\sqrt{2/\pi}$, and for the remaining 4/9, $\sigma_w = 0$. The lower curves in Fig. 20 show that the likelihood is still lower for higher wind velocities, with a 1σ limit of $<95 \text{ km s}^{-1}$ but now 250 km s^{-1} is allowed at the 2σ level.

Hence our small sample of absorber–absorber coincidences could arise in fast winds from LBGs alone extending to 40 kpc and making one third of the C IV or Mg II lines that we could detect. However, the data prefer absorption in a cold population with no extra velocity dispersion from winds, or otherwise. We are not consistent with most C IV or Mg II coming from such high-velocity winds. If most galaxies have high-velocity absorbing winds, these winds must be

confined to much less than 40 kpc. Here 40 kpc is the distance from LBGs at which Adelberger et al. (2005a) see strong C IV absorption (not necessarily from winds). Typical absorption systems are too common to be confined to smaller distances from galaxies. If all galaxies have winds that travel out greater than 40 kpc then the wind material must have low velocities where we see absorption or not have the density, metal abundance, ionization and velocity structure necessary to make metal lines that we can see.

8 SPATIAL DISTRIBUTION OF ABSORBERS AROUND QSOs

We now leave the absorber–absorber (AA) coincidences and turn to the QSO–absorber (EA) coincidences. If QSOs are in normal galaxies, we expect the EA and AA coincidences to be very similar in terms of the 3D velocity-space correlation, the infalling velocities and the pair-wise random velocities. The main differences will come from the feedback from the QSO itself, and the ~ 10 – 30 times larger errors on the z_{em} compared to z_{abs} values.

We will examine the distribution of absorbers around the QSOs. If the UV radiation from QSOs can change or destroy absorbers, then we will see an asymmetric distribution of absorbers around QSOs if the QSO UV radiation is confined to a narrow beam, or alternatively if QSOs emit isotropically but for only 0.3–10 Myr. We will not use the QSO–absorber correlation to look for signs of winds from galaxies, because the errors on the z_{em} values are too large.

8.1 Distribution of absorbers in velocity from the QSOs

We examined in Section 5.3 how absorbers are distributed around the partner QSOs as a function of the redshift difference (Fig. 6b) and velocity difference (Fig. 7b). We saw excess absorbers near the QSOs, with an a posteriori probability of 0.0003. The excess absorbers all appeared in front of the QSOs, but this asymmetry was only significant at the 1.4– 2σ level. We fit the excess of ~ 11 absorbers with a Gaussian with a mean of 300 km s^{-1} and a standard deviation of 250 km s^{-1} .

The mean velocity of the excess of absorbers around the partner QSOs is physically interesting. If the absorbers are in reality symmetrically distributed in velocity relative to the QSO systemic velocity, then the mean provides a new way to measure the difference of the z_{em} values from the systemic redshifts. This would work best in a sample of paired QSOs with a larger separation in z_{em} , which would minimize the effects of associated absorption and absorption in ejected gas. The current sample suggests that our emission redshifts are systematically too large by $\sim 300 \text{ km s}^{-1}$. An error of this size is possible, but larger than we would guess because it leads to more H I absorption behind the QSOs than we expect for the likely random errors in the z_{em} values (Kirkman et al. 2008).

Alternatively, if the QSO redshifts have small systematic errors $\ll 300 \text{ km s}^{-1}$, the mean velocity will tell us about the distribution of the absorbing gas. For example, we might see high-ionization gas that shows C IV preferentially in front of the QSOs if the QSOs are luminous for ~ 1 Myr.

The standard deviation of the LOS velocities of the excess absorbers about the QSO z_{em} values of 235 km s^{-1} , although poorly determined, is very small. This suggests that the random errors in the terms that contribute to this dispersion are also small. Let us ignore ejected gas and consider two terms that we expect when absorbers arise in galaxies near the QSO host.

First, the standard deviation of the differences of the z_{em} values from the systemic redshifts for the QSO hosts must be small

for many QSOs, including those that show the excess in the two bins.

Secondly, the LOS pair-wise random velocities of the absorbing gas relative to the QSO host galaxies must also be small. We expect pair-wise velocities to give a standard deviation of $\sigma_{12}/\sqrt{2}$ of 160–280 km s $^{-1}$ for blue galaxies and 340–500 km s $^{-1}$ for red galaxies from the references that we discussed in Sections 7.6–7.7. The small standard deviation that we see suggests that both the host galaxies for the QSOs and the absorbing galaxies are blue rather than red. This is consistent with our conclusions from our analysis of the AA correlations in Section 7.7 that the absorbers belong to the blue and not the red galaxy population. It is also consistent with Coil et al. (2007) who found that 36 QSOs from SDSS and 16 more from DEEP2 at $0.7 < z < 1.4$ are in regions with mean overdensity similar to blue and not red galaxies, implying that these QSOs are not in galaxies with the largest halo masses. The same applies to lower luminosity AGN (Wake et al. 2004; Adelberger & Steidel 2005; Constantin & Vogeley 2006).

8.2 Impact parameters of the absorbers near QSOs

In Fig. 21 we show the cumulative distribution of separations of the sightlines from the QSOs in each pairing. We use the EA6 sample, since this appears to maximize the number of excess absorbers around the QSOs, and we show separately the sample from which they were selected, including associated absorbers. We see that these EA6 coincidences are approximately a random sampling with only a slight preference to low impact parameters. There is 10 per cent chance of a random sample giving a difference between the two cumulative distributions that is larger than the maximum difference of $D = 0.2955$ that we see at 1.108–1.131 Mpc.

In Fig. 22 we show the distribution of the EA6 coincidences as a histogram. We estimate the probability of seeing an EA6 coincident absorption when a sightline passes a QSO from the ratio of the number of coincidences n to the number m of QSOs we sample

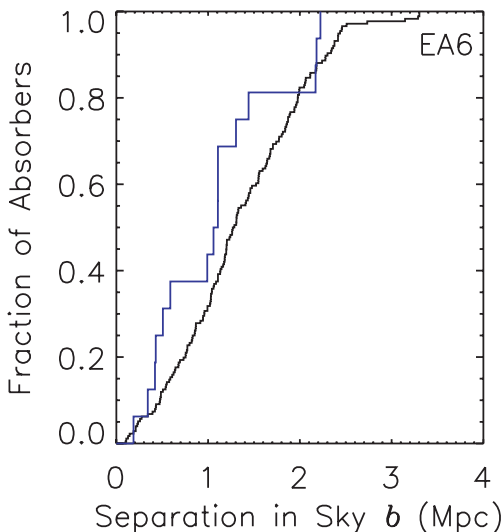


Figure 21. The cumulative distribution of the impact parameters b (proper Mpc) in the plane of the sky of the QSO–absorber coincidences. We show the 16 EA6 coincidences (fainter blue stepped line) and the sample from which they are drawn (smooth black line), the distances from all foreground QSOs to the partner sightline, plus the distances for the background to the foreground QSOs when the z_{em} difference is <0.005 and including all EA pairings.

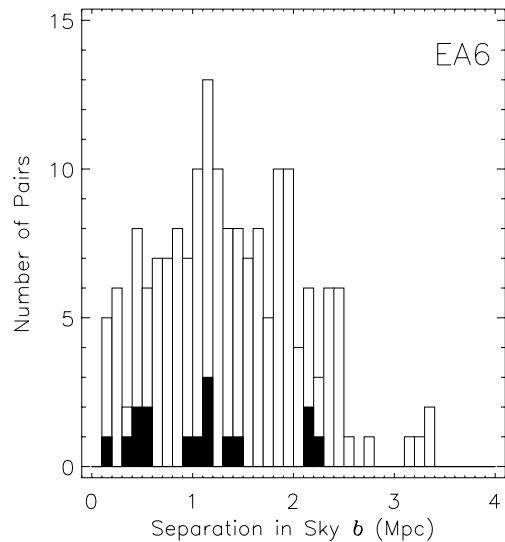


Figure 22. Same as Fig. 21 but in histogram form, showing the 16 EA6 coincidences (black) and the sample from which they are drawn (clear).

Table 10. The probability of seeing a coincidence as a function of impact parameter b in proper Mpc. The n is the number of AA or EA6 coincidences seen from a potential sample of size m . The n values include the background of random uncorrelated absorption systems, 6.73 of the 17 AA coincidences and 5.77 of the 16 EA6 systems.

b (Mpc)	AA coincidences			EA6 coincidences		
	n	m	$100n/m$ (per cent)	n	m	$100n/m$ (per cent)
0.0–0.1	1	2	50	0	0	–
0.1–0.2	6	28	21	1	5	20
0.2–0.3	2	24	8	0	6	<30
0.3–0.4	1	15	7	1	2	50
0.4–0.5	1	34	3	2	8	25
0.5–0.7	2	72	2.7	2	13	15
0.7–1.0	2	74	2.7	1	22	4
1.0–1.5	1	129	0.8	6	49	12
1.5–2.0	1	120	0.8	0	40	<5
2.0–2.5	0	117	<1.5	3	25	12
0.0–2.5	17	615	2.8	16	169	9.5

per bin. From the values in Table 10 we have $n/m = 1/5$ (20 per cent) at impact parameters of $b = 100$ –200 kpc, 3/16 (19 per cent) at 200–500 kpc, 3/35 (8 per cent) at 0.5–1 Mpc, 6/49 (12 per cent) at 1–1.5 Mpc and 3/65 (5 per cent) at 1.5–2.5 Mpc. As for the AA coincidences, these ratios are very much lower limits because there exist many weak metal lines that we do not detect. On the other hand, we know from Fig. 7(b) that only ~ 10.2 of the 16 EA6 absorbers are in excess over the background of 5.77 absorbers that accidentally have z_{abs} similar to the z_{em} values.

On scales below 100 kpc where we have no sightlines, Bowen et al. (2006) found Mg II in 4/4 sightlines at impact parameters of 26–97 kpc, while Hennawi et al. (2006a, fig. 1) saw LLS in 3/3 cases at <100 kpc. At 100–200 kpc our probability of 1/5 for EA6 coincidences is not significantly lower than the 3/8 from Hennawi et al. (2006a, fig. 1), for their LLS absorbers. The probability of seeing 0 or 1 is 0.44 for an expectation of $5 \times 3/8 = 1.875$.

In Fig. 23 we show that the impact parameters of the EA6 and AA coincidences have different distributions. The maximum difference

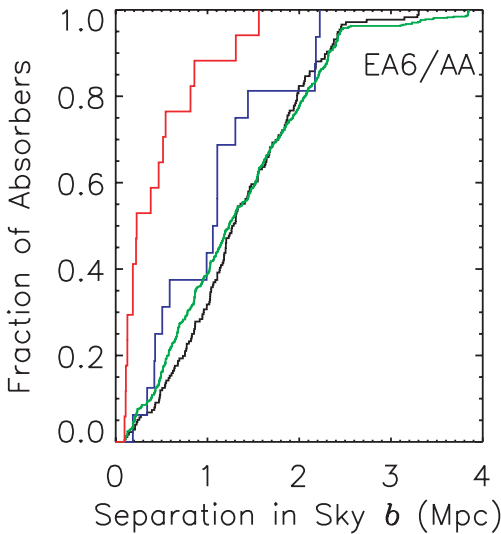


Figure 23. Combination of Figs 11 and 21. From top to bottom at 0.7 Mpc, the distributions are AA (17 in red), EA6 (16 in blue), the parent populations for AA (smooth pale green) and for EA6 (black). The EA6 and AA samples are selected from similar distributions of impact parameter, both of which are nearly uniform from 0.1 to 2.5 Mpc, appearing as straight lines in this plot.

between the EA6 and the AA cumulative distributions is $D = 0.5074$ at $0.858\text{--}0.990$ Mpc. If we ignore the relatively small difference in the two parent populations, the probability of a larger difference is ~ 1.6 per cent by the two-sample Smirnov test (Conover 1980, A21). This drops to a differences of 0.437 and a probability of ~ 4.5 per cent when we subtract the difference in the parent populations.

We have no compelling explanation for why the probability of detecting an EA6 coincidence is approximately constant from about 0.1 out to 2.5 Mpc, while the AA coincidences (Fig. 12) are strongly concentrated to small impact parameters. This difference could be an accident because the samples are small. The background contamination will tend to make the distributions uniform in impact parameter, but for both the AA and EA6 coincidences, we estimate the same proportion of background: 6.73 of the 17 AA coincidences versus 5.77 of the 16 EA6. The large z_{em} errors will cause the EA6 sample to miss some coincidences, however, when we include all EA + EAV coincidences that extend out to 1000 km s $^{-1}$, the background rises much more than the number of excess coincidences. Fig. 22 looks similar but with less concentration around the QSO. The plot is also very similar when we use EA instead of EA6. Perhaps absorbers are missing at low impact parameters because they are destroyed by the UV radiation from the QSOs, possibly by photoevaporation (Hennawi & Prochaska 2007). This hypothesis would lead us to expect to see fewer absorbers of a given type and rest-frame equivalent width near to QSOs than near to other absorbers. However, we see the opposite.

In Table 10 we see that the overall rate of seeing an absorber when we pass another absorber (AA) is 2.8 per cent compared to 9.5 per cent when we pass a QSO (EA6 or EA). If we consider only the excess absorbers, these rates drop to 1.7 per cent for AA and 6.1 per cent for EA6. We believe that we more often see excess absorption near a QSO than near another absorber because our sample is inhomogeneous. It is easier to see absorbers near to the QSOs in the high S/N in the emission lines and towards the red end of spectra. From Fig. 7(a) that shows LOS absorbers, we see a

mean of eight absorbers per 200 km s $^{-1}$ at 0–2000 km s $^{-1}$ compared to ~ 1 per 200 km s $^{-1}$ at much larger velocities. This explanation is consistent with our finding from Fig. 9 that the EA coincident systems have lower than typical W_{rest} values. This also explains why we see the excess EA coincidences in Fig. 7(b) but not in Fig. 7(c) where we removed all the associated absorbers, leaving too small a sample.

8.3 Redshift-space distribution of absorbers around QSOs

In Fig. 24 we show how the absorption systems are distributed around the QSOs in two dimensions. This Fig. 24 is like Fig. 13 but we now place QSOs and not absorbers at the origin of the plot. The x-axis is distance from the QSO to the absorber along the LOS. We obtain this from $z_{\text{em}} - z_{\text{abs}}$, giving positive values when $z_{\text{abs}} < z_{\text{em}}$. If there were no redshift errors or peculiar velocities, the points on the right-hand side of the plot would be nearer to us than the QSOs. The y-axis is the impact parameter in the plane of the sky. As we discussed for the EA values in Section 5.3, we include both foreground and background QSOs since many pairs have similar z_{em} values and z_{em} errors can be large. Since the UV flux from the QSOs is expected to be a factor of a few larger than the UV background out to about 4 Mpc for this sample of QSOs (Kirkman et al. 2008), we show an 8 Mpc range for the x-axis.

We include on the plot the absorption systems selected from table 1 of Hennawi et al. (2006a). The systems are Lyman limits and DLA lines within 1500 km s $^{-1}$ of the z_{em} values of 149 foreground QSOs at projected separations of 0.031–2.4 Mpc. We are interested in the distribution of the absorbers in velocity, and not in the absolute rate of detection, and hence we are not concerned that some of their systems might not have high H I column densities.

Errors in the z_{em} values will often be several hundred km s $^{-1}$ and hence the x-axis location of many points will have large random errors. As we discussed in Section 5.3 the narrow width of v_{EA} values for the coincident EA systems suggests that some QSOs have z_{em} errors of less than 300 km s $^{-1}$. However, we also expect larger errors for many QSOs. Hennawi et al. (2006a) guess errors of 300, 500, 1000 and 1500 km s $^{-1}$, depending on the emission lines seen, for the z_{em} values that they provide and we use.

The interpretation of Fig. 24 is complicated by the presence of a few background QSOs that are in the volume on the left-hand side of the plot, but are not shown on the plot. The spectra of these QSOs sample only part of the LOS past the foreground QSO, the part to the right-hand side of the QSOs position. We have two QSOs at 0 to -0.5 Mpc, 13 at -0.5 to -4 Mpc and nine at -4 to -8 Mpc. These QSOs are all from our sample, since we allow EA systems to come from QSOs with similar or identical z_{em} values. Hennawi et al. (2006a) did not consider QSOs within 8 Mpc of their foreground QSOs. These few QSOs have a small effect on the total sample of 313 QSOs.

We discussed in Section 7.5 the effects of systematic infalling velocities of absorbers (galaxies) around other absorbers. That discussion also applies to absorbers around QSOs, with the difference that the infalling velocities may be different, though not necessarily higher (Slosar et al. 2006), even if the QSOs reside in more massive haloes than typical galaxies. Croom et al. (2005) estimated QSO halo masses of $4.2 \pm 2.3 \times 10^{12}$ solar masses in the 2QZ sample at all redshifts. Coil et al. (2007) also found a mean mass of $\sim 3 \times 10^{12}$ at $0.7 < z < 1.4$. Less directly, Kim & Croft (2007) use the distribution of H I absorption seen in background QSOs to estimate the masses of nearby foreground QSO haloes. They find a mean mass of $\log M = 12.48_{-0.89}^{+0.53}$ ($0.4\text{--}10 \times 10^{12}$) in solar units for

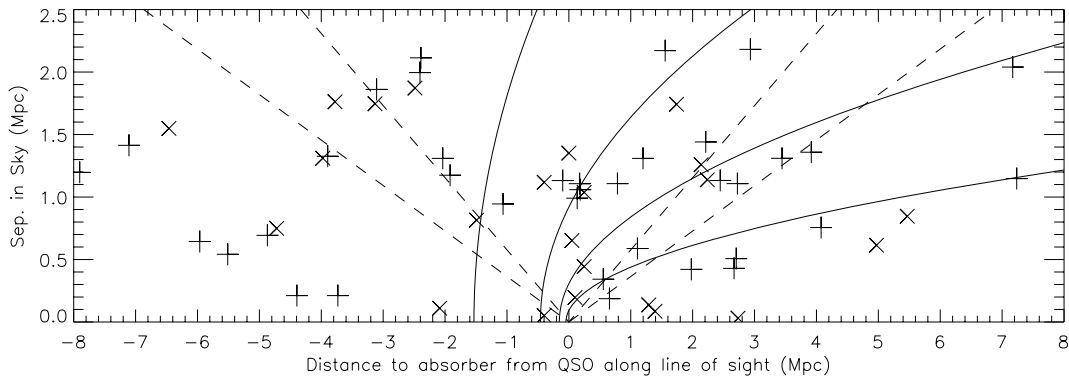


Figure 24. The distribution of absorbers near to QSOs that we place at the origin of the plot. Rays from the QSOs travelling towards us are horizontal lines extending to the right-hand side. The horizontal axis is derived from the velocity difference $v_{\text{EA}} \sim c(z_{\text{em}} - z_{\text{abs}})/(1 + z)$ which is positive for absorbers that have a smaller redshift than the emission redshift of the partner QSO. We have converted the v_{EA} values into proper Mpc using the Hubble flow alone, ignoring peculiar velocities. The vertical axis shows the proper distance between the two QSOs in the plane of the sky, coming from their angular separation. We truncate the plot at $b = 2.5$ Mpc because Fig. 22 shows that the density of impact parameters for possible EA coincidences is nearly constant up to this value, but then declines by a factor of several. We show the 36 absorbers (+symbols) that we saw around 170 QSOs (the sum of the open histograms at $b < 2.5$ Mpc in Fig. 22), and 23 absorbers (\times) towards 143 QSOs from Hennawi et al. (2006a). We do not double count six QSOs that we have in common with Hennawi et al. (2006a). We use our z_{abs} for three cases where we report the same absorber in the same QSO. Two additional z_{abs} from their table 1 are outside the area of this plot. The dashed lines show angles of 20° and 30° from the horizontal axis, half apex angles for cones containing the UV. The parabolas show the maximum distance the light travels from a QSO if that QSO switched on 0.3, 1, 3 or 10 Myr ago, in the QSO rest frame. Points below the dashed lines and to the right-hand side of the parabolas are more likely to be illuminated by the UV flux that we see from each QSO. Errors in the z_{em} values move points horizontally 2–4 or more Mpc. If the QSOs have had their current luminosities for only 10 Myr, then the volume to the left-hand side of the leftmost parabola had not yet received the UV that we see from the foreground QSO, when the light from the background QSO we see today passed through that volume.

QSOs at $z = 3$ with absolute G -band magnitude -27.5 , a factor of 20 above the mass of LBGs.

Adelberger (2004, fig. 16) shows corrections for systematic infall towards QSOs plus random peculiar velocities. These corrections are typically 0.2–0.4 Mpc at $z = 3$ for the distances out to 4 Mpc, implying (Hubble flow) velocities of 40–80 km s $^{-1}$. Systematic corrections of this size have little effect on our plots. As we mentioned in Section 7.5, Kim & Croft (2007, fig. 2) use simulations to estimate how the mean radial infalling velocities increase with the mass of the halo. These infalling velocities are also modest, except for their most massive halo with 5.1×10^{12} solar masses that gave peak infalling velocities of 270 km s $^{-1}$ at 1.2 Mpc.

8.4 Transverse associated absorbers are rarely seen in the LOS

When we see excess absorbers in the LOS to background QSOs near the z_{em} of foreground QSOs, we call these transverse absorbers that are associated with the foreground QSO. If the transverse absorbers are selected from a population, such as galaxies, that are found in all directions around the QSOs, then we should be able to see these same absorbers in individual QSO spectra at $z_{\text{abs}} \sim z_{\text{em}}$.

The transverse absorbers are rarely seen in the LOS to individual QSOs. For example, if 20 per cent of the 310 QSOs showed one absorber at $0 < v_{\text{abs}} < 600$ km s $^{-1}$ drawn from the population of transverse absorbers that happen to be in the LOS, then we would see 62 excess absorbers at these v_{abs} values where we see only 21 in total in Fig. 7(a), or 7 per 200 km s $^{-1}$, consistent with the mean density of 8.0 ± 0.9 absorbers per 200 km s $^{-1}$ from 0–2000 km s $^{-1}$. From the Poisson distribution, there is a 5 per cent chance of seeing 21 or less absorbers when the mean is 30.2. This gives an approximate (2σ) upper limit of $(30.2 - 24)/310$ or ~ 2 per cent of QSOs showing transverse associated absorbers in the LOS at 0–600 km s $^{-1}$. This upper limit is of low accuracy

because we do not know the distributions of the transverse and non-transverse LOS absorbers.

Bowen et al. (2006) and Hennawi & Prochaska (2007) report more transverse absorbers in the plane of the sky than equivalent absorbers seen in the LOS to individual QSOs. Indeed this is how they found the transverse absorbers, but the comparison of the absolute numbers of absorbers can be insecure. Hennawi & Prochaska (2007) are very sensitive to the minimum column density in their sample, while we did not apply any minimum W_{rest} .

We see an excess transverse absorber in ~ 6.1 per cent of cases when a sightline passes a QSO. We see excess absorbers at the same velocities in < 2 per cent of cases in the LOS to QSOs, which we can double to < 4 per cent for comparison, because the LOS does not sample the absorbers behind the QSOs. The reason why we see fewer transverse absorbers in the LOS may be related to the lack of the expected steep rise in the numbers of EA coincidences with decreasing impact parameter (Section 8.2). Since the EA absorbers are not strongly concentrated near the QSOs in impact parameter, there is no huge difference in looking directly to a QSO versus looking past the QSO with an impact parameter of ~ 1 Mpc.

8.5 Is the UV emission from QSOs beamed towards us or obscured in other directions?

A popular explanation for why we see few transverse absorbers along the LOS to individual QSOs is that the UV radiation from a QSO illuminates the LOS to us, but not the transverse directions in the plane of the sky. Absorbers in the UV radiation beam and near to the QSO are changed in some way. They might become too highly ionized to show the ions we can see, or they might be destroyed or photoevaporated (Hennawi & Prochaska 2007) so they no longer make absorption lines that we can see. We can also imagine the converse, where the QSO UV radiation enhances ions such as C IV and N V that we see. These processes will presumably depend in part on physical structure of the absorbers, such as whether they are

optically thin or thick in the Lyman continuum. The UV might be beamed, and only omitted in certain directions, including towards us, or most other directions might be obscured, e.g. by dust.

Let us put aside the z_{em} errors, peculiar velocities, and complications of paired QSOs near to each other and look for evidence that the QSO UV radiation is anisotropic. Let us assume that the UV luminosities of the QSOs have not changed for more than 17 Myr so they can illuminate all of Fig. 24. Assume that the UV from all QSOs is emitted only inside a pair of coaxial cones, one opening towards the Earth and the other away, and with their vertices at the QSO. If the QSO UV radiation destroys the transverse absorbers that we do not see in the LOS, then we expect absorbers will be less common inside the cones of UV radiation.

We show in Fig. 24 dashed lines for cone apex half-angles of $\theta = 20^\circ$ and 30° measured up from the horizontal axis, the LOS to the Earth. We see numerous absorbers between the horizontal axis and the dashed lines, and to first order the distribution of absorbers around the QSOs looks isotropic, except for the preference for velocities 0 – 600 km s^{-1} that we discussed in Section 5.3.

However, three issues persuade us that the plot is compatible with UV radiation confined to cones, leading to a lower (or higher) density of absorbers inside the cones. First, the UV radiation may destroy absorbers out to at most a few Mpc from the QSO at the origin. The precise distance will depend on the absorber gas density and structure, the QSO luminosity, the length of time the QSOs has its current luminosity (Kirkman et al. 2008), the ions we see and the sensitivity of the spectrum. Secondly, z_{em} errors will more often move points into the cone than outside it when the impact parameter is small. This can account for the absorbers near the x -axis. Thirdly, LOS to the Earth can be anywhere in the UV illuminated cone, including at the edge of the cone. The probability of looking into a cone at some angle to the cone axis is proportional to that angle. If an LOS is along one edge of the cone, then we expect absorbers below the dashed line down to the horizontal axis, on both sides of the origin, because the figure ignores the position angle from the QSO to the absorber in the sky.

In Fig. 25 we show the distribution of absorbers that we expect around the QSOs. This figure is intended to mimic the data in Fig. 24. It was made using the methods described for the absorber–absorber correlations shown in Figs 15–17. The top panel shows the distribution expected from clustering, infall and random pair-wise velocities alone. For the clustering, we use $\xi(r) = [(r + r_m)/r_0]^{-\gamma}$ with $\gamma = 1.6$, $r_m = 0.05$ proper Mpc, and $r_0 = 1.2$ proper Mpc (Adelberger et al. 2005b). For the infall, we use the velocities from the Kim & Croft (2007, fig. 2) for a halo of mass 5.1×10^{12} solar masses, and we assume the curve flattens at distances smaller than they show, reaching a constant value of 272 km s^{-1} . For the pair-wise random velocities we use $\sigma_{12} = 400 \text{ km s}^{-1}$. We could improve the plot using infall for a range of QSO masses and a range of σ_{12} values. There is clearly much more concentration near the QSO at the origin of the plot than in the data in Fig. 24.

In the second to top panel we have removed points from a cone with a half apex angle of 20° and an axis pointing directly towards us, which is unrealistic. We remove the points after we add clustering, and before we add infall and pair-wise velocities, since the points are removed in real space, not velocity space. The infall is systematic and distorts the cone edges, but the pair-wise velocities are random and move points, especially those near the QSO, into the cone, making the cone hard to see even with about 20 000 points. A cone with a wider opening angle would be easier to see, as would a cone that extended farther from the QSO, in units of the pair-wise velocity dispersion.

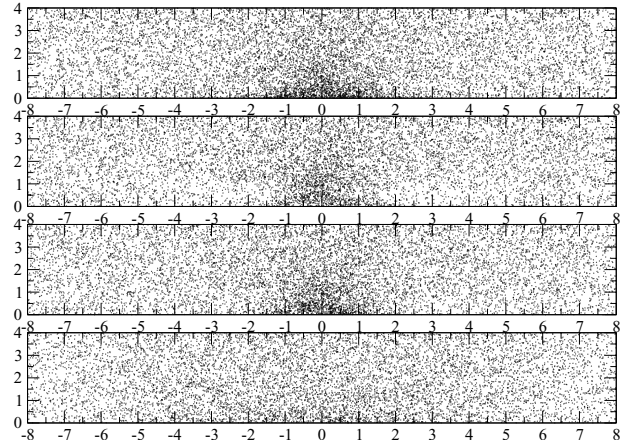


Figure 25. Simulation of the distribution of absorbers near to QSOs that we place at the origin of each panel. Axes and points as in Fig. 24 but here with 4 Mpc rather than 2.5 in the y direction. Top, showing clustering, infall and random pair-wise velocities. Second top, as top, now removing all points from a cone with half-apex angle of 20° . The cone axis is pointing directly towards us. We are off to the right-hand side of the plots, along the horizontal axis. We remove points out to a distance of c Mpc, where c is a normal random deviate with a mean of 4 Mpc and $\sigma = 2$ Mpc. Second to bottom, as above but now the cone axis is tipped to the LOS to us, with probability proportional to the angle to us. Bottom, as above and now also including the QSO emission redshift errors.

In the second to bottom panel we allow the cone axis to be tipped relative to the LOS to us with probability proportional to the angle. You can still see a lower density of points near $x = \pm 0.5$, $y = 3$ Mpc, but this would be missed if we did not know what to expect.

In the bottom panel we add normally distributed errors for the difference between the emission and absorption redshifts, comprising 35 per cent with $\sigma = 2$ Mpc, 35 per cent with $\sigma = 4$ Mpc and 30 per cent with $\sigma = 8$ Mpc. Since the absorption redshift errors are about 0.1 Mpc, these values are completely dominated by the poorly known errors in the emission redshifts. This plot should be the best representation of the data, and shows that we will not be able to see the emptied cone. Three random effects, the orientations, how the QSOs might change individual absorbers at a specified distance, and especially the random pair-wise velocities all combine to hide all but the most gross effects.

We could make the data more like the second to bottom panel if we had accurate systemic redshifts for the QSOs that have nearby absorbers. However, there is no obvious way to know the beam orientation to better than 20° . Radio core halo or jet morphology might help give the position angle on the sky, but only ~ 10 per cent of our QSOs will be radio-loud. A much better way to study the distribution of the UV around QSOs is to use higher resolution spectra to explore the ionization of individual systems. In this way Goncalves, Steidel & Pettini (2008) see evidence for enhanced UV in the transverse direction from two bright QSOs.

8.6 QSO episodic lifetimes

The second popular explanation for why we see few transverse absorbers along the LOS to individual QSOs is that the QSOs have a short episodic lifetime of ~ 1 Myr. By episodic lifetime we mean how long, measured in the QSO rest frame, did a QSO have a UV luminosity similar to that seen today. We will explore a model in

which QSOs are UV luminous in various episodes separated by longer intervals of negligible UV emission.

If the QSOs emit isotropically but were less luminous in the past, then we expect a lack of absorbers confined to regions illuminated while the QSOs are luminous. These regions are bounded by parabolic surfaces with the QSO at the focus and the apex of the parabola farther away from us by half the distance that light can travel in the QSO life. All rays leaving a QSO at a given time and reflecting on a parabola reach us at the same time. Adelberger (2004, fig. 3) and Visbal & Croft (2008, fig. 1) show these parabolic surfaces that have the equation

$$y = \sqrt{2d(x + d/2)}, \quad (14)$$

where x is the horizontal axis of our plots, along the LOS to Earth and y is the impact parameter in the plane of the sky. With x and y in proper Mpc, the d in the equation is the delay measured in Mpc which corresponds to a time delay t in Myr of $t(\text{Myr}) = 3.2617d$ (Mpc). We show delays of $t = 0.3, 1, 3$ and 10 Myr, corresponding to $d = 0.09198, 0.3066, 0.9198$ and 3.066 Mpc. All points in space that are to the right-hand side of the parabola for a given lifetime will have been exposed to the QSO flux.

A key point is that these parabolas are strongly asymmetric about the QSO while the bicone beaming hypothesis gives a symmetric pattern. We should then be able to distinguish beaming from QSO life time by examining the distribution of absorbers about the QSOs. We again assume that the QSOs UV is only able to destroy absorbers out to some distance, and we ignore the infalling velocities that are probably smaller than the errors on most z_{em} values.

There are many points to the right-hand side of the parabolas where we would expect few if the QSOs have short episodic lives and their UV radiation destroys all nearby absorbers. We expect some absorbers inside the parabolas for two of the three reasons already mentioned for the beamed bicone model. The QSO UV radiation will only destroy absorbers out to at most a few Mpc, depending on the QSO and absorber, and the z_{em} errors will move points horizontally. Given the difficulty we saw in detecting the 20° evacuated cones, it seems hard to detect life times of under 1 Myr because they do not remove enough points. We could interpret the slight tendency that we saw in Section 5.3 for absorbers to lie in front of QSOs as evidence that the QSO UV radiation enhances, rather than reduces, the number of C IV absorbers near to the QSOs. From Fig. 24 an episodic lifetime of ~ 3 Myr would then explain why we do not see an equivalent excess of C IV behind the QSOs.

Many other lines of evidence relate to QSO UV life times. Croom et al. (2005) estimate QSO active life times of 4×10^6 – 6×10^8 yr at $z \sim 2$. Goncalves et al. (2008) see direct evidence for life times of greater than 25 Myr and of $16 < t < 33$ Myr for two luminous QSOs. Adelberger & Steidel (2005) argue that the lack of dependence of the QSO–galaxy correlation length on QSO luminosity implies that lower luminosity AGN live longer.

9 BAL SYSTEMS

So far we have ignored the BAL systems. We now present two plots that explore potential coincidences in BAL systems. We do not expect to see excess coincidences over the random distributions because the BAL winds are believed to extend much less than an Mpc from the QSOs.

In the top of Fig. 26 we show the distribution of BAL system redshifts relative to the redshifts of the partner QSO. We see that about 50 per cent of the differences are confined to $-0.05 < \Delta z_{\text{EA}} < 0.1$. In comparison, Fig. 6(b), with the same bin size,

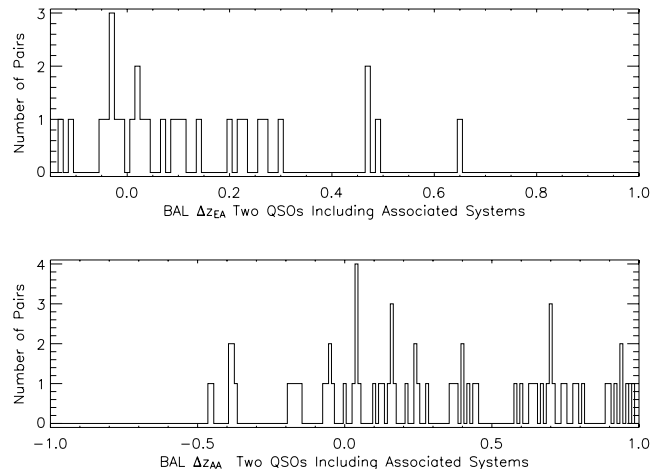


Figure 26. The Δz_{AA} and Δz_{EA} distributions for the 34 BAL systems, with Δz bins of 0.01. The BAL systems distribution is unremarkable.

showed that the non-BAL absorbers show an excess that is more confined around $\Delta z_{\text{EA}} = 0$. The Δz_{EA} values for the BAL systems may have a wider dispersion because we will have large z_{em} errors when the absorption is in the emission-line peak. The BAL systems also have a different v_{abs} distribution from the non-BAL systems that will be convolved with the distribution of the differences in the z_{em} values of the paired QSOs. In addition, we biased our sample to disfavour QSOs with strong BAL systems that would place Ly α absorption at 1070–1270 Å rest in the partner QSO spectrum. To make progress we would prefer an unbiased sample in which the background QSO z_{em} was much larger than the foreground value.

In the lower panel of Fig. 26 we look for coincidences between BAL systems in one sightline with BAL systems in the other sightline. There is no excess near to $\Delta z_{\text{AA}} \sim 0$ except for the four pairings at $\Delta z_{\text{AA}} \sim 0.03$ that may come from the similarity of the z_{em} values of the paired QSOs.

10 CONCLUSIONS

We presented and discussed the first large sample of metal-line absorption systems seen in pairs of QSOs. In the plane of the sky, the QSO pairs are separated by 0.1–2.5 Mpc at $0.2 < z < 4$ and typically 1 Mpc at $z = 2$. We found 690 absorption systems, most showing C IV or Mg II (Tables 4 and 5) in the spectra of 310 QSOs in 170 pairings. We used medium-resolution spectra (Table 3) and saw lines with typical rest-frame equivalent widths $W_{\text{rest}} = 0.5$ Å, with a 90 per cent range of 0.2–1.3 Å. Lines of this strength usually arise in galaxy haloes. We summarize and discuss this work under several headings.

10.1 LOS associated absorption

The top panel of Fig. 7 shows the strong tendency of the LOS absorbers to have $z_{\text{abs}} \simeq z_{\text{em}}$. We see an nearly constant high density of absorbers from 0 – 2000 km s $^{-1}$, and a smaller excess that extends to approximately 9000 km s $^{-1}$. The excess with $z_{\text{abs}} \simeq z_{\text{em}}$ is caused by galaxies near the QSOs and intrinsic absorbers (Wild et al. 2008, fig. 9). The excess is enhanced by the ease of finding absorption near to the emission lines, and the red end of spectra, where the S/N is highest.

We do not restrict our sample to lines exceeding some minimum W_{rest} value. While the distribution of our absorbers in $z_{\text{abs}} - z_{\text{em}}$ is

similar to that shown by Weymann et al. (1981), who also do not use a minimum W_{rest} , we have not examined whether the lower luminosity QSOs presented here are different from the high-luminosity QSOs analysed in the 1980s.

In Fig. 3 we saw that the paired QSOs tend to have similar z_{em} . This tendency couples with the excess of absorbers with $z_{\text{abs}} \sim z_{\text{em}}$ in both sightlines to give extra random associations with the z_{abs} and z_{em} of the partner QSOs.

10.2 AA absorber-absorber clustering

The correlation of absorbers with other absorbers describes the distribution of metals around galaxies and the clustering of those galaxies. Our absorber redshift errors of $\sim 23 \text{ km s}^{-1}$ (Table 8) are about 10 times smaller than the typical errors for galaxies at these redshifts. This allows us to study the 3D redshift-space distribution of absorbing galaxies on small scales in a sample that is tiny by galaxy standards. We learn about the distribution of the pair-wise velocities of the haloes that contain the absorbers and we obtain limits on the peculiar velocities of the gas relative to the haloes. We now list our results.

(1) We detect for the first time a significant excess of coincident absorbers in paired sightlines separated by about 1 Mpc. We see the coincidences in the bin near zero in Figs 6(d) and 7(d) where we include associated systems, those within 3000 km s^{-1} of their QSOs. We still see the coincidences in Figs 6(e) and 7(e) where we removed all associated absorbers. Fig. 7(e) shows 13 absorber-absorber coincidences with redshift differences of $< 200 \text{ km s}^{-1}$. The probability of finding ≥ 13 , where we expect 2.237 by chance, is 7.2×10^{-7} .

(2) For each absorber, we define the impact parameter as the distance, in the plane of the sky, from that absorber to the LOS to the partner QSOs. These impact parameters have an approximately uniform distribution from 0.1 to 2.5 Mpc (Figs 11 and 12). Overall, the chance of seeing an AA coincidence, one with a redshift difference $|\Delta z_{\text{AA}}| < 0.005$, is 2.8 per cent per detected absorption system, or 1.7 per cent if we subtract the random background.

(3) The chance of seeing an AA coincidence declines rapidly with increasing distance between the LOS from 0.1 to 2.5 Mpc (Figs 11, 12 and Table 10). This decline reminds us of galaxy clustering. If we see an absorber in one QSO spectrum, the chance of absorption in the partner spectrum is at least ≈ 50 per cent at $< 100 \text{ kpc}$, declining rapidly from 23 per cent at $100\text{--}200 \text{ kpc}$ to 0.7 per cent by 1–2 Mpc. These probabilities are very much lower limits because high-resolution spectra with high S/N and full wavelength coverage would show factors of several more absorbers. Coppolani et al. (2006) did not see any significant correlation in 139 C_{IV} systems towards 32 pairs of QSOs, except for an overdensity of C_{IV} in front of a group of four QSOs. Their QSOs had a mean separation of greater than 2 arcmin, corresponding to linear distances that are too large.

(4) The redshifts of the AA coincident absorbers seen in the paired sightlines are remarkably similar. We can fit the differences in their velocities (Fig. 7d) with a straight line for the random background plus a Gaussian with a mean of zero and a standard deviation of only 85 km s^{-1} . This small dispersion leads us to conclude that the absorbers arise in quiescent gas in the haloes of a population of galaxies with low random peculiar velocities.

(5) The redshift-space distribution of absorbers around other absorbers is consistent with normal galaxy clustering, normal systematic infalling velocities and a small value for the random pair-wise

velocity parameter σ_{12} (equation 10). The redshift-space distribution of the 23 AA absorbers separated by $< 2.5 \text{ Mpc}$ favours $\sigma_{12} = 0$, with a 1σ upper limit of 100 km s^{-1} and a 2σ limit of 300 km s^{-1} . This suggests that the absorbers are in the haloes of blue galaxies (Figs 17 and 18). Red galaxies have larger random velocities (Section 7.7) and would produce larger differences in the redshifts between the two LOS.

We expect that the distribution of halo masses sets both the infalling velocity field and the pair-wise random velocities σ_{12} . In Fig. 18 we saw that changing the halo mass distribution from $\propto M^{-1}$ to $\propto M^{-2}$ had no effect on the allowed σ_{12} values because low-mass haloes dominate in both cases. The Kim & Croft (2007) simulations show only a small decrease in the infalling velocities for decreasing halo mass below $\sim 2.9 \times 10^{10}$ solar masses. Hence it is unclear if even much lower halo mass would allow the data to be consistent with significantly larger velocity dispersions, from either pair-wise random motions or from winds. We also found that a model with more high-mass haloes gave similar results to a model with no infall, and that both give lower likelihoods for the data.

(6) The compact redshift-space distribution of the absorbers is not compatible with most absorbers we see arising in winds flowing quickly out from galaxies. Absorption in gas flowing out from galaxies at a mean velocity of 250 km s^{-1} would produce more velocity smearing than we see. The winds seen by Adelberger et al. (2005a) in LBG spectra are not representative of absorption systems that we see. Either the winds they see are confined to the star-forming regions of LBGs, or they do not extend to $> 40 \text{ kpc}$ with large velocities while still making absorption we can detect. We observe the same ions seen in the LBG spectra and we are typically sensitive to much weaker lines. We are compatible at the 2σ level with 1/3 of strong metal-line systems coming from fast winds. When we assign z_{abs} values, we attempt to use the relatively weak lines to give the value for the component with the largest column density, rather than a mean for all the components.

In a similar vein, Rauch et al. (2001) found that the Ly α absorption in two pairs of QSOs separated by 86 pc at $z \sim 3.3$ was very similar, implying that strong winds blowing for a substantial fraction of the Hubble time fill less than 20 per cent of the volume of the universe. This result refers to the lower column densities in lower density parts of the IGM that we will typically not detect. Our results and theirs both imply that most metals do not enter the IGM in fast winds at $z = 2\text{--}3$. Instead, metals probably entered the IGM gradually over many epochs, and most metals in the IGM at $z = 2$ were in place long before that epoch.

10.3 EA absorbers near QSOs

We also studied how absorbers are distributed around the QSOs. If absorbers are in galaxy haloes, and QSOs are in typical galaxies, we would expect the absorber-absorber correlation to be similar to the QSO-absorber correlation.

(7) We see excess absorption when light passes a QSO. We see these absorbers in the bins near zero in Fig. 6(b). The a posteriori probability of seeing ≥ 16 when we expect 5.77 at $0\text{--}600 \text{ km s}^{-1}$ is 0.0003, while probability of seeing ≥ 21 when we expect 11.53 in the range $\pm 600 \text{ km s}^{-1}$ is 0.008.

(8) The absorbers we see when we pass a QSO (Fig. 7b) are not the same as those we see when we look directly at the QSOs (Fig. 7a). Three tests in Section 5.3.1 show that the probability that the velocities in the range $\pm 2000 \text{ km s}^{-1}$ come from the same population is 0.5–0.9 per cent. The LOS absorbers have a mean

of $658 \pm 90 \text{ km s}^{-1}$ while the transverse absorbers have a mean of $213 \pm 146 \text{ km s}^{-1}$, showing that the transverse absorbers know with more precision the systemic velocity of the other QSO, that giving the z_{em} , than do its own LOS associated absorbers. The excess transverse absorbers are probably in the haloes of galaxies near the QSOs.

(9) The velocity distribution of the excess transverse absorbers includes terms from the z_{em} errors and the pair-wise velocity dispersions of QSOs relative to absorbers. We know that either term can be as large or larger than the small mean $\sim 300 \text{ km s}^{-1}$ and dispersion $\sigma \sim 250 \text{ km s}^{-1}$ that we see.

(10) The 10 excess EA absorbers are all in two bins at 0–200 and 400–600 km s^{-1} in Fig. 7(b). It may be an accident that these are all at positive velocities because there is a 4.8 per cent probability of a larger mean for all the velocities in the a posteriori range $\pm 600 \text{ km s}^{-1}$. The EA absorbers may appear to be in front of the QSOs because our redshifts are too large by $\sim 300 \text{ km s}^{-1}$. A 300 km s^{-1} shift is near the upper limit allowed by the distribution of H_I in a subset of these QSOs (Kirkman et al. 2008) because it would lead to too much H_I absorption behind the QSOs. Alternatively, there might be a real preference for absorption systems to be in front of QSOs. In Kirkman et al. (2008) we find an excess of H_I behind these QSOs, which might come from some hypothetical anisotropy in the QSO UV emission, or from isotropic UV emission that lasted less than $\sim 1 \text{ Myr}$.

(11) The excess absorbers near the QSOs (Fig. 7b) have a small $\sim 250 \text{ km s}^{-1}$ velocity dispersion suggesting that both these EA absorbers and the QSOs are in the blue sequence of galaxies, and that some, perhaps many, of the QSOs have z_{em} errors $\sim 300 \text{ km s}^{-1}$. We would need a much larger sample to put this result on a secure statistical basis.

(12) In Section 6 we saw that 14 of the 16 EA absorbers show C IV lines and we expect C IV in the remaining two. These C IV lines tend to have smaller than typical W_{rest} values (Fig. 9), probably because the lines are in regions of the spectra with higher than average S/N. We see no excess of N V (Table 5), though we did not search for N V in each case, and we would not be able to see N V in many cases.

(13) The probability of seeing absorption when light passes a QSO is approximately constant for impact parameters 0.1–2.5 Mpc (Figs 21 and 22), with only a slight increase at small impact parameters. We expected a strong increase from galaxy clustering because QSOs are in normal galaxies; hence we suspect that the QSOs destroy the nearest absorbers. Wild et al. (2008) find that they can best explain the numbers of C IV looking towards QSOs if those QSOs destroy all C IV out to $\sim 300 \text{ kpc}$.

(14) The overall probability of seeing an AA absorber when we pass another absorber is ~ 2.8 per cent compared to ~ 9.5 per cent when we pass a QSO (EA6 or EA). These rates drop to ~ 1.7 and 6.1 per cent when we remove the background absorbers. The rate of detecting absorbers near to QSOs is probably higher than near other absorbers because the EA absorbers are typically seen in the emission lines and towards the red end of spectra where the S/N is highest allowing us to see more absorbers per unit velocity. In addition, some of the EA absorbers near to QSOs will be ejected gas in the background QSO spectrum, that appear near the foreground QSO z_{em} value because the z_{em} of the paired QSOs are similar.

(15) We rarely see the transverse absorbers along the LOS to individual QSOs (Section 8.4). When an LOS passes a QSO we see excess transverse absorbers in ~ 6 per cent of cases at $0 < v_{\text{EA}} < 600 \text{ km s}^{-1}$ (Section 8.2). When we look straight at the individual QSOs, < 2 per cent (95 per cent limit, Section 8.4) of cases show excess absorption at these velocities. We might double this to

< 4 per cent to account for absorption behind the QSO. If QSOs were normal galaxies with no special effects on their environment, we would expect more absorbers in the LOS to QSOs because this ends in the centre of a galaxy. However, we know that QSOs destroy the nearest absorbers. Wild et al. (2008) show this on large scale, and we see only a slight increase in the number of transverse absorbers as the impact parameter drops from 2.5 to 0.1 Mpc. We can understand these trends if the destruction of absorbers cancels much of the increase expected from galaxy clustering. Since we more often see absorbers in the plane of the sky than along the LOS to the QSOs, we can conclude that there is more destruction in the LOS than in the plane of the sky. An LOS that ends at a QSO is less likely to show an absorber than one that passes within about $\sim 1 \text{ Mpc}$ of the QSO.

Bowen et al. (2006) saw extra Mg II transverse absorbers in four out of four cases, all at impact parameters $< 100 \text{ kpc}$ where we expect absorption in the QSOs host galaxies. Hennawi et al. (2006a) report excess LLS and DLA transverse absorbers compared to LOS at similar impact parameters to ours. They compare the absolute numbers of absorbers in their samples to other samples, and their results are suspect because these values are sensitive to the precise minimum column density in their sample.

(16) Excluding the LOS to us, the distribution of absorbers around QSOs (Fig. 24) seems isotropic, with the exception of the possible tendency (item 10 above) for the EAs to be on the front side of the QSOs. The patterns expected if QSO UV radiation is confined to narrow cones, or if episodic lifetimes are under 1 Myr (Fig. 25) are much too subtle to detect with the current data.

(17) We measured redshifts for the QSO using the Mg II line where possible, and correcting to this line in other cases, all to approximate the systemic redshifts of the galaxy hosts. We do not know the errors on these redshifts, but speculate that a mixture of Gaussians with different dispersions (Section 8.5) would be a better model than a single Gaussian. We believe that the absorbers with $z_{\text{abs}} \gg z_{\text{em}}$ typically indicate that the z_{em} values are too small, in some cases by many hundred km s^{-1} . At the other extreme, the distribution of the excess EA absorbers (Fig. 7b) suggest small errors $< 300 \text{ km s}^{-1}$ for other QSOs.

ACKNOWLEDGMENTS

We obtained spectra using the Kast spectrograph on the Lick Observatory 3-m Shane telescope, and LRIS spectrograph on the Keck-I telescope. The W. M. Keck Observatory is operated as a scientific partnership among the California Institute of Technology, the University of California and the National Aeronautics and Space Administration and was made possible by the generous financial support of the W. M. Keck Foundation. We are exceedingly grateful for the help we receive from the staff at both observatories. We recognize and acknowledge the very significant cultural role and reverence that the summit of Mauna Kea has always had within the indigenous Hawaiian community. We are extremely grateful to have the opportunity to conduct observations from this mountain. Former UCSD students John O'Meara and Nao Suzuki helped to obtain some of the spectra used in this paper. We thank Don Schneider, Chuck Steidel, Jason Prochaska, Jeffrey Newman, Jeff Cooke, Mat Malkan, Gordon Richards and Peter Bartel for important discussions. Our work was inspired by the pioneering work of Chuck Steidel and his collaborators. We are delighted to thank Jim Peebles for long ago stimulating our interest in the study of the correlation of absorption in spectra of pairs of QSOs. Angela

Chapman was funded by the NSF REU programme grant to the Physics Department at UCSD. This work was funded in part by NSF grants AST-0098731, 0507717 and 0808168 and by NASA grants NAG5-13113.

REFERENCES

- Adelberger K. L., 2004, *ApJ*, 612, 706
 Adelberger K. L., 2005, in Williams P., Shu C.-G., Menard B., eds, IAU Colloq. 199: Probing Galaxies through Quasar Absorption Lines. Cambridge Univ. Press, Cambridge, p. 341
 Adelberger K. L., Steidel C. C., 2005, *ApJ*, 630, 50
 Adelberger K. L., Shapley A. E., Steidel C. C., Pettini M., Erb D. K., Reddy N. A., 2005a, *ApJ*, 629, 636
 Adelberger K. L., Steidel C. C., Pettini M., Shapley A. E., Reddy N. A., Erb D. K., 2005b, *ApJ*, 619, 697
 Adelberger K. L., Steidel C. C., Kollmeier J. A., Reddy N. A., 2006, *ApJ*, 637, 74
 Antonucci R., 1993, *A&A*, 31, 473
 Barthel P. D., 1989, *ApJ*, 336, 606
 Barthel P. D., Tytler D. R., Thomson B., 1990, *A&A*, 82, 339
 Best P. N., 2007, *New Astron. Rev.*, 51, 168
 Bowen D. V. et al., 2006, *ApJ*, 645, L105
 Boyle B. J., Smith R. J., Shanks T., Croom S. M., Miller L., 1997, in Sato K., ed., Proc. IAU Symp. 183, Cosmological Parameters and the Evolution of the Universe. Kluwer Academic Publishers, Dordrecht
 Broadhurst T. J., Ellis R. S., Koo D. C., Szalay A. S., 1990, *Nat*, 343, 726
 Chelouche D., Ménard B., Bowen D. V., Gnat O., 2008, *ApJ*, 683, 55
 Chen H., Lanzetta K. M., Webb J. K., 2001, *ApJ*, 556, 158
 Churchill C. W., Kacprzak G. G., Steidel C. C., Evans J. L., 2007, *ApJ*, 661, 714
 Coil A. L., Hennawi J. F., Newman J. A., Cooper M. C., Davis M., 2007, *ApJ*, 654, 115
 Coil A. L. et al., 2008, *ApJ*, 672, 153
 Conover W. J., 1980, Practical Nonparametric Statistics, 2nd edn. Wiley, New York, lc1980
 Constantin A., Vogeley M. S., 2006, *ApJ*, 650, 727
 Cooke J., Wolfe A. M., Gawiser E., Prochaska J. X., 2006, *ApJ*, 652, 994
 Coppolani F. et al., 2006, *MNRAS*, 370, 1804
 Cristiani S., D'Odorico S., D'Odorico V., Fontana A., Giallongo E., Savaglio S., 1997, *MNRAS*, 285, 209
 Croft R. A. C., 2004, *ApJ*, 610, 642
 Croom S. M. et al., 2005, *MNRAS*, 356, 415
 Crotts A. P. S., 1989, *ApJ*, 336, 550
 Crotts A. P. S., Fang Y., 1998, *ApJ*, 502, 16
 Crotts A. P. S., Bechtold J., Fang Y., Duncan R. C., 1994, *ApJ*, 437, L79
 Crotts A. P. S., Burles S., Tytler D., 1997, *ApJ*, 489, L7
 Davis M., Peebles P. J. E., 1983, *ApJ*, 267, 465
 Di Matteo T., Springel V., Hernquist L., 2005, *Nat*, 433, 604
 Diaferio A., Geller M. J., 1996, *ApJ*, 467, 19
 Dobrzański A., Bechtold J., 1991a, *ApJ*, 377, L69
 Dobrzański A., Bechtold J., 1991b, in Crampton D., ed., ASP Conf. Ser. Vol. 21, The Space Distribution of Quasars. Astron. Soc. Pac., San Francisco, p. 272
 D'Odorico V., Petitjean P., Cristiani S., 2002, *A&A*, 390, 13
 D'Odorico V., Bruscoli M., Saitta F., Fontanot F., Viel M., Cristiani S., Monaco P., 2008, *MNRAS*, 389, 1727
 Faucher-Giguere C., Lidz A., Zaldarriaga M., Hernquist L., 2008, *ApJ*, 688, 85
 Fechner C., Richter P., 2008, preprint (arXiv:0807.4638)
 Fernandez-Soto A., Barcons X., Carballo R., Webb J. K., 1995, *MNRAS*, 277, 235
 Ganguly R., Brotherton M. S., 2008, *ApJ*, 672, 102
 Gaskell C. M., 1982, *ApJ*, 263, 79
 Gaskell C. M., 1983, *ApJ*, 267, L1
 Goncalves T. S., Steidel C. C., Pettini M., 2008, *ApJ*, 676, 816
 Guimarães R., Petitjean P., Rollinde E., de Carvalho R. R., Djorgovski S. G., Srianand R., Aghaee A., Castro S., 2007, *MNRAS*, 377, 657
 Hamilton T. S., Casertano S., Turnshek D. A., 2002, *ApJ*, 576, 61
 Hennawi J. F., Prochaska J. X., 2007, *ApJ*, 655, 735
 Hennawi J. F. et al., 2006a, *ApJ*, 651, 61
 Hennawi J. F. et al., 2006b, *AJ*, 131, 1
 Hui L., Stebbins A., Burles S., 1999, *ApJ*, 511, L5
 Jakobsen P., Perryman M. A. C., 1992, *ApJ*, 392, 432
 Jakobsen P., Perryman M. A. C., di Serego Alighieri S., Ulrich M. H., Macchetto F., 1986, *ApJ*, 303, L27
 Jakobsen P., Jansen R. A., Wagner S., Reimers D., 2003, *A&A*, 397, 891
 Kaiser N., 1987, *MNRAS*, 227, 1
 Kaiser N., 1988, *MNRAS*, 231, 149
 Kendall M., Stewart A., 1979, The Advanced Theory of Statistics, 4th edn. Charles Griffin & Co. Ltd., London, lc1979
 Kim Y.-R., Croft R., 2007, preprint (astro-ph/0701012)
 Kirkman D., Tytler D., Gleed M., 2008, *MNRAS*, 387, 377
 Lanzetta K. M., Bowen D., 1990, *ApJ*, 357, 321
 Li C., Jing Y. P., Kauffmann G., Börner G., White S. D. M., Cheng F. Z., 2006, *MNRAS*, 368, 37
 Liske J., 2000, *MNRAS*, 319, 557
 Liske J., Williger G. M., 2001, *MNRAS*, 328, 653
 Loeb A., Eisenstein D. J., 1995, *ApJ*, 448, 17
 Loh J.-M., Quashnock J. M., Stein M. L., 2001, *ApJ*, 560, 606
 Lupton R., 1993, Statistics in Theory and Practice. Princeton Univ. Press, Princeton, NJ, lc1993
 Madgwick D. et al., 2003, *MNRAS*, 344, 847
 McCarthy J. K. et al., 1998, in D'Odorico S., ed., Proc. SPIE Vol. 3355, Optical Astronomical Instrumentation. Bellingham, WA, p. 81
 McDonald P., 2003, *ApJ*, 585, 34
 McDonald P., Miralda-Escudé J., 1999, *ApJ*, 518, 24
 Miller L., Lopes A. M., Smith R. J., Croom S. M., Boyle B. J., Shanks T., Outram P., 2004, *MNRAS*, 348, 395
 Milutinovic N. et al., 2007, *MNRAS*, 382, 1094
 Misawa T., Eracleous M., Charlton J. C., Tajitsu A., 2005, *ApJ*, 629, 115
 Misawa T., Charlton J. C., Eracleous M., Ganguly R., Tytler D., Kirkman D., Suzuki N., Lubin D., 2007, *ApJS*, 171, 1
 Moller P., Kjaergaard P., 1992, *A&A*, 258, 234
 Narayanan D., Hamann F., Barlow T., Burbidge E. M., Cohen R. D., Junkkarinen V., Lyons R., 2004, *ApJ*, 601, 715
 Nestor D., Hamann F., Rodriguez Hidalgo P., 2008, *MNRAS*, 386, 2055
 Oke J. B. et al., 1995, *PASP*, 107, 375
 Pen U.-L., 1999, *ApJS*, 120, 49
 Petitjean P., Bergeron J., 1990, *A&A*, 231, 309
 Petitjean P., Bergeron J., 1994, *A&A*, 283, 759
 Petitjean P., Rauch M., Carswell R. F., 1994, *A&A*, 291, 29
 Pichon C., Scannapieco E., Aracil B., Petitjean P., Aubert D., Bergeron J., Colombi S., 2003, *ApJ*, 597, L97
 Pieri M. M., Schaye J., Aguirre A., 2006, *ApJ*, 638, 45
 Prochaska J. X., Hennawi J. F., Herbert-Fort S., 2008, *ApJ*, 675, 1002
 Quashnock J. M., vanden Berk D. E., York D. G., 1996, *ApJ*, 472, L69
 Rauch M., Sargent W. L. W., Womble D. S., Barlow T. A., 1996, *ApJ*, 467, L5
 Rauch M., Sargent W. L. W., Barlow T. A., Carswell R. F., 2001, *ApJ*, 562, 76
 Rauch M., Sargent W. L. W., Barlow T. A., Simcoe R. A., 2002, *ApJ*, 576, 45
 Richards G. T., York D. G., Yanny B., Kollgaard R. I., Laurent-Muehleisen S. A., vanden Berk D. E., 1999, *ApJ*, 513, 576
 Richards G. T., Vanden Berk D. E., Reichard T. A., Hall P. B., Schneider D. P., SubbaRao M., Thakar A. R., York D. G., 2002, *AJ*, 124, 1
 Rollinde E., Petitjean P., Pichon C., Colombi S., Aracil B., D'Odorico V., Haehnelt M. G., 2003, *MNRAS*, 341, 1279
 Rollinde E., Srianand R., Theuns T., Petitjean P., Chand H., 2005, *MNRAS*, 361, 1015
 Romani R. W., Filippenko A. V., Steidel C. C., 1991, *PASP*, 103, 154
 Russell D. M., Ellison S. L., Benn C. R., 2006, *MNRAS*, 367, 412

- Sargent W. L. W., Steidel C. C., 1987, ApJ, 322, 142
 Sargent W., Young P., Boksenberg A., Tytler D., 1980, ApJS, 42, 41
 Sargent W. L. W., Boksenberg A., Young P., 1982, ApJ, 252, 54
 Sargent W. L. W., Boksenberg A., Steidel C. C., 1988, ApJS, 68, 539
 Sargent W. L. W., Steidel C. C., Boksenberg A., 1989, ApJS, 69, 703
 Scannapieco E., 2005, ApJ, 624, L1
 Scannapieco E., Pichon C., Aracil B., Petitjean P., Thacker R. J., Pogosyan D., Bergeron J., Couchman H. M. P., 2006, MNRAS, 365, 615
 Schirber M., Miralda-Escudé J., McDonald P., 2004, ApJ, 610, 105
 Scoccimarro R., 2004, Phys. Rev. D, 70, 083007
 Shanks T., Boyle B. J., Croom S., Loaring N., Miller L., Smith R. J., 2000, in Mazure A., Le Fèvre O., Le Brun V., eds, ASP Conf. Ser. Vol. 200, Clustering at High Redshift. Astron. Soc. Pac., San Francisco, p. 57
 Shaver P. A., Robertson J. G., 1983, ApJ, 268, L57
 Shaver P. A., Robertson J. G., 1985, MNRAS, 212, 15P
 Shaver P. A., Boksenberg A., Robertson J. G., 1982, ApJ, 261, L7
 Shen Y. et al., 2007, AJ, 133, 2222
 Simcoe R. A., Sargent W. L. W., Rauch M., Becker G., 2006, ApJ, 637, 648
 Slosar A., Seljak U., Tasitsiomi A., 2006, MNRAS, 366, 1455
 Srianand R., 1997, ApJ, 478, 511
 Steidel C. C., Sargent W. L. W., 1991, AJ, 102, 1610
 Suzuki N., Tytler D., Kirkman D., O'Meara J. M., Lubin D., 2003, PASP, 115, 1050
 Tonry J. L., 1998, AJ, 115, 1
 Tytler D., 1982, Nat, 298, 427
 Tytler D., 1987, ApJ, 321, 49
 Tytler D., Fan X.-M., 1992, ApJS, 79, 1
 Tytler D., Sandoval J., Fan X.-M., 1993, ApJ, 405, 57
 Tytler D., O'Meara J. M., Suzuki N., Kirkman D., Lubin D., Orin A., 2004, AJ, 128, 1058
 Urry C. M., Padovani P., 1995, PASP, 107, 803
 Vale A., Ostriker J. P., 2004, MNRAS, 353, 189
 Vanden Berk D. E. E., 2001, AJ, 122, 549
 Vanden Berk D. E., Stoughton C., Crots A. P. S., Tytler D., Kirkman D., 2000, AJ, 119, 2571
 Visbal E., Croft R. A. C., 2008, ApJ, 674, 660
 Wake D. A. et al., 2004, ApJ, 610, L85
 Weymann R. J., Carswell R. F., Smith M. G., 1981, ARA&A, 19, 41
 Wild V. et al., 2008, MNRAS, 388, 227
 Williger G. M., Hazard C., Baldwin J. A., McMahon R. G., 1996, ApJS, 104, 145
 Wise J. H., Eracleous M., Charlton J. C., Ganguly R., 2004, ApJ, 613, 129
 Worseck G., Wisotzki L., 2006, A&A, 450, 495
 Worseck G., Wisotzki L., 2007, in Metcalfe N., Shanks T., eds, ASP Conf. Ser. Vol. 379, Cosmic Frontiers. Astron. Soc. Pac., San Francisco, p. 235
 Worseck G., Fechner C., Wisotzki L., Dall'Aglio A., 2007, A&A, 473, 805
 Wright E. L., 2006, PASP, 118, 1711
 York D. G. E., 2000, AJ, 120, 1579
 Young P., Sargent W. L. W., Boksenberg A., 1982, ApJS, 48, 455
 Zehavi I. et al., 2002, ApJ, 571, 172

APPENDIX A: OBSERVATIONS

In Table A1, we give the observation date, the width of the slit we used, the set-up, exposure times and the S/N per pixel for each spectrum. Unless otherwise noted, we measured the S/N at 4200 Å for spectra observed with the A2 or B2 set-up, and at 5200 Å for spectra observed with the A1 or B1 set-up. We give the S/N for a subsample of the spectra. The majority of the QSOs were observed using the 0.7 arcsec slit but we used a 1.0 arcsec slit for 29 QSOs. Exposure times for the objects ran from 460 to 8000 s. Spectra were extracted using the standard `IRAF` extraction packages or our own

Table A1. Keck LRIS Observations.

Label	Date	Slit	Set-up	Exposure time (s)		
				Blue	Red	S/N
P1a	11/2001	0.7	B2, C4	1200	1200	35
P1b	11/2001	0.7	B2, C4	900	900	54
P2a	11/2001	0.7	B2, C4	2700	2700	46
P2b	11/2001	0.7	B2, C4	3600	3600	55
P3a	10/2001	0.7	B2, C4	2700	2700	17
P3a	08/2002	0.7	A1, C4	2400	2400	
P3a	09/2004	1.0	A1, C4	2200	2200	
P3b	10/2001	0.7	B2, C4	3600	3600	45
P3b	08/2002	0.7	A1, C4	462	462	
P3b	09/2004	1.0	A1, C4	3600	3600	
P4a	10/2001	0.7	B2, C4	900	900	6
P4a	11/2001	0.7	B2, C4	900	900	
P4a	09/2004	1.0	A1, C4	1800	1800	
P4a	09/2004	1.0	A1, C4	2400	2400	
P4b	10/2001	0.7	B2, C4	600	600	42
P4b	08/2002	0.7	A1, C4	300	300	
P5a	10/2001	0.7	B2, C4	424	423	32
P5a	10/2001	0.7	B2, C4	900	900	32
P5a	08/2002	0.7	A1, C4	2400	2400	
P5b	10/2001	0.7	B2, C4	1800	1800	51
P6a	08/2001	0.7	B2, C3	1200	1200	10
P6b	08/2001	0.7	B2, C3	1200	1200	16
P7a	03/2003	0.7	A1, C4	5400	5250	23
P7b	03/2003	0.7	A1, C4	5600	5400	26
P8a	03/2003	0.7	A1, C4	3600	3450	33
P8a	03/2003	1.0	A1, C4	2300	2300	
P8b	04/2001	0.7	B1, C4	1800	1800	17
P8b	03/2003	1.0	A1, C4	3600	3600	
P8c	04/2001	0.7	B1, C4	1800	1800	12
P9a	03/2003	1.0	A1, C4	1000	1000	33
P9b	03/2003	0.7	A1, C4	3600	3420	21
P10a	04/2001	0.7	B1, C4	3000	3000	10
P10b	04/2001	0.7	B1, C4	3000	3000	7
P11a	03/2003	0.7	A1, C4	5400	5250	35
P11b	03/2003	0.7	A1, C4	5400	5250	16
P11b	04/2004	0.7	A1, C4	4600	4600	
P12a	03/2003	0.7	A1, C4	3300	3150	30
P12b	03/2003	0.7	A1, C4	3300	3150	20
P13a	03/2003	0.7	A1, C4	2700	2550	41
P13b	03/2003	0.7	A1, C4	2700	2550	36
P14a	03/2003	0.7	A1, C4	2900	2750	13
P14b	03/2003	0.7	A1, C4	1500	1350	13
P15a	07/2002	0.7	A1, C4	7262	7262	22
P15b	08/2002	0.7	A1, —	3200	—	5 ^a
P16a	07/2002	0.7	A2, C3	1800	1800	47
P16b	07/2002	0.7	A2, C3	1800	1800	40
P17a	04/2001	0.7	B1, C4	2400	2400	24
P17b	04/2001	0.7	B1, C4	2700	2700	39
P18a	07/2002	0.7	A2, C3	2700	2700	21 ^b
P18b	08/2001	0.7	—, C3	—	3600	19 ^c
P19a	07/2002	0.7	A2, C3	2300	2300	34
P19b	07/2002	0.7	A2, C3	2100	2100	35
P20a	07/2002	0.7	A2, C3	900	900	8
P20a	08/2002	0.7	A1, C4	3421	3421	
P20b	07/2002	0.7	A2, C3	1500	1500	31
P21a	07/2002	0.7	A1, C4	5400	5400	33
P21b	07/2002	0.7	A1, C4	3600	3600	40
P22a	08/2001	0.7	B2, C3	1200	1200	29
P22b	08/2001	0.7	B2, C3	3600	3600	42
P22c	08/2001	0.7	B2, C3	1901	1046	73
P23a	08/2001	0.7	B2, C3	900	900	25
P23b	10/2001	0.7	B2, C4	2700	2700	6
P24a	11/2001	0.7	B2, C4	3300	3300	23

Table A1 – *continued.*

Label	Date	Slit	Set-up	Exposure time (s)		
				Blue	Red	S/N
P24b	11/2001	0.7	B2, C4	1500	1500	22
P25a	04/2004	0.7	B1, C4	3600	3600	
P25b	04/2004	0.7	B1, C4	600	600	
P26a	04/2004	0.7	B1, C4	2160	2160	
P26b	04/2004	0.7	B1, C4	4100	4100	
P27a	04/2004	0.7	B1, C4	3914	3914	
P27b	04/2004	0.7	B1, C4	4900	4900	
P28a	08/2003	3.3	LICK	3601	3601	
P28b	04/2004	0.7	B1, C4	2800	2800	
P29a	07/2002	0.7	A1, C4	4600	4600	
P29b	07/2002	0.7	A1, C4	2880	2880	
P30a	09/2004	1.0	A1, C4	2700	2700	
P30b	09/2004	1.0	A1, C4	4500	4500	
P31a	09/2004	1.0	A1, C4	1800	1800	
P31b	09/2004	1.0	A1, C4	1800	1800	
P32a	09/2004	1.5	A1, C4	2400	2400	
P32b	09/2004	1.5	A1, C4	2200	2200	
P34a	09/2004	1.0	A1, C4	2300	2300	
P34b	09/2004	1.0	A1, C4	3200	3200	
P35a	09/2004	1.5	A1, C4	2400	2400	
P35b	09/2004	1.5	A1, C4	1200	1200	
P36a	09/2004	1.0	A1, C4	1800	1800	
P36b	09/2004	1.0	A1, C4	5400	5400	
P37a	09/2003	1.0	A5, C4	2200	2200	
P37b	09/2003	1.0	A5, C4	4000	4000	
P38a	09/2003	1.0	A1, C4	4800	4800	
P38b	09/2003	1.0	A1, C4	2500	2500	
P39a	09/2003	1.0	A1, C4	2500	2500	
P39b	09/2003	1.0	A1, C4	3050	3050	
P40a	09/2003	1.0	A1, C4	5100	5100	
P40b	09/2003	1.0	A1, C4	3700	3700	
P41a	09/2003	2.3	LICK	4805	4805	
P41b	09/2003	2.3	LICK	4800	4800	
P42a	09/2003	1.0	A1, C4	3000	3000	
P42b	09/2003	1.0	A1, C4	5400	5400	
P43a	09/2003	1.0	A1, C4	3600	3600	
P43b	09/2003	1.0	A1, C4	2300	2300	
P44a	09/2003	1.0	A1, C4	2000	2000	
P44b	09/2003	1.0	A1, C4	1500	1500	
P45a	08/2003	3.3	LICK	4802	4802	
P45b	08/2003	3.3	LICK	6303	6303	
P46a	12/2004	2.3	LICK	4802	4802	
P49a	03/2005	2.3	LICK	5421	5421	
P50b	03/2005	2.3	LICK	5403	5403	
P51a	03/2005	2.3	LICK	1451	1451	
P51b	03/2005	2.3	LICK	4515	4515	
P52a	12/2004	2.3	LICK	9005	9005	
P52b	03/2005	2.3	LICK	5402	5402	
P53a	03/2005	2.3	LICK	5407	5407	
P54a	03/2005	2.3	LICK	3622	3622	
P55b	03/2005	2.3	LICK	5406	5406	
P56c	03/2005	2.3	LICK	5405	5405	
P57a	03/2005	2.3	LICK	5404	5404	
P58b	03/2005	2.3	LICK	5413	5413	
P60a	03/2005	2.3	LICK	4513	4513	
P61a	03/2005	2.3	LICK	5403	5403	
P61b	03/2005	2.3	LICK	5402	5402	
P62a	03/2005	2.3	LICK	5400	5400	
P63b	03/2005	2.3	LICK	5410	5410	
P64b	03/2005	2.3	LICK	5408	5408	
P65b	03/2005	2.3	LICK	4524	4524	
P66b	08/2003	3.3	LICK	4000	4000	
P67a	08/2003	3.3	LICK	3602	3602	

Table A1 – *continued.*

Label	Date	Slit	Set-up	Exposure time (s)		
				Blue	Red	S/N
P69a	09/1998	2.0	LICK	5400	5400	
P70b	09/2003	2.0	LICK	7200	7200	
P72b	03/2005	2.0	LICK	5400	5400	
P73b	04/2002		LICK	3600	3600	
P74a	06/2006	2.0	LICK	5400	5400	
P74b	06/2006	2.0	LICK	3600	3600	
P75a	06/2006	2.0	LICK	3600	3600	
P75b	06/2006	2.0	LICK	4500	4500	
P76b	06/2006	2.0	LICK	2700	2700	
P77a	04/2004	0.7	A1, C4	1000	1000	
P77a	06/2006	2.0	LICK	6000	6000	
P77b	06/2006	2.0	LICK	6000	6000	
P78a	06/2006	2.0	LICK	3600	3600	
P79a	06/2006	2.0	LICK	6000	6000	
P79b	06/2006	2.0	LICK	6000	6000	
P80a	06/2006	2.0	LICK	2800	2800	
P80b	04/2005	2.0	LICK	2900	2900	
P81a	06/2006	2.0	LICK	6000	6000	
P81b	06/2006	2.0	LICK	4600	4600	
P82a	04/2004	0.7	A1, C4	3602	3602	
P116a	10/1998		D1			4
P116b	10/1998		D1			9
P117a	12/1994 ^c		D2			18
P117b	12/1994 ^c		D2			17
P118a	06/1995		D3			17
P118b	06/1995		D3			13
P118c	06/1995		D3			21
P119a	10/1998 ^d		D4			8
P119b	10/1998 ^d		D4			26
P120a	10/1998 ^d		D4			19
P120b	10/1998 ^d		D4			18

^aS/N measured at 3800 Å. ^bS/N measured at 6500 Å. ^cAlso 1995 January 25. ^dAlso 1999 June 16–17.

software that is designed to give accurate flux calibration with the optimal S/N. We only list a pair if we obtained spectra of one or both QSOs. We do not list a pair if we used SDSS spectra alone.

The spectra from Lick observatory used the Kast Double Spectrograph on the 3-m Shane telescope. We typically used the 830 groves mm⁻¹ grism blazed at 3460 Å in the blue camera and a 1200 grooves mm⁻¹ grating blazed at 5000 Å in the red camera. A dichroic with a 50 per cent transmission near 4600 Å was used to cover 3175–5880 Å with no gaps. The dispersion are 1.13 Å pixel⁻¹ in the blue and 1.17 Å in the red. The typical slit width gives approximately 2.5 pixels per FWHM, depending on the wavelength and focus setting. We show similar spectra in Tytler et al. (2004).

APPENDIX B: COMMENTS ON INDIVIDUAL SYSTEMS

B1 P1

EAV and AAA coincidences. For EAV15 an absorption system in P1a is coincident with the z_{em} of P1b. The C IV and N V are slightly to the blue of their emission lines. Both absorbers are single velocity components. The N V $\lambda 1242.80$ transition is blended with unidentified absorption. For AAA21 the same system in P1a is coincident with a system showing a single velocity component in C IV and Si IV.

B2 P3

An AA coincidence. Both P3a and P3b show strong Mg II and Fe II absorption. There are two velocity components in the Mg II absorption of P3b. The Mg I in P3b shows a single velocity component. The Mg II and Fe II in P3a are also single velocity components.

B3 P5

EAV, AA, AAA and AAV coincidences. For AA2 both P5a and P5b show single velocity components in C IV absorption. For EAV17 an absorption system in P5a is coincident with the z_{em} of P5b. AAA27 consists of this same absorption system in P5a and a system in P5b that shows single velocity components in C IV and Si IV. AAV19 consists of an absorption system in P5a containing single velocity components in C IV and Si IV and an absorption system in P5b containing a single velocity component in C IV.

B4 P6

Both P6a and P6b show Mg II absorption comprising the AA3 coincidence. The Mg II in P6a is in a blend but seems reliable. The Mg II in P6b is less secure. Its Mg II 2803 is the blue side of a blend with N V 1238. We use the redshift $z = 2.5593$ for the N V from its Si III 1206.

The EA1 absorption system in P6a is coincident with the z_{em} of P6b. The C IV has multiple velocity components that are blended. The N V is a single velocity component. Both the N V and C IV are slightly blueward of their emission lines.

The same absorption system in P6a that comprises EA1 is coincident with an absorption system in P6b, which is AAA28. The system in P6b shows a single velocity component in C IV.

B5 P7

AA and EAV coincidences. The C IV in P7a is very strong and is a single velocity component. The Al III is a multiple velocity component. The C IV in P7b is a single velocity component. EAV18 is C IV in P7b coincident with the z_{em} of P7a.

B6 P8

EA, EAV and AAV coincidences. For EA2 an absorption system in P8a is coincident with the z_{em} of P8c. The C IV is a single velocity component and slightly blueward of its emission line. The P8a absorption system of EA2 is also coincident with an associated system of P8c giving AAA24 and an associated system of P8b giving AAA25. The AAA24 absorption system in P8c shows a single velocity component in C IV.

The C IV in the system in P8b is strong and its $\lambda 1550.77$ transition is blended with another C IV at a different redshift. For EA5 the z_{em} of P8a is coincident with the AAA25 absorption system in P8b. For EAV20 the z_{em} of P8c is also coincident with the AAA25 absorption system in P8b. For EA6 the z_{em} of P8a is coincident with another absorption system in P8b. The C IV in this system in P8b is strong and its $\lambda 1548.19$ transition is blended with the C IV in the system mentioned above. We find a Ca II in P8a at $z = 0.4215$.

B7 P22

EA, AA, AAA, EAV and AAV coincidences. An absorption system in P22a is coincident with the z_{em} of P22b. The same absorption

system in P22a is coincident with an absorption system in P22c and two different absorption systems in P22b. The C IV in P22a is strong and has multiple velocity components that are blended. The Si IV has multiple velocity components. The N V in the system in P22c is a single velocity component and is in the Ly α emission line. The two coincidences with P22b are AAA28 and AAA29. For P22b the $\lambda 1550.77$ transition of the C IV in AAA28 is blended with the $\lambda 1548.19$ transition of the C IV in AAA29. In addition, the system in P22c mentioned above is also coincident with the two close proximity systems of P22b giving AAA26 and AAA27 and the z_{em} of P22b to form EAV21. For the AAV coincidence, in P22a the C IV and Si IV both show a large single velocity component. In P22b the C IV and Si IV both show a small single velocity component.

B8 P23

An EA coincidence. An absorption system in P23a is coincident with the z_{em} of P23b. The C IV is at the peak of the C IV emission line and is a single velocity component.

B9 P25

Two AA coincidences. For P25a the C IV in both coincident systems is a single velocity component. For P25b the C IV in both coincident systems show multiple velocity components.

B10 P31

Two AA coincidences and an AAV coincidence. For AA8 a Mg II absorption system in P31a is coincident with a Mg II absorption system in P31b. The Mg II in P31b is a single velocity component, and the Mg II in P31a is weak but is also a single velocity component. AA9 consists of an absorption system in P31a that shows strong multiple velocity components in C IV and an absorption system in P31b with C IV that is a single velocity component. AAV19 consists of the C IV absorption of P31a of AA9 and C IV absorption in P31b that is a single velocity component.

B11 P36

EA and AAA coincidences. An absorption system in P36b is coincident with the z_{em} of P36a and also with an associated system of P36a. The system in P36b consists of a single velocity component in Si II, Al II and Al III. AAA30 is this system plus a single velocity component N V absorption in P36a.

B12 P38

Two AA coincidences. An absorption system in P38a with large C IV that has multiple velocity components is coincident with an absorption system in P38b with large C IV that has multiple velocity components. Another absorption system in P38a with weak C IV that has multiple velocity components is coincident with an absorption system in P38b with weak C IV that has multiple velocity components.

B13 P42

Two AA coincidences. An absorption system in P42a with Mg II that has multiple velocity components is coincident to a system in P42b with Mg II that is a single velocity component. An absorption

system in P42a is coincident with an absorption system in P42b. The C_{IV} in both systems has strong multiple velocity components.

B14 P44

An AA coincidence. An absorption system in P44a with C_{IV}, Mg II, Al II and Fe II identified is coincident with an absorption system in P44b that has C_{IV} identified. The C_{IV} in both systems are large and appear in the Ly α forest.

B15 P70

An AA coincidence. An absorption system in P70a with Mg II and Fe II is coincident with an absorption system in P70b with C_{IV}.

B16 P83

An AAA coincidence. An absorption system in P83a with C_{IV} is coincident with an absorption system in P83b with Si III and H I. The C_{IV} is a single velocity component.

B17 P125

An AAV coincidence. Both of the absorption systems contain C_{IV}. The C_{IV} in P125a is a large single velocity component and the C_{IV} in P125b is a small single velocity component.

B18 P147

An AAA and two EAV coincidences. EAV29 is the coincidence of an absorption system in P147a and the z_{em} of P147b. This same absorption system is also coincident with an absorption system in

P147b with a single velocity component in C_{IV} identified. A system in P147b with a single velocity component in C_{IV} identified slightly to the red of the emission line is coincident with the z_{em} of P147a.

B19 P153

The emission redshift of P153a is an EA coincidence with a system in P153b with weak single velocity components in C_{IV} and Si IV.

B20 P155

AA and AAA coincidences. An absorption system in P155a is coincident with an absorption system in P155b. Also, another absorption system in P155a is coincident with a separate absorption system in P155b.

SUPPORTING INFORMATION

Additional Supporting Information may be found in the online version of this article:

Table 4. The 690 metal-line absorption systems in the spectra of the 310 QSOs. Supporting Information may be found in the online version of this article.

Please note: Wiley-Blackwell are not responsible for the content or functionality of any supporting information supplied by the authors. Any queries (other than missing material) should be directed to the corresponding author for the article.

This paper has been typeset from a \TeX / \LaTeX file prepared by the author.